UNIVERSIDADE
BEIRA INTERIOR

On the Development of an Anti-Sloshing System for Sub-Orbital Vehicle Cryogenic Tanks

Adriana Raquel Moura Pinto

Dissertação para obtenção do Grau de Mestre em
Engenharia Aeronáutica
(mestrado integrado ciclo de estudos)

Orientador: Prof. Doutor André Resende Rodrigues da Silva
Co-orientador: Rodrigo Pinto Carvalho
Co-orientador: Bernardo Rocha

outubro de 2023

Declaração de integridade

Eu, Adriana Raquel Moura Pinto, que abaixo assino, estudante com o número de inscrição a41794 de/o Mestrado Integrado em Engenharia Aeronáutica da Faculdade de Engenharia, declaro ter desenvolvido o presente trabalho e elaborado o presente texto em total consonância com o **Código de Integridades da Universidade da Beira Interior**.

Mais concretamente afirmo não ter incorrido em qualquer das variedades de Fraude Académica, e que aqui declaro conhecer, que em particular atendi à exigida referenciação de frases, extratos, imagens e outras formas de trabalho intelectual, e assumindo assim na íntegra as responsabilidades da autoria.

Universidade da Beira Interior, Covilhã 09/10/2023

Dedicatória

Aos meus pais, ao Pedro, ao meu padrinho e ao Martim.

Obrigada pelo apoio incondicional e por iluminarem o meu caminho sempre.

Agradecimentos

Esta dissertação marca o final de um belo percurso de cinco anos onde muito foi aprendido. Apesar disso, este foi o trabalho mais desafiador e que me permitiu desenvolver mais quer a nível pessoal quer a nível profissional. Nada disto teria sido possível se o Rodrigo e o Bernardo não me tivessem possibilitado esta oportunidade. Agradeço pela confiança que depositaram em mim e pela ajuda incansável ao longo destes meses. Obrigada ao projeto VIRIATO pela disponibilização dos fundos necessários para o projeto. Agradecer ainda ao INEGI por me terem acolhido de tão bela forma na instituição e pela oportunidade que me foi dada. Obrigada ainda ao professor André pelo acompanhamento e por ter aceitado este desafio.

Não posso deixar de agradecer á minha família por todo o apoio que me deram ao longo de toda a minha existência. Não descorando ninguém, não posso deixar de mencionar em especial o meu pai e a minha mãe que foram os principais intervenientes na minha jornada. Obrigada por terem acreditado em mim ao longo de todo este tempo e pelo investimento que fizeram em mim. Mesmo estando longe estiveram sempre a torcer por mim e estou muito grata por mim. Quero ainda mencionar o meu afilhado Martim, que sempre se mostrou interessado quando lhe contava sobre o espaço e por me ter alegrado em alguns dias em que o espírito não era tanto.

Ao Pedro, por ter sido um verdadeiro companheiro ao longo destes cinco anos. Obrigada pela ajuda incansável em todo o percurso, pelo apoio em momentos menos bons e por ter tido a paciência necessária em alturas em que o stress falava mais alto.

Obrigada aos amigos, tanto aos que estão comigo desde o começo como àqueles que a Covilhã me deu oportunidade de conhecer, por me terem acompanhado, ajudado quando eu precisava e por terem dado a satisfação de viver coisas incríveis.

Resumo

O sloshing tem vindo a ser tema de estudo desde o ínicio dos anos 60 uma vez que representa um problema real para diversos meios de transporte, como por exemplo tanques cisterna, aviões e foguetes. Este fenómeno corresponde ao movimento indesejado do líquido dentro de um reservatório quando o mesmo é sujeito a uma perturbação levando ao aparecimento de cargas indesejadas que afetam a estabilidade do veículo.

Esta dissertação pretende perceber a influência do sloshing quando aplicado aos tanques criogénicos do veículo sub-orbital no âmbito do projeto VIRIATO. O maior objetivo consiste no desenvolvimento de um sistema anti-sloshing para ser aplicado no caso em questão. Para reduzir os efeitos do sloshing, comummente, são aplicados dispositivos designados de baffles. Existem diversas configurações de baffles sendo a mais comum os anéis.

Primeiramente foi implementada a equação de Miles desenvolvida por Bauer, através de Python, fazendo-se um estudo do amortecimento de diversas configurações de baffles com espaçamento constante. Para perceber a influência de um espaçamento diferente, utilizou-se o método de Powell para otimizar a configuração. Obtiveram-se 4 configurações, posteriormente, implementadas nos modelos numérico e experimental.

O modelo numérico foi implementado em ANSYS Fluent® utilizando-se uma análise transiente e pressure-based com modelo VOF. Para modelar a turbulência foi utilizado o modelo k-ε. O modelo experimental, completamente desenvolvido no INEGI, consiste numa estrutura feita com perfis de alumínio extrudidos e um tanque em acrílico e blocos de alumínio maquinados. O sistema de anti-sloshing foi feito de forma a facilitar a troca de configurações. A excitação foi fornecida por um modelo elétrico acoplado com um mecanismo Scotch-Yoke.

O modelo numérico e o modelo experimental permitiram obter a variação da superfície livre ao longo do tempo. A eficiência da implementação dos baffles foi corroborada observando-se uma rápida estabilização da superfície livre, assim que o movimento foi parado. Para além disso, a previsão analítica de que um maior número de baffles amortece mais o líquido foi corroborada.

Palavras-chave

Sloshing, Cryogenic tanks, Anti-sloshing, Ansys Fluent, Experimental model.

Abstract

Sloshing has been a topic of study since the beginning of the 1960s as it represents a real problem for various means of transport, such as tanks, airplanes, and rockets. This phenomenon corresponds to the unwanted movement of liquid within a reservoir when it suffers a perturbation, leading to unwanted loads that affect the vehicle's stability.

This dissertation aims to understand the influence of sloshing when applied to the cryogenic tanks of the sub-orbital vehicle within the scope of the VIRIATO project. The main objective is to develop an anti-sloshing system to be used in the case in question. To reduce the effects of sloshing, devices called baffles are commonly applied. There are several baffle configurations, the most common being rings.

Firstly, the Miles equation developed by Bauer was implemented, using Python, carrying out a study of the damping of different baffle configurations with constant spacing. To understand the influence of different spacing, Powell's method was used to optimize the configurations. Four configurations were obtained and subsequently implemented in the numerical and experimental models.

The numerical model was implemented in ANSYS Fluent® using a transient and pressure-based analysis with a VOF model. To model turbulence, the k-ε model was used. The experimental model, completely developed at INEGI, consists of a structure of extruded aluminum profiles an acrylic tank, and machined aluminum blocks. The anti-sloshing system was designed to facilitate changing settings. Excitation was provided by an electrical model coupled with a Scotch-Yoke mechanism.

The numerical and experimental models allowed to obtain the variation of the free surface over time. The efficiency of implementing the baffles was corroborated by observing a rapid stabilization of the free surface as soon as the movement stopped. Furthermore, the analytical prediction that a higher number of baffles dampens the liquid more was corroborated.

Keywords

Sloshing, Cryogenic tanks, Anti-sloshing, ANSYS Fluent, Experimental model.

Contents

List of Figures

List of Tables

Nomenclature

Latin Letters

A_f	Forcing Amplitude	[m]
b	Wave amplitude	[m]
C	Constant	[-]
$C_{1\varepsilon}$, $C_{2\varepsilon}$, $C_{3\varepsilon}$	Constants	[-]
d	Distance between baffle and free surface	[m]
D	Distance between baffles	[m]
E	Energy dissipation	[J]
F_e	Excitation Force	[N]
g	Gravitational acceleration	[m/s^2]
G_ω	Generation of ω	[-]
G_b	Generation of turbulent kinetic energy due to buoyancy	[-]
G_k	Generation of turbulent kinetic energy due to mean velocity gradient	[-]
h	Tank height	[m]
H	Liquid height	[m]
J_m	Bessel function of order m	[-]
K	Spring constant	[N/m]
k	Turbulent Kinetic Energy	[m^2/s^2]
l_s	Pendulum length	[m]
m	Mass	[kg]
mn	Sloshing Mode	[-]
n	Number of baffles	[m]
p	Pressure	[Pa]
r	Tank radius	[m]
S_k, S_ε, S_ω	User defined source terms	[-]
T	Period	[s]
t	Time	[s]
u	Velocity in x direction	[m/s]
v	Velocity in y direction	[m/s]
w	Ring baffle width	[m]
w	Velocity in z direction	[m/s]
W	Weight	[N]
$x(t)$	Position of the tank	[m]
y	Position of the first baffle	[m]
Y_k, Y_ω	Dissipation of k and ω due to turbulence	[-]

Y_M	Contribution to the dissipation rate	[-]
A_s	Dimensionaless number of amplitude	[-]
Bo	Bond Number	[-]
Fr	Froude number	[-]
Re	Reynolds Number	[-]
We	Weber number	[-]
W_s	Dimensionaless number of frequency	[-]

Vectors

n	Normal vector	[-]
u	Velocity	[m/s]
x	Optimization result	[m]

Greek Letters

α	Tank cross-sectional area	[m]
β_i	Constant	[-]
δ	Damping factor	[m]
ε	Turbulent kinetic energy dissipation rate	[m^2/s^3]
η	Displacement of the free surface	[m]
γ	Damping Ratio	[-]
Γ_ω	Effective diffusivity of ω	[m^2/s]
Γ_k	Effective diffusivity of k	[m^2/s]
κ	Transport variable	[-]
λ	Scaling coefficient	[-]
μ_t	Turbulent kinetic energy	[m^2/s^2]
∇	Rotational	[-]
ν	Kinematic viscosity	[m^2/s]
ω	Frequency	[rad/s]
ω_{mn}	Sloshing mode natural frequency	[rad/s]
Φ	Velocity potential function	[m^2/s]
ρ	Density	[kg/m^3]
σ	Superficial tension	[N/m]
σ_ε	Turbulent Prandlt number for ε	[m^2/s]
σ_k	Turbulent Prandlt number for k	[m^2/s]
τ^R	Reynolds stress tensor	[N/m^2]
ξ_{mn}	Root of the Bessel function of order m	[-]
ζ	Amplitude of liquid oscilations	[m]

List Of Acronyms

AFP	Automated Fibre Placement
CFD	Computational Fluid Dynamics
CG	Center of Gravity
CPV	Composite Pressure Vessel
DNS	Direct Numerical Simulation
FVM	Finite Volume Method
FW	Filament winding
LES	Large-eddy Simulation
LH	Liquid Height
LHx	Liquid Hydrogen
LOx	Liquid Oxygen
MUSCL	Monotone Upstream-Centeres Schemes for Conservation Laws
PISO	Pressure-Implicit with Splitting of Operators
PRESTO!	Pressure Staggered Option
QUICK	Quadratic Upstream Interpolation for Convective Kinematics
RANS	Reynolds-Averaged Navier-Stokes
RNG	Renormalization Group
UDF	User Defined Function
VIRIATO	Veículo Inovador Reutilizável para investigação e Alavancagem de Tecnologia Orbital
VLES	Very Large Eddy Simulation
VOF	Volume Of Fluid
WALE	Wall-Adapting Local Eddy-Viscosity Model

Chapter 1

Introduction

1.1 Motivation

Sloshing is a phenomenon that emerges when a fluid is perturbated, causing the movement of the fluid free surface. The disturbance creates forces and moments. This phenomenon has been studied since 1960 because of its importance for spacecraft with liquid propulsion. The perturbation in the movement of a reservoir causes the fluid to move with a given frequency. If this frequency is close to the frequency of any control system, an instability in the flight can be created [2]. The propelled flight phase corresponds to the phase where sloshing is more significant due to lateral motions. The forces that result from this phenomenon interfere with the attitude control system, a thermal stratification appears, and depending on the amplitude of the sloshing wave, droplets can emerge [3].

There have been situations when sloshing guided to failure. In 2007, the Falcon 1 mission failed because the sloshing frequency of the liquid oxygen (LOx) coupled with the thrust vectoring control system, amplified the oscillation of the spacecraft [4]. During the final moments of the Apollo-11 Lunar Module landing, the remaining propellant caused a sloshing effect, creating oscillatory motion that posed a challenge to control the module accurately. As the propellant level decreased to about fifty percent, fluid started to slosh even more, but it still possessed enough mass to generate substantial forces and moments. This situation demanded more stringent control measures to ensure a successful landing maneuver [5, 6].

Sub-orbital vehicles are capable of traveling to outer space. However, unlike orbital vehicles, they do not have sufficient energy to achieve an orbit. Orbital vehicles travel about 28000 km/h, while sub-orbital vehicles travel at approximately 6000 km/h. Once these spacecraft reach their highest altitude, their items can experience a small period of microgravity before descent. Sub-orbital vehicles are often used to test and demonstrate technology for aerospace applications, such as hardware qualification before orbital flight. Furthermore, these vehicles can be used to monitor populations, animals, vegetation, and weather events by remote sensing. The Swedish Space Corporation launched the Neurobeta experiment to resolve some questions about diabetes type 1 using living stem cells and insulin-producing beta cells under microgravity. Space tourism also uses sub-orbital vehicles, recently seen with Virgin Galactic and Blue Origin flights. The vehicles allow passengers to experience spaceflight and be under a microgravity field for a short period [7].

The VIRIATO project arises from the Portuguese government's desire to enter the microsatellite launching market to take part of the future development of the space sector. Starting in 2020, the project consists of developing, integrating, and operating a suborbital vehicle capable of validating and testing fundamental technologies for microsatellite launcher development. To do so, the project involves a consortium with companies of the country working in the aerospace field. INEGI enters the project with the responsibility of developing the tank [8].

The mixture of Liquid Hydrogen (LHx) as propellant with LOx as oxidizer has become the most popular propulsion fuel for space vehicles, mainly because it generates the highest specific impulse compared to other mixtures [9]. Nevertheless, the use of cryogenic fluids has some problems. Ignition of LHx in the presence of oxygen causes powerful explosions. Hence, safety measures must be implemented to reduce the violent handling of propellants and oxidizers. Additionally, cryogenic fluids have a low saturation temperature. This combined with heat fluxes from outside the reservoir, leads to evaporation and hinders storage for long periods [9].

There are different ways to store fuel, i.e., different types of tanks with several materials. A common way to store cryogenic fuels is using carbon fiber composite pressure vessels. Those tanks allow a lightweight construction with a gravimetric storage density much higher than steel tanks. The architectureof teh tanks can be divide into five types. The one used in VIRIATO Project is of type V, which corresponds to a tank that does not have a liner and uses composite as a gas barrier and a load-bearing structure. Type V tanks, called CPVs (Composite Pressure Vessels), can have a higher fatigue performance while reducing weight. There are different ways to manufacture this vessel. Tensioned bands of fibers are commonly winded around a rotating mandrel called filament winding (FW). However, to create this tank, INEGI opted for an alternative method. Using Automated Fibre Placement (AFP), the fibers were placed on a rotating mandrel using a more automated method, such as a robotic arm. This technique allowed to have a higher quality in the fiber placement, as well as more quality and less waste [10].

1.2 Thesis Structure

Sloshing can be a significant problem for spacecraft since it can lead to instability. However, a way to control the movement of the liquid is by using anti-sloshing devices such as baffles. Baffles increase the effective damping on the fluid, inhibiting ts oscillations [11]. To understanf the behavior of sloshing, this work aims to understand the influence of sloshing and to find an optimal configuration of the anti-sloshing devices reducing the effects of liquid movement.

With that purpose, three different approaches will be made during this work: analytical, numerical, and experimental. To do so, this document is divided into eight chapters.

Chapter 1 is dedicated to explain the basis of the work as well as the main motivation. It also explains how the work is divided and what are the main objectives of this work.

Chapter 2, does a review of sloshing theory. it divides the types of sloshing dynamics and mention important contents for sloshing. This chapter also includes the basis of damping theory and how it can be used to evaluate the fluids dynamics. One of the most important contents of this chapter is related to the analytical approach uses Bauer's equations, which corresponds to a set of equations that allows obtaining the damping ratio provided by different configurations of ring baffles.

Since study a tank with the real dimensions of VIRIATO would be difficult, a scaled tank must be used. Because of that, a scaling analysis must be implemented. This is done in Chapter 3. This Chapter discusses the governing equations and the Boundary conditions and make a first approach on dimensionless numbers. lastly, the three types of similarity are accounted.

Chapter 4 dedicates to anti-sloshing devices in which a literature review is done. Furthermore, it shows the implementation of Bauer's equation in Python, testing different configurations of baffles with varying distances, positions, numbers, and widths. Since, this first code only allows configurations with equal spacing, an optimization study is also implemented using Powell's method. The configuration was optimized, determining the optimal spatial configuration while considering the general consideration of non-uniform spacing. This analytical analysis allows for the definition of an initial table of study cases implemented in ANSYS.

Numerical analyses are reviewed in Chapter 5. Moreover, the theory behind numerical methods are explained in order to conclude which are the best methods to be use in this study. The numerical analysis are done using ANSYS Fluent®, which is CFD software. This model introduces the resulting configurations from the analytical model with the same conditions. The post-processing allows to obtain the damping ratio through the logarithmic decrement. The numerical model uses VOF to simulate the free surface. Also, it is known that domain partition is crucial, which implies the study of mesh convergence.

Chapter 6 discusses the previously experimental setups implemented and also the experimental setup and methods developed for this study. The experimental approach allows the validation of the numerical model. The setup is designed and explained, and the procedure is detailed. The rig is developed with the mindset that it can be used for other projects.

The results obtained in the numerical and experimental models are discussed and compared in Chapter 7. The results are evaluated and also compared for each configuration allowing a more clear comparison.

Lastly, Chapter 8 discusses the work developed and conclusions about the best configuration is made. Moreover, some suggestions of future work are mentioned.

1.3 Objectives

The main objective of this work is to answer one essential question:

1. What is the anti-sloshing configurations that optimizes damping in a cylindrical tank?
2. How is developed and implemented a numerical model for a sloshing problem?
3. How to develop an experimental setup for a sloshing analysis?
4. Can the experimental model validate the numerical model?
5. What is the best anti-sloshing system to be implemented in VIRIATO project?

Chapter 2

Sloshing Theory

Sloshing describes the movement of a liquid inside a reservoir when the container suffers a disturbance. The behavior of the fluid depends on different factors and can be characterize by different regimes. This movement generates momentum and forces that can lead to the instability of a vehicle. Besides that, the undesired movement of the liquid can lead to structural problems. Hence, this is a problem that is considered in various applications such as rockets, trucks, and airplanes typically consider.

Depending on the type of disturbance and the geometry, the movement of the free surface can be described as asymmetric, symmetric, rotational, planar, nonplanar, irregular beating, quasi-periodic or chaotic. In cases where the interaction of the liquid with an elastic container is essential, the fluid can show a type of motion characterized by an exchange of energy between interacting modes. The effect of gravity is also substantial such that under low gravity, the surface tension can not be neglected, and the movement of the liquid is randomly oriented depending upon the wetting characteristics of the tank wall.

This section describes the dynamics of sloshing and discusses the modeling of this phenomenon. Furthermore, the concept of damping, which is an important parameter to the development of anti-sloshing devices, is reviewed. Thus, the following section describes theoretical damping.

2.1 Linear Sloshing Dynamics

This section describes the linear sloshing dynamics using the velocity potential theory and modal analysis. besides that, it also describes the mechanical models used to evaluate damping.

Linear sloshing dynamics define the most simple behavior of the free surface, considering that the wave and liquid motion amplitude is linearly proportional to the motion amplitude of the tank. This theory considers some assumptions [12, 13, 4, 14, 15, 16]

1. fluid is inviscid, i.e., $\nu = 0$;
2. flow is irrotational, i.e., $\nabla \times \mathbf{u} = 0$;
3. fluid is incompressible, i.e., $\rho =$ constant;
4. flow is gravity-dominated, i.e., Bo $\gg 1$;

5. velocities and displacements are small;

6. fluid is homogeneous;

7. the vessel is rigid;

8. oscillation of the container is given by $X(t) = A_0 \sin(\omega t)$.

As mentioned, the flow field is assumed to be irrotational and inviscid, which enables the use of the velocity potential function $\Phi(R, \theta, z)$ to describe the liquid's velocity field. Since this work refers to a cylindrical container, this function uses cylindrical coordinates. Thus, the following Equation depicts the velocity of the liquid:

$$\mathbf{V} = \nabla\Phi. \quad (2.1)$$

Considering assumptions 3., 1. and 7., the free-boundary potential flow equations govern the wave motion of the fluid. In the case of a circular cylinder with radius r and filled with a height of H, the velocity potential of the fluid motion at the free surface concerning the container follows the Laplace equation. Thus, the Equation that represents the field writes as

$$\Phi(R, \theta, z, t) = \sum_{m=0}^{\infty} \sum_{n=1}^{\infty} \alpha_{mn}(t) \cos(m\theta) J_m \left(\frac{\xi_{mn} R}{r} \right) \frac{\cosh\left[\xi_{mn} \frac{(z+H)}{r}\right]}{\cosh\left(\xi_{mn} \frac{H}{r}\right)} \quad (2.2)$$

where α_{mn} and is a time-dependent function that come from the initial conditions of the free surface, J_m is a Bessel function of the first kind with order m, ξ_{mn} is the n^{th} zero of the first derivative of the Bessel function J_m. In this equation, the subscripts m e n refers to the mode and wave numbers, respectively [12, 13, 4, 14, 15]. Table 2.1 exhibits the derivative roots ξ_{mn} of the Bessel function of the first kind with order m.

Table 2.1: Zeros ξ_{mn} of the first derivative of the Bessel function J_{mn} of the first kind with order m.

		m				
		0	1	2	3	4
n	0	0	0	0	0	0
	1	3.832	1.841	3.054	4.201	5.318
	2	7.016	5.331	6.706	8.015	9.282
	3	10.174	8.536	9.970	11.346	12.682

2.1.1 Normal modes Frequencies

Normal modal frequencies can be acquired from the linearized free-surface boundary condition under the assumption on Equation 2.3 where $\tilde{\phi}$ is the Laplace equation and η is the displacement of the free-surface.

$$\frac{\partial \tilde{\Phi}}{\partial t} - g\eta = 0 \quad (2.3)$$

where eta is fluid surface elevation. Once derivated to time, the above equation turns into

$$\frac{\partial^2 \tilde{\Phi}}{\partial t^2} + g\frac{\partial \tilde{\Phi}}{\partial z} = 0 \quad (2.4)$$

The time-dependent functions in Equation 2.2, α_{mn} can be expressed as harmonics. Thus, substituting Equation 2.2 in Equation 2.4, the natural frequencies ω_{mn} of the liquid free-surface are given by:

$$\omega_{mn}^2 = \frac{g\xi_{mn}}{r} \tanh\left(\xi_{mn}\frac{H}{r}\right) \quad (2.5)$$

This equation is only valid for cases where surface tension is neglected. For the first mode, $m = 1$ and $n = 1$, ξ_{mn} is equal to 1.841, as mentioned in Table 2.1.

The previous equation shows that the natural frequency depends on the geometrical characteristics of the tank, the level of fluid, and also on the vertical acceleration. Furthermore, this Equation simplifies by neglecting the influence of the bottom of the tank by considering only high levels of fluid, which leads to

$$\omega_{mn} = \sqrt{\frac{g\xi_{mn}}{r}}. \quad (2.6)$$

Since the geometric characteristics influence the natural frequency, ring baffles implementation in a tank can modify its natural frequency. If the baffle intersects the free surface, the resonant frequency increases, and if the baffle location is at more than one baffle width depth, it decreases [14, 17].

2.1.2 Normal Modes

Using Equation 2.2 in Equation 2.3, the fluid surface elevation is translated into Equation 2.7.In this case, $\bar{\alpha_{mn}}$ and $\bar{\beta_{mn}}$ represent constant coefficients that are obtained from initial conditions [15, 18, 19].

The contact line can be written as

$$\eta = \frac{1}{g}\sum_{m=0}^{\infty}\sum_{n=1}^{\infty}\left[\bar{\alpha}_{mn}\cos(m\theta) + \bar{\beta}_{mn}\sin(m\theta)\right] J_m\left(\xi_{mn}\frac{R}{r}\right)\cosh\left(\xi_{mn}\frac{H}{r}\right)\left(\omega_{mn}\cos(\omega_{mn})t\right) \quad (2.7)$$

If the surface tension is strong enough to keep the contact line fixed in place, i.e., $\eta(r,\theta,t) = 0$, Equation 2.7 becomes

$$\eta(R,\theta,t) = e^{i\omega t}\bar{\eta}(R,\theta) = \sum_{m=0}^{\infty}\sum_{n=1}^{\infty}\frac{\alpha_{mn}}{i\omega}\frac{\xi_{mn}}{r}\cos(m\theta)\sinh\left(\xi_{mn}\frac{H}{r}\right)J_m\left(\xi_{mn}\frac{R}{r}\right)e^{i\omega t}. \quad (2.8)$$

Considering that,

$$B_{mn} = \frac{\alpha_{mn}}{i\omega}\frac{\xi_{mn}}{r}\sinh\left(\xi_{mn}\frac{H}{r}\right) \quad (2.9)$$

Equation 2.8 takes the form of

$$\eta(R,\theta,t) = \sum_{m=0}^{\infty}\sum_{n=1}^{\infty}B_{mn}\cos(m\theta)J_m\left(\xi_{mn}\frac{R}{r}\right)e^{i\omega t}. \quad (2.10)$$

Taking the complex law $\tilde{R}e^{i\bar{\omega}t} = \tilde{R}(\cos(\tilde{\omega}t) + i\sin(\tilde{\omega}t))$, Equation 2.10 becomes

$$\eta(R,\theta,t) = B_{mn}J_m\left(\varepsilon_{mn}\bar{r}\right)\cos(m\theta)\left[\sin\left(\omega_{mn}t\right) - i\cos\left(\omega_{mn}t\right)\right] \quad (2.11)$$

which can be used to visualize the free surface by using only the real part of the previous Equation, i.e.,

$$\mathrm{Re}\left(\zeta_{mn}\right) = B_{mn}J_m\left(\varepsilon_{mn}\frac{R}{r}\right)\cos(m\theta)\sin\left(\omega_{mn}t\right). \quad (2.12)$$

Figure 2.1 describes the behavior of the free surface for modes of $0 \leq m \geq 2$ and $n \geq 2$. It is possible to see that normal modes are symmetrical and asymmetrical. Symmetrical modes consist of a symmetrical axial peak whose shape defines by the Bessel function of the first kind of order 0. Figures 2.1a and 2.1b shows two symmetrical modes. As the wave number n increases, the number of waves in the radial direction also increases. The highest symmetrical modes are difficult to observe since their excitation frequency needs to be higher enough to compensate for the inertia of the fluid. Thus, some symmetrical modes appear only in the regime of chaotic sloshing or liquid splashing where it is possible to witness the dispersion of some droplets from the free surface [13].

Asymmetric modes occur when a reservoir is subjected to axial or lateral excitation, and its comportment depends, exclusively, on the excitation frequency. In Figures 2.1c, 2.1d, 2.1f are represented some asymmetric modes. The most common asymmetric mode is the first one $m = 1$ and $n = 1$ (Figure 2.1c) since it occurs for relatively small excitation frequencies in the order of the first natural frequency [13]. This mode is characterized by an asymmetric form where a side of the wave elevates and the other goes down. The first mode is of fundamental interest since it creates a net force or torque in the tank [14, 20].

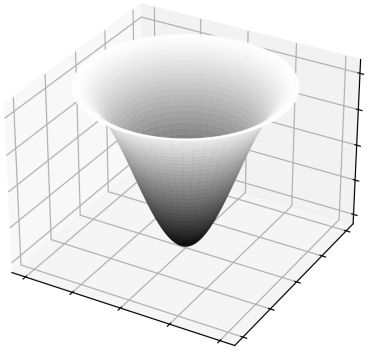

(a) $m = 0, n = 1$

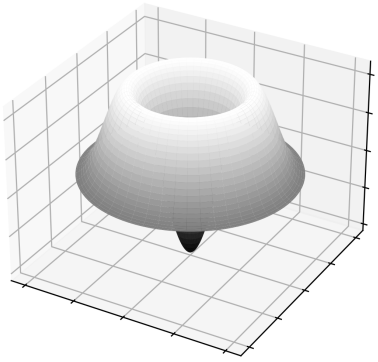

(b) $m = 0, n = 2$

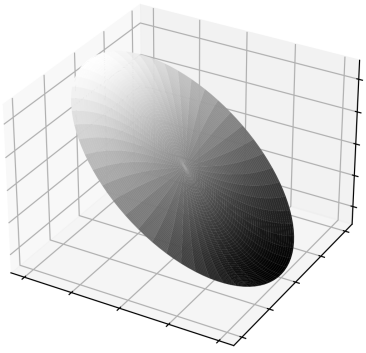

(c) $m = 1, n = 1$

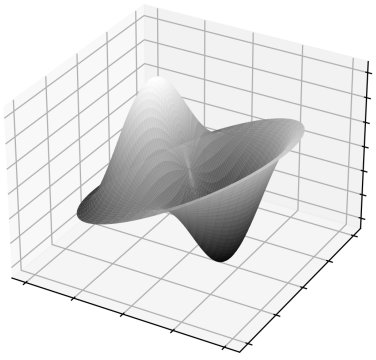

(d) $m = 1, n = 2$

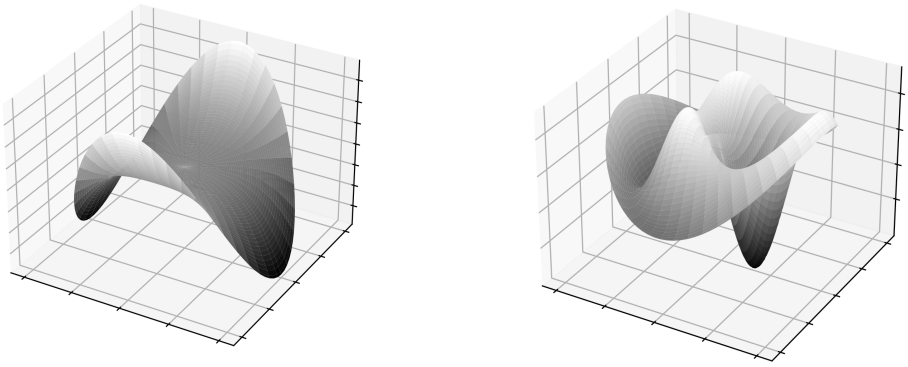

(e) $m = 2, n = 1$ (f) $m = 2, n = 2$

Figure 2.1: Displacement of the free surface for the sloshing mode m, n.

2.2 Mechanical Slosh Models

When a reservoir is under lateral motion, the formed wave stands up on one side of the tank while it descends on the other. These models describe sloshing by establishing an analogy between the motion of the liquid's center of mass and an oscillation mechanical systems such as a pendulum or a spring-mass system [14]. Both these methods are similar and accurately represent the sloshing modes. However, they only allow the representation of the first sloshing mode with linear dynamics.

The equivalent models consider a total mass of fluid m composed by a fixed mass, m_0, and the mass of the slosh m_s corresponding to the mass of the fluid that takes part in the sloshing. Thus, taking the principle of conservation of mass, the total mass of the system is equal to the sum of the fixed mass with the mash of slosh, i.e.,

$$m = m_0 + \sum_{n=1}^{\infty} m_s \quad (2.13)$$

In this Equation, the sloshing mode m is represented by introducing an n number of slosh masses, i.e., to represent the first sloshing mode where $m = 1$, then $n = 1$.

2.2.1 Spring-mass Model

The spring-mass model is represented in Figure 2.2b, where the viscosity effects are represented by the dashpots and the spring elements represent the sloshing liquid. Each spring-mass portrays a sloshing mode. Considering a model with n spring masses, the system's center of mass must be at the same height as the liquid's center of mass. Thus, the spring constants K_s can be determined in function of the frequency as

$$K_s = \omega_n^2 m_s \quad (2.14)$$

where m_s corresponds to the spring's mass, to obtain the Equation of motion of the n^{th} spring, an ordinary differential equation of second order, such as Equation 2.15, can be used.

$$m_s \ddot{y}(t) = -K_s y(t) - d_s \dot{y}(t) + F_e(t) \quad (2.15)$$

where d_s is the damping coefficient described as $d_s = 2m_s\gamma\omega_{mn}$ and F_e is the excitation force equal to $F_e(t) = m_s y_A \omega_{mn}^2 \cos(\omega t)$. Thus, substituting these descriptions in Equation 2.15, it takes

$$\ddot{y}(t) + 2\gamma\omega_{mn}\dot{y}(t) + \omega_{mn}^2 y(t) = y_A \omega_{mn}^2 \cos(\omega t). \quad (2.16)$$

Damping is an essential parameter in the Equation of motion, since it is related to the kinetic energy that a fluid dissipates when it is oscillated. As explained previously, the damping ratio is obtained from the logarithmic decrement of a given variable. The critical damping case occurs when the damping ratio γ equals one. This condition indicates a critically damped system, which is a condition where the liquid returns to its equilibrium position as quickly as possible without oscillating. Nevertheless, the solution of Equation 2.16 is givens by the superposition of the homogeneous and the particular solution, i.e.

$$y(t) = y_h(t) + y_p(t). \quad (2.17)$$

2.2.2 Pendulum Model

The pendulum model considers n pendulums to represent each sloshing mode. Each pendulum has its support point below the undisturbed free surface, and the series of pendulums must preserve the system's total mass. Considering a pendulum in which the pendulum length l_n is chosen so that the natural frequency of the pendulum is equal to

$$\omega_{11} = \sqrt{\frac{g}{l_n}}. \quad (2.18)$$

The amplitude ε of the excitation is scaled to the pendulum length l_n and can be simplified as

$$\varepsilon = \frac{A_f}{r} \quad (2.19)$$

The pendulum is excited laterally, which means that the motion is on the y axis. This leads to the following equations of motion of the pendulum:

$$\begin{aligned} \left(\frac{d^2}{dt^2} + \frac{g}{L}\right)\alpha - \frac{g}{6L}\alpha^3 + \frac{1}{2}\left(\frac{d^2}{dt^2} + \frac{g}{L}\right)\alpha\beta^2 = \varepsilon\omega^2 \cos\omega t \\ \left(\frac{d^2}{dt^2} + \frac{g}{L}\right)\beta - \frac{g}{6L}\beta^3 + \frac{1}{2}\left(\frac{d^2}{dt^2} + \frac{g}{L}\right)\beta\alpha^2 = 0 \end{aligned} \quad (2.20)$$

where α is the angle between the pendulum and the y axis, β is the angle between the pendulum and x axis and ϑ is the angle between the z axis and the pendulum. The above equations are obtained considering that $\sin(\alpha) \approx \alpha - \frac{a^3}{6}$ and $\cos(\alpha) \approx 1 - \frac{a^2}{2}$. These equations can be used to define the mode of sloshing.

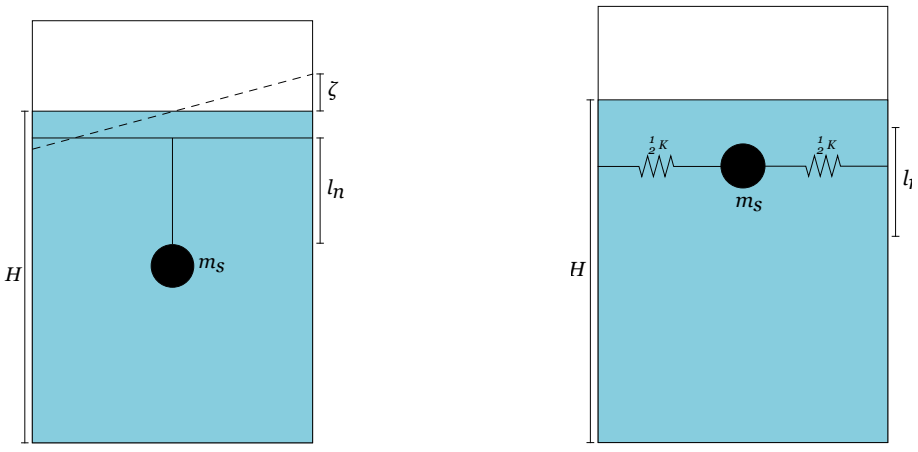

(a) Pendulum model.

(b) Spring-mass model.

Figure 2.2: Equivalent mechanical slosh models.

2.3 Damping

2.3.1 Theory

In liquid sloshing, damping indicates the dissipation of energy that occurs due to various viscous mechanisms. It includes the development of boundary layers at the walls and of

free surface along viscous stresses within the liquid. In small tanks, the dominant form of dissipation is typically from boundary layer effects. In contrast, the contribution from viscous stresses within the liquid interior may become more significant in larger tanks. Viscous effects are often highly reduced, so the energy dissipation of the liquid movement must occur by another means, i.e., by baffles. The current section presents two distinct types of damping: the damping caused by the viscous effects of the fluid and the damping provoked by the implementation of anti-sloshing systems.

In a case with no anti-sloshing devices, damping evaluation is by the logarithmic decrement of the amplitude of sloshing waves caused by the free oscillations of a liquid in a stationary tank. Thus, the logarithmic decrement can be described as [14]

$$\Delta = \ln\left(\frac{\text{peak amplitude of oscillation}}{\text{peak amplitude of oscillation one cycle later}}\right) \quad (2.21)$$

However, damping is commonly quantified by a damping ratio, γ, and computed as a fractional part of the mechanical energy dissipated in each cycle of the oscillation, i.e.

$$\gamma = \frac{\left|\frac{dE}{dt}\right|}{2\omega E} \quad (2.22)$$

where $\left|\frac{dE}{dt}\right|$ is the derivative of the energy dissipation ratio in time.

Even though the viscous effects of the liquid cause some damping, it will not be enough to reduce the movement of fluid [11, 14]. Thus, there are different systems to enhance damping, such as ring baffles. Ring baffles are the most common designs to reduce the unwanted movement of a liquid, since it provides some rigidity to the structure and is very efficient for lateral oscillations.

The damping ratio provided by this system can also be determined by Equation 2.22. However, in the case of a tank with ring baffles, the energy is mainly dissipated by pressure drag. The energy derivative is spatially averaged around the tank circumference and, thus, Equation 2.22 becomes

$$\gamma = \frac{15(4/3\pi)^2 C_1 A f_d^{2.5}\sqrt{\zeta w}}{2\sqrt{\pi}\left(m_s/\rho\right)\Gamma^2}, \quad (2.23)$$

for a cylindrical tank with a ring baffle, and considering that $\frac{h}{r} > 2$ [14]. In this Equation, C_1 is a variable dependent of w in such a way that it is equal to $w/r\left(2 - w/r\right)$, w is the width of the ring baffle, Γ is equal to 0.649, f_d is an exponential function equal to $e^{-1.84h_s/r}$ and

ζ is the wave amplitude on the tank wall.

Miles predicted damping factor γ provided by a ring baffle , who considered a circular cylindrical tank of radius r filled with liquid at a height h. Ring baffle was considered attached to the inner wall of the tank at a distance d from the free surface and with an area equal to $\alpha\pi r^2$. Therefore, Miles derived the following expression 2.24

$$\gamma = \mathrm{C}e^{-\frac{4.6d}{a}}\alpha^{3/2} \quad \left(\zeta/a\right)^{1/2}, \quad \alpha \ll 1 \text{ and } \zeta_1 \ll a, \quad (2.24)$$

where the constant C is obtained through experimental drag measurements of flat plates in an oscillating fluid and is approximately equal to 2.83, ζ, is the amplitude of the liquid measured on the tank wall, and α is the area ratio blocked by baffles on the cross-sectional area. Various institutes [21, 22] validated the Equation and discovered it could extend beyond its limits [22].

One of the limits was related to baffle width, which proved that the Equation could provide damping values for a baffle area of about 1/4 the tank cross-sectional area. However, results indicated that, for some wave displacements, the damping predicted was higher than the one obtained experimentally. Therefore, Bauer [22] developed an extension to the Miles equation acknowledging that during the sloshing cycle, some parts of ring baffles were entirely out of the liquid, fully submerged, or partially submerged.

To account for the effects of the partial submersion of ring baffles, $\bar{\alpha}$ is used instead of α into Equation 2.24. $\bar{\alpha}$ is the effective baffle area ratio that will reduce the values of the damping ratio and therefore, allow to obtain values more close than the ones measured through experimental analysis [22].Therefore, the full Equation that describes $\bar{\alpha}$ is denoted into the subsequent expression

$$\begin{aligned}\bar{\alpha} = {} & \underline{\frac{w}{r}\left(2-\frac{w}{r}\right)} - \frac{1}{2}\left(1-\frac{d/r}{\zeta_w/r}\right) + \frac{2}{\pi}\frac{d/r}{\zeta_w/r}\ln\left[\frac{\zeta_w/r+\sqrt{\left(\zeta_w/r\right)^2-(d/r)^2}}{d/r}\right] - \\ & - \frac{1}{\pi}\frac{d/r}{\left(\zeta_w/r\right)^2}\sqrt{\left(\zeta_w/r\right)^2-(d/r)^2} + \frac{1}{\pi}\arcsin\left(\frac{d/r}{\zeta_w/r}\right) - \frac{1}{2}\frac{d/r}{\zeta_w/r} + \\ & + \frac{1}{2}\left(1-\frac{w}{r}\right)^2\left\{1-\frac{d/r}{\left(1-\frac{w}{r}\right)\zeta_w/r}\right\} - \frac{2}{\pi}\frac{d/r\left(1-\frac{w}{r}\right)}{\zeta_w/r}\,\mathrm{lr}\left[\frac{\zeta_w/r+\sqrt{\left(\frac{\zeta_w}{r}\right)^2-\left(\frac{d/r}{1-\frac{w}{r}}\right)^2}}{\frac{d/r}{1-\frac{w}{r}}}\right] \\ & + \frac{1}{\pi}\frac{\frac{d}{r}\left(1-\frac{w}{r}\right)}{\left(\zeta_w/r\right)^2}\sqrt{\left(\frac{\zeta_w}{r}\right)^2-\frac{(d/r)^2}{\left(1-\frac{w}{r}\right)^2}} - \frac{1}{\pi}\left(1-\frac{w}{r}\right)^2\arcsin\left(\frac{d/r}{\left(1-\frac{w}{r}\right)\zeta_w/r}\right) \\ & + \frac{1}{2}\left(1-\frac{w}{r}\right)\frac{d/r}{\zeta_w/r}.\end{aligned} \quad (2.25)$$

In the case of a fully submerged baffle, in other words, $\frac{d}{r} \geq \frac{\zeta_w}{r}$, then α is equal to the underline term in the previous Equation. If $\frac{\zeta_w}{r}\left(1-\frac{w}{r}\right) \leq \frac{d}{r} \leq \frac{\zeta_w}{r}$, it means that the device is out of the liquid during the slosh cycle, ensuring that the rim of the annular baffle is not out of the fluid at any time, and the dot underlined terms add to the previous one. If a part of the ring gets out of the liquid during a particular time during the slosh cycle, i.e., $\frac{d}{r} < \frac{\zeta_w}{r}\left(1-\frac{w}{r}\right)$, α is defined by the full Equation 2.25.

Considering the ring's location above the undisturbed liquid surface, Equation 2.25 can be applied. However, now it is considered $d^* = (D-d)$ as the distance above the undisturbed liquid surface. The effective baffle are ratio becomes equal to $\bar{\alpha}^* = \alpha - \bar{\alpha}$. Therefore, if $\frac{\zeta_w}{r} \leq \frac{d^*}{r}$ then $\bar{\alpha}^* = 0$, if $\frac{d^*}{r} < \frac{\zeta_w}{r} \leq \frac{d^*/r}{1-w/r}$ then the dot underlined terms in Equation 2.25 are applied, and if $\frac{\zeta_w}{r} \geq \frac{d^*/r}{1-w/r}$ the rest of the formula is applied.

If several ring baffles are implemented, the damping ratio is given by the linear superposition, which is given by the following formula

$$\gamma = \sum_{n=1}^{N} \mathrm{Ce}^{-\frac{4.6d}{r}} \bar{\alpha}^{3/2} \quad \left(\frac{\zeta_1}{r}\right)^{1/2} + \sum_{m=1}^{M} \mathrm{Ce}^{-\frac{4.6d}{r}} \bar{\alpha}^{3/2} \quad \left(\frac{\zeta_1}{r}\right)^{1/2} \quad (2.26)$$

N corresponds to the number of baffles under the liquid, and M is the number above the surface.

2.3.2 Experimental damping

There are two different ways to obtain the damping of sloshing.

One of the methods is wave amplitude decay, which is done by oscillating the tank at the resonant frequency until a steady state is reached and then quickly stopping it. The free surface displacement is measured, and the logarithmic decay of successive waves is calculated with Equation 2.27. However, this method can only be used for the first sloshing mode, since the others decay faster.

$$\gamma = \frac{\delta}{\sqrt{4\pi^2 + \delta^2}} \quad (2.27)$$

Another way consists of analyzing the slosh force amplitude response, which measures the amplitude of the force applied to the tank. One way to do it is by using a load cell, measuring the amplitude as a function of the excitation frequency over a different range of frequencies close to the resonant frequency. As an alternative, the amplitude of the wave can be measured directly. Thus, the force is plotted as a function of the frequency, and then the damping is obtained by

$$\gamma = \frac{1}{2}\frac{\Delta\omega}{\omega_{mn}}, \quad (2.28)$$

where $\Delta\omega$ corresponds to the frequency variation for which the amplitude is 0.707 times the maximum wave amplitude.

Also, the experimental damping can be obtained by the anchor force decay method that consists of attaching the load cell to the tank, and the force is measured after the tank excitation is quickly stopped.

2.4 Nonlinear Sloshing Dynamics

According to weakly nonlinear theory, the behavior of the waves generated by a sinusoidal excitation depends on the amplitude and frequency of that excitation. Thus, three types of waves are associated with the following characteristics [4, 12, 16, 23]:

1. **Stable planar waves:** These are associated with the waves modeled by the pendulum model. Thus, they are related to the linear dynamics. This motion categorizes as steady-state harmonic having a peak wave height that does not vary with time. It also has a single stationary nodal diameter normal to the direction of tank excitation. The following Equation estimates de maximum wave amplitude of stable planar waves:

$$\frac{b}{A_f} \approx \left[\frac{\left(\frac{\omega}{\omega_{11}}\right)^2}{1-\left(\frac{\omega}{\omega_{11}}\right)^2}\right]. \quad (2.29)$$

   where b is the wave's amplitude, and A_f is the force excitation's amplitude.

2. **Chaotic sloshing:** This regime occurs at a frequency close to the natural one. A chaotic regime indicates the increasing amplitude until a particle's downward acceleration on the free surface equals the gravitational acceleration. After that, the amplitude decreases, initiating a new cycle until reaching the critical value of the amplitude again. Thus, the amplitude of the wave is defined by the expression:

$$\frac{b}{r} \approx \pi\frac{A_f}{r}\frac{t}{T_\omega} \quad (2.30)$$

   where T_ω is the oscillation period and t the time instant [12].

3. **Swirl waves:** Also known as rotary sloshing, this regime outlines the very stable waves with a mean amplitude of $0.7r$. Swirl waves break near the top but, once stabilized, transfer angular momentum to the liquid.

The simplification of sloshing problem through the use of mechanical models helps to predict which mode the liquid follows. Considering the motion Equations 2.20 of pendulum model, it is possible to understand that for $\beta = 0$ the liquid has a planar but nonlinear motion. Also, they shows that there are other solutions for motions around z axis which shows a rotary motion. The solutions Equations 2.20 are stable conditions of the model, but they are only true for a given range of parameter's values. The stability characteristics of the solutions can be ascertained through the introduction of a minor disturbance, enabling the identification of conditions under which these perturbations either amplify or diminish over time [14]. These findings can be expressed in relation to a dimensionless frequency denoted as

$$\mu = \varepsilon^{-43} \left[\frac{(\omega^2 - \omega_1^2)}{\omega_1^2} \right]. \quad (2.31)$$

The value of μ can describe the behavior of the liquid. Thus,

- When mu falls either below -0.945 or exceeds 0.757 simple harmonic planar motion remains stable. In these cases, the solutions resemble the typical antisymmetric slosh wave, featuring a stationary nodal line.
- Simple harmonic nonplanar motion is stable in a specific frequency band just above the natural frequency, where 0.154 < μ < 0.757. This type of motion resembles rotary sloshing, where the nodal line of the antisymmetric slosh wave undergoes rotation around the tank's vertical axis.
- Another stable configuration involves simple harmonic motions in which the plane of pendulum-like movement oscillates. This stability is observed within a narrow frequency range centered around the natural frequency, encompassing values of μ between -0.945 and 0.154. In this scenario, the solution corresponds to a swaying back-and-forth oscillation of the nodal line of the antisymmetric slosh wave along the vertical axis of the tank.
- For μ > 0.757, both planar and nonplanar (rotational) motions exhibit stability. The specific type of solution, or the form of sloshing observed, hinges upon whether there is any initial nonplanar motion, such as an initial rotation of the liquid.

Chapter 3

Scaling analysis

Scaling analysis is a powerful technique to properly scale the quantities between models in a study. In a wide range of applications, such as the tank being analysed, testing a full-scale model can be very expensive, both computationally and monetarily. This motivates the definition of a small-scale model. Since the fluids and dimensions of the both models are different, the relation between both models is ensured through the analysis of the de adimensional numbers. This type of analysis allows to reduce the number of variables. Two different approaches can be employed. The first refers to the dimensional analysis using the Buckingham Pi-Theorem. The other is through the scaling of equations. For this problem, the last method was selected. Firstly, governing equations and boundary conditions of the problem are described, and the most important quantities are extracted.

The following sections define the governing equations and boundary conditions. Considering the problem is isothermal, only the liquid phase is necessary. This study considers that the gaseous phase has a negligible effect on it [24].

3.1 Governing equations

The previous sections described the theoretical part of sloshing dynamics. Section 4.2 describes a parametric study developed to obtain an optimal configuration for an anti-sloshing system. However, the study corresponds to a prototype tank, meaning that the similarity analysis is necessary to understand the effects of the full-scale model. Therefore, the following chapter's main objective is to set a scaling analysis so that similarity can be made.

In general, fluid dynamics problems are described by three main transport equations. Those correspond to the conservation of mass, the conservation of momentum, and the conservation of energy [13, 16, 25, 26, 27, 28]. This set of equations yields the Navier-Stokes equations, also known as Euler equations, where the fluid is considered inviscid.

The gas phase has a small mass compared to the liquid phase, so its influence can be neglected. The liquid phase is considered to be an incompressible fluid. Thus, from the application of the conservation of mass comes

$$\nabla \mathbf{V} = \frac{\partial u}{\partial x} + \frac{\partial v}{\partial y} + \frac{\partial w}{\partial z} = 0. \quad (3.1)$$

Conservation of momentum is also applied. This theory bases on Newton's Second Law relating the quantity of movement of a given body with the resultant force applied to it. For an incompressible, isotropic, Newtonian fluid, the viscous stresses are considered to be proportional to the rate of velocity and dynamic viscosity, yielding:

$$\tau_{ij} = \mu \left[\frac{\partial u_j}{\partial x_i} + \frac{\partial u_i}{\partial x_j} \right]. \quad (3.2)$$

Thus, the Navier- Stokes equations describe the movement of the liquid phase. For an incompressible and isothermic fluid, the Navier-Stokes equation is expressed as

$$\frac{D\mathbf{V}}{Dt} = \frac{\partial \mathbf{V}}{\partial t} + \mathbf{V} \cdot \nabla \mathbf{V} = -\frac{1}{\rho} \nabla p + \nu \nabla^2 \mathbf{V} + \sum F \quad (3.3)$$

in its vectorial form. The first member represents the total variation of momentum per unit mass of a fluid element, and the second member yields the total force applied to the fluid element [29]. If the forces applied result from the gravitic field, the second member rewrites as

$$\sum F = -\nabla \phi = -g \quad (3.4)$$

and substituting in Equation 3.3, becomes:

$$\frac{D\mathbf{V}}{Dt} = -\frac{1}{\rho} \nabla p + \nu \nabla^2 \mathbf{V} - \nabla gh. \quad (3.5)$$

3.2 Boundary conditions

Even though the main governing equations represent a crucial part of the problem, boundary conditions are also significant. Thus, the equations of boundary conditions need to be dimensionalized so proper scaling can be done.

The first Equation is related to the motion the tank is subjected, and that writes as

$$X(t) = A_f \sin(\omega t). \quad (3.6)$$

The reservoir walls are rigid and impermeable, which comes to the assumption of the no-slip condition. Thus,

$$\mathbf{V}_{fluid} = \mathbf{V}_{wall}. \quad (3.7)$$

At the free surface, denoted as $\eta(R, \theta, t)$, the vertical velocity at the interface must be equal for both phases, i.e.:

$$w_{liq} = w_{gas} = \frac{d\eta}{dt}. \quad (3.8)$$

At the free surface, the conservation of mass must be guaranteed so that,

$$m = \rho_L \left(\mathbf{V}_L - \mathbf{V}_i\right) \cdot \mathbf{n} = \rho_U \left(\mathbf{V}_U - \mathbf{V}_i\right) \cdot \mathbf{n}, \quad (3.9)$$

Where $\mathbf{V}_i, \mathbf{V}_L, \mathbf{V}_U$ is the velocity at the interface, liquid, and ullage, respectively. Equation 3.5 is also applied at the interface. The Laplace-Young equation introduces the effect of the surface tension through the pressure change across the interface:

$$\Delta p_i = -\sigma \left(\frac{1}{R_1} + \frac{1}{R_2}\right), \quad (3.10)$$

where R_1 and R_2 represent the principal radii of curvature that describe an arbitrarily-curved surface.

3.3 Dimensionless numbers

The dimensionless analysis is a helpful method to scale variables for experimental or numerical models of physical problems [30]. To use a dimensionless analysis it is necessary to identify variables and constants. Dimensional variables are the quantities that vary during the study. Dimensional constants are parameters that can vary. However, depending on the case of the study, they can be as constants. To do a proper scale and to know which

parameters must be scaled, the following guidelines must be followed:

- The variables and the constants must be identified to set the non-dimensionalization of the first ones;
- The non-dimensional values must be incorporated in governing equations and boundary conditions;
- Once the variables are substituted in the main equations, some characteristic numbers may appear and must be identified;
- The dimensionless numbers that appear must be correlated with the characteristic ones.

As seen before, the governing equations' main variables are velocity, time, pressure, and acceleration. So, the scaling is done by dimensionalizing these variables as follows [4, 12, 31, 32]:

Table 3.1: Adimensionalization of parameters.

Parameter	**Adimensionalization**
Velocity	$\frac{\mathbf{V}}{b\omega}$
Acceleration	$\mathbf{g}^* = \frac{\mathbf{g}}{g}$
Time	$t^* = \frac{tb\omega}{r}$
Pressure	$p^* = \frac{p}{\rho(b\omega)^2}$

In these equations, L represents the characteristic length which, in the case of lateral excitation, is equal to the tank radius. The characteristic velocity equals $b\omega$, where b is the wave's amplitude, and ω is the excitation frequency. Sloshing is a purely dynamic effect, yielding that dynamic pressure is enough to define the characteristic pressure.

Substituting Equations in Table 3.1 through Equations 3.1 to 3.10, the characteristic numbers presented in Table 3.2 appear.

The most significant adimensional number in fluid mechanical is the Reynolds number Re. In sloshing, this number estimates the liquid damping along the container walls [4]. The Froude number Fr appears from the consideration of the free surface since it defines the effect on it. Weber number We is only essential for the case where the surface's curvature is comparable with the depth of the liquid [33].

The liquid inside the reservoir moves accordingly to the resultant of four principal forces: capillary, body, inertia, and vicious. Figure 3.1 represents the relative importance of inertia, capillary, and gravity forces as a function of Weber and Bond numbers. If $\mathbf{We} \gg 1$, then the liquid is dominated by inertia forces. Froude Number dictates if the liquid is

Table 3.2: Dimensionaless numbers

Abbreviation	Name	Equation	Definition
Fr	Froude number	$\frac{(b\omega)^2}{gL}$	$\frac{\text{Inertia}}{\text{Gravity}}$
Re	Reynolds number	$\frac{\rho b\omega L}{\mu}$	$\frac{\text{Inertia}}{\text{Viscosity}}$
We	Weber number	$\frac{\rho(b\omega)^2 L}{\sigma}$	$\frac{\text{Inertia}}{\text{SurfaceTension}}$
Ga	Galilei number	$\frac{gL^3}{\nu^2}$	$\frac{\text{Gravity}}{\text{Viscosity}}$
Bo	Bond number	$\frac{\rho g L}{\sigma}$	$\frac{\text{Gravity}}{\text{SurfaceTension}}$

dominated by inertial or gravity forces. If $\mathbf{Fr} \gg 1$, liquid behavior is more influenced by the inertia forces than gravity ones. The influence of viscous effects are determined by the Reynolds number [34].

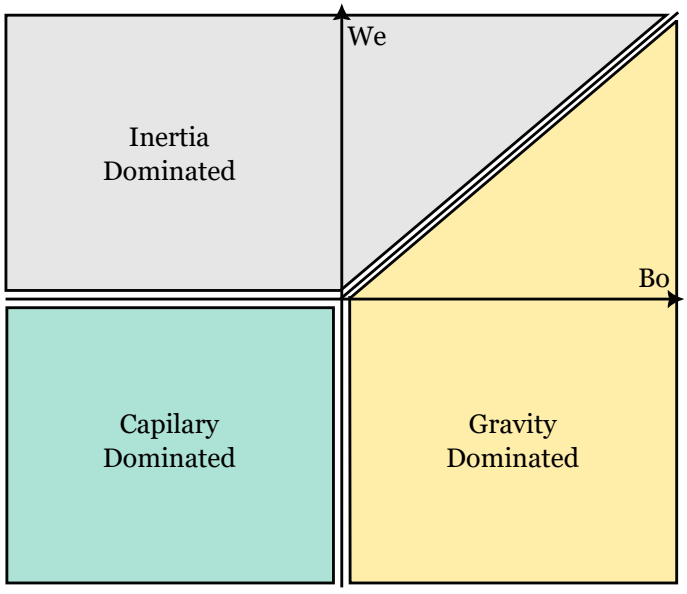

Figure 3.1: Hydrodynamic Regimes.

The dimensionalization of the boundary conditions originates the forcing amplitude ratio $A_s = \frac{A_0}{r}$ that relates the amplitude of the excitation with the radius of the tank. This guarantees that the original tank and the scaled one are under the same regime of sloshing. Additionally, the wave amplitude ratio $W_s = \frac{\omega}{\omega_{11}}$ that relates the amplitude of the wave with the radius.

3.4 Similarity Approach

3.4.1 Geometric Similarity

The geometric similarity is an essential phase in a scaling analysis. A small-scale model is similar to a full-scale model if all body dimensions in all three coordinates have the same linear scale ratio. Thus, the length scales must all be the same.

When baffles are geometrically scaled down in a model, the damping reduces, resulting in a decrease in the amplitude of the sloshing waves. However, the log decrement is used as a measure of damping. In that case, the decrease in damping due to scaling the baffles down in size is proportional to the scale ratio between the model and the prototype, meaning that the log decrement remains roughly the same between the model and the prototype. Thus, as long as the geometric scaling and slosh wave amplitudes are adequately accounted for, the drag damping due to baffles in a sub-scale model can be used to accurately predict the damping in a full-scale prototype [35].

The scaling coefficient is significant since the effects of the surface tension become more noticeable with reducing the tanks dimensions. Weber's number accounts for these effects. It relates the inertia of the fluid with the surface tension. Thus, if $\mathbf{We} \gg 1$, the surface tension of the fluid can be neglected. The tank studied corresponds to a tank with a radius of 146 mm and a height (of the cylindrical part only) of 205 mm. Thus, since the bigger scale corresponds to a tank with a radius of 486 mm and height of 681 mm, the scaling factor is 3.11.

$$\lambda = \frac{r_{Viriato}}{r_{small-scale}} = \frac{h_{Viriato}}{h_{small-scale}} = 3.33. \quad (3.11)$$

3.4.2 Kinematic Similarity

The kinematic similarity is achieved when the small-scale and full-scale models have the same length scale and time scale ratios. This ensures that, the velocity scale ratio will be the same for both models. Geometric similarity allows the same length scale ratio. However, to get the same time scale ratio, dynamic considerations are needed [27]. The kinematic similarity in frictionless flows with a free surface is done by equaling the Froude numbers, securing the scaling of the wave motion. Thus, using the Equation of the Froude number

$$\mathrm{Fr}_{Viriato} = \frac{(b_{Viriato}\omega)^2}{r_{Viriato}g} = \frac{(b_{small-scale}\omega)^2}{r_{small-scale}g} = \mathrm{Fr}_{small-scale}. \quad (3.12)$$

This sets that the behavior of the wave must be similar in both cases. Hence, the excitation amplitude ratio and the frequency ratio ω/ω_{11} similarity fixes the motion of the wave. The characteristic velocity $b\omega$, by introducing Equation 2.29, can be expressed by

$$b\omega = \underbrace{2\left[\frac{\left(\frac{\omega}{\omega_{11}}\right)^2}{1-\left(\frac{\omega}{\omega_{11}}\right)^2}\right]\left[\frac{\omega}{\omega_{11}}\right]}_{\text{constant.}}\omega_{11}A_f \quad (3.13)$$

The characteristic velocity $b\omega$ can be rewritten as

$$b\omega \propto \sqrt{\frac{g}{R}}A_f, \quad (3.14)$$

that when substituted in Equation 3.12 leads to

$$\mathrm{Fr}_{Viriato} = \left(\frac{A_{Viriato}}{r_{Viriato}}\right) = \left(\frac{A_{small-scale}}{r_{small-scale}}\right) = \mathrm{Fr}_{small-scale}. \quad (3.15)$$

Therefore, if the amplitude and frequency ratios are fixed, the kinematic similarity is ensured for cases where the inertia and gravity effects have equal importance [12].

3.4.3 Dynamic Similarity

Dynamic similarity occurs when the models have the same length scale, time scale, and force ratios. Geometric similarity is mandatory, while kinematic and dynamic similarities co-occur. The flow is incompressible, in order to have similarity, the Froude, Reynolds, and Weber must be equal.

Figure 3.2a relates the Reynolds number of the full-scale model using LOx and the small-scale model using water. Understandably, the small-scale has a Reynolds number approximately 1.33 times smaller than the original Viriato tank. A higher damping is noticed for the small scale, since the viscous tensions are higher. It is essential to understand if the surface tension effects can be neglected on a small scale. This is related to the Weber number represented in Figure 3.2b. Understandably, Viriato's tank has a high Weber number, signifying that the inertia forces have a more significant impact than the surface tension. Nevertheless, the small-scale has a Weber number almost 70 times smaller, denoting that the surface tension starts to have a meaningful effect. However, in both cases, the Weber number is much higher than one, purporting that the effects caused by the tension of the

fluid surface can be neglected.

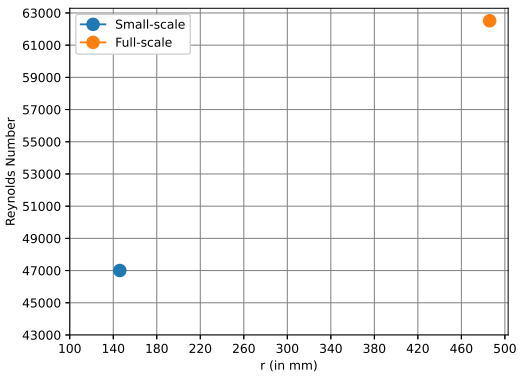

(a) Reynolds number in the function of the radius for the full-scale and small-scale.

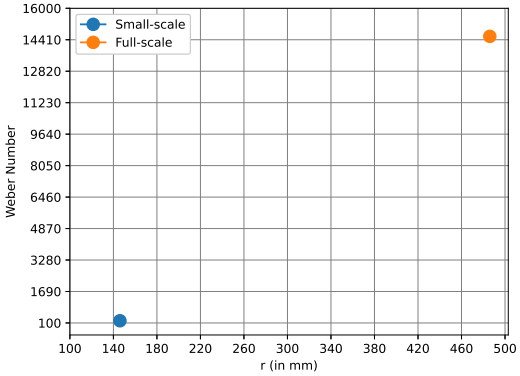

(b) Weber number in the function of the radius for the full-scale and small-scale.

Figure 3.2: Kinematic similarity.

Chapter 4

Anti-Sloshing Devices

4.1 State Of Art

Sloshing is a phenomenon that encompasses a range of possible issues in vehicle operations, resulting in the generation of detrimental moments and forces that impact the vehicle's stability, control, and safety [36, 37]. To mitigate this occurrence, devices that counteract sloshing, commonly called baffles, are installed in tanks in various configurations. This section presents a review of studies that have explored anti-sloshing devices, by means of numerical simulations, experimental investigations, or a combination of both, and presents their findings and conclusions.

Panigrahy et al. [37] performed an experimental study in a rectangular tank with dimensions 600×600×600 mm to observe the displacement of the free surface, considering different baffles when the frequency of oscillation and the level of water varies. Horizontal devices consisted of flat plates with dimensions of 600×120 mm, with four holes were placed in the tank's half height. Vertical baffles were placed in the half-width of the tank with dimensions of 600×200 mm with four holes with a diameter of 76 mm. Also, a case of ring baffles with small holes was considered. The authors concluded that when the water hits the anti-sloshing devices, the kinetic energy of the fluid reduces. Thus, the movement of the free surface is dampened. Observing the variation of pressure in the unbaffled case and the three where baffles were considered, the authors observed that the pressure variations decreased significantly, suggesting that the ring baffles are the best option. Ring baffles reduce the velocity of the impact of the fluid at the walls and retards the vertical motion of the liquid, absorb the energy and dissipate it to the walls instead of concentrating it in the ones normal to the direction of the excitation.

Maleki et al. [38] investigated the hydrodynamic damping of sloshing in a seismic context using vertical and horizontal baffles, comparing the analytical results with the experimental. The authors utilized two ring baffles of 5 and 7.5 cm in width placed perpendicular to the excitation axis in a cylindrical tank with a diameter of 100 cm and a height of 120 cm . The study showed that the ring baffles dampen slender tanks when situated close to the liquid surface. For tanks where the ratio of liquid height with tank radius is more than two, the sloshing mode affects a depth close to $2r$. Thus when this ratio increases, the influence of baffles in this sloshing mode is less notable. The authors concluded that the damping ratio depended on tank and baffle dimensions, as well as its location and sloshing height amplitude. The authors also observed that when the relative liquid height is between 50%

and 100% of the total height, the utilization of baffles keeps the relative sloshing amplitude constant. When baffle placement was at a height lower than 0.766 of the relative liquid height, the damping ratio increased as the relative liquid height increased. Lastly, as the distance between baffles increases damping ratio increases.

Akyildiz et al. [39] experimentally analyzed the effect of different configurations and arrangements of two baffles in a cylindrical tank under pitch oscillations. The main parameters changed in each case were the width of the baffle and its vertical location in the tank. This study allowed the authors to conclude that ring baffles decrease the variation of pressure in the container, thus provoking lower loads. Also, the authors observed that the best configuration was when the baffles were at a greater distance from each other, and the larger baffle was at the top.

Garza et al. [17] studied the effect of baffles with variable thickness in a cylindrical tank under lateral oscillation. Rings had a fixed ratio of w/r of 0.157 and a variable thickness from 0.046 cm to 0.076 cm. This study involved diverse materials from solid sheet to sheet with holes with 30% of the area removed. Experimental results were compared with analytical ones obtained through the Miles equation. The employment of solid rings indicated a good agreement between experimental and analytical values when the baffle was well below the liquid free surface. However, when this distance d/r is less than 0.125, experimental values showed higher damping than the analytical ones. The utilization of perforated ring baffles showed that damping is less than when solid rings were considered. For perforated baffles, with a perforation area less than 16%, results exhibit that damping increases a lot. However, this study concluded that the area of the baffles could be reduced by 23% with perforations without reducing damping. Lastly, an implementation multiple baffles was tested, since it provides more damping for a higher range of liquid levels. The utilization of ring baffles affects the liquid natural frequencies. If a ring is located right below the free surface, the natural frequency increases compared to the unbaffled case. However, the natural frequency decreases if the baffle is deep.

Dodge et al. [40] experimentally evaluated the effect of ring baffles in the damping of a cylindrical tank. These baffles were made of aluminum with 0.51 mm of thickness and 15.2 mm of width. The number of baffles varied from one, three, and five, equally spaced. The experiment revealed that the number of baffles increased with the moment of inertia of the liquid. The authors compared the damping with similar baffled tanks and observed that it was about fifty to one hundred times less. Also, when compared with the unbaffled tank, it was concluded that the log decrement of a baffled tank was much higher.

Concerning the available literature, ring baffles are preferred for cylindrical tanks subjected to lateral oscillations. In fact, Maleki et al. [38] stated that ring baffles effectiveness is independent of liquid oscillation. Consequently, the ring baffle can be the optimal solution. Furthermore, it is imperative to consider specific parameters that may significantly affect fluid dynamics, such as baffles' width, number, location, and spacing.

4.1.1 Anti-sloshing devices

Ring baffles are the most common geometry used to reduce the undesired movement of the fluid. Ring baffles are mainly used because of their excellent performance under lateral oscillations. They are sometimes used with porous materials or even with holes. However, other types of devices must be accounted for.

In some cases, lids are utilized to cover the free surface of the liquid and follow its movement as it goes up or down. When this geometry covers at least 85% of the tank diameter, its effect is noticed, and sloshing is damped. Porous floating mats are also used in the same movable device configuration since it increases the viscous effects on the free surface. However, these devices can be stuck on the tank's internal components. Thus, its application in the spacecraft field could be more practical.

For cases where it is necessary to transfer liquid in a low gravity field, or when the flow wants to be increased without a pump, flexible diaphragms are used, since they provide an impermeable barrier between the liquid and the gas. The device is fixed around the periphery of the tank wall.

Additionally, the devices have other types of geometries: conical, vertical, and cruciform [41, 42]. Figure 4.1 represents different types of configurations and geometries for suppression devices.

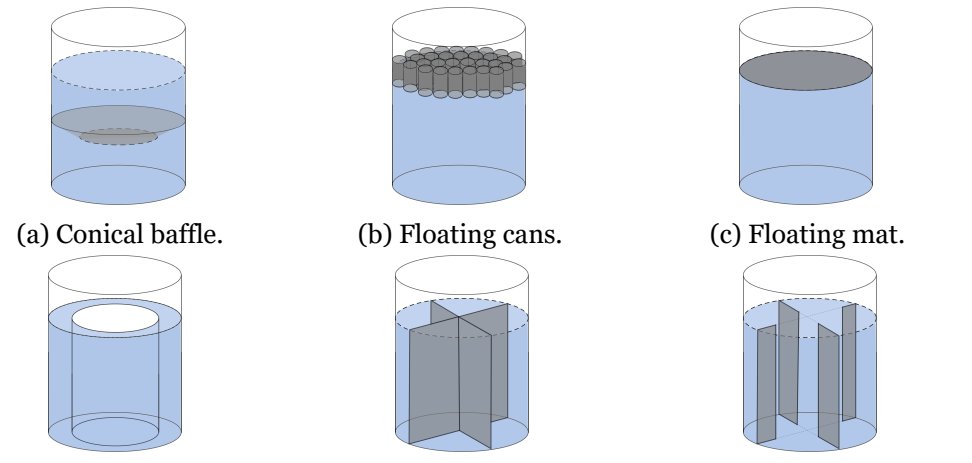

(a) Conical baffle. (b) Floating cans. (c) Floating mat.

(d) Annular tank. (e) 90°sectioned tank. (f) Cruciform baffled tank.

Figure 4.1: Representation of different types of suppression devices and tanks.

Event though, there are other types of anti-sloshing systems or geometrical solutions, this work will focus on studying ring baffles. This anti-sloshing, as reviewed above, are the most commonly used system and seems to be the ones with the best performance, specially for space vehicles applications [22]. Furthermore, ring baffles present a very good compromise between performance and weight, which in space applications is important.

4.2 Parametric Study

As mentioned before, anti-sloshing devices have the goal of controlling the liquid's movement. Therefore, designers must follow requirements when designing an anti-sloshing system. The first one consists of the minimum damping, since this is a requirement in some designs. At the same time, the implementation in a tank must have a minimum penalty in weight and volume. This is also important so that operations, such as emptying or cleaning, do not suffer any interference. Anti-sloshing devices absorb some forces and torques produced by the liquid. Thus, these systems must absorb the forces and moments and uniformly distribute them to tank structure [43].

A parametric study is often developed to have an initial insight into the best configuration for an anti-sloshing system. In this section, a parametric study is explained. This was constructed under Bauer's extension [22] of the Miles equation. The main objective of this study is to understand which is the best configuration of baffles for a prototype tank to understand which variables would be parameterized in the numerical study.

4.2.1 Model description

The Bauer's extension [22] was utilized to study the effects of baffle width w, number of baffles n, the distance between baffles D and the position of the baffle y on the damping of sloshing motion. Figure 4.2 represents the variables used in the parametric study.

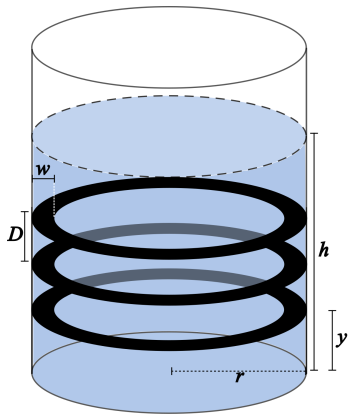

Figure 4.2: Representation of a tank with n baffles, each one with a width w, at a distance D from each other, being the first one at position y.

The tank is cylindrical with a radius of 0.146 m and height of 0.205 m (considering only the cylindrical part), with an infill percentage varying from 25% to 90%. Pérez et al. [35] stated that a good design principle would be spacing baffles at a distance of $D \leq 0.2r$, also, referring that if the distance between baffles is higher that its width, Equation 2.24 does not correctly predict damping.

Equation 2.24 only applies within certain limits, one of them referring to the amplitude

of the sloshing wave, which must be $\zeta \ll r$. Furthermore, if the amplitude exceeds 10% of the diameter of the tank, the wave behavior becomes nonlinear. Hence, the higher slosh amplitude that is reasonably assumed equals to $0.2r$ [14]. Therefore, the wave amplitude was assumed as $\zeta = 0.15r$. The amplitude of liquid oscillation was set to be constant, since Pérez et al. [35] mentioned that the design of ring baffles is based on choosing the best configuration for their length, spacing, and distance from the free surface.

Taking that statement into account, a test matrix was chosen to observe the effect of different values of variables. Table 4.1 reports the values utilized for the parametric study. In the parametric study, the parameters were the number of baffles n, the distance between baffles D, the position of the higher baffle y, and the baffle width w.

Table 4.1: Test matrix utilized for the parametric study utilizing the extension of Miles equation developed by Bauer.

Width [m]	Number of baffles	Position [m]	Distance between baffles [m]
$0.05r$ $0.08r$ $0.11r$ $0.14r$ $0.20r$	1	$0.2h$	-
		$0.5h$	-
		$0.75h$	-
	2	$0.2h$	$0.1r$
			$0.2r$
			$0.3r$
		$0.5h$	$0.1r$
			$0.2r$
			$0.3r$
		$0.75h$	$0.1r$
	3	$0.2h$	$0.1r$
			$0.2r$
			$0.3r$
			$0.4r$
		$0.5h$	$0.1r$
			$0.2r$
			$0.3r$
	4	$0.2h$	$0.1r$
			$0.2r$
			$0.3r$
		$0.5h$	$0.1r$
			$0.2r$
	5	$0.2h$	$0.1r$
			$0.2r$
		$0.5h$	$0.1r$

The maximum number of baffles was chosen based on the limits of Equation 2.24. The theory could not predict a good result for baffles distance below a baffle width. Also, a good design principle would be the placement of the baffles at a maximum distance of $0.2r$ [35]. Thus, $n = 5$ was the maximum number that could account for the different limits, especially the distance between baffles.

4.2.2 Results And Conclusions

4.2.2.1 Effect Of Baffle Width

Baffle width corresponds to the difference between the inner and outer radius of the device. When comparing results for different widths, it was observed that as the width increases, damping also increases. Figure 4.3a shows that for a width of $0.2r$, the damping is more significant than for a minimum width of $0.05r$. This occurs because, with the increase in width, the cross-sectional area of the baffle also increases, which corresponds to a more damped motion of the liquid. A wider ring baffle will have more surface area in contact with the medium than a narrower one, which can dissipate more energy. This increased dissipation leads to higher damping, which can benefit applications where damping is desired, such as shock absorbers or vibration dampeners. Thus, it is observed that damping ratio tends to increase with a larger baffle. Although, the analytical model only allows a study until a maximum width of $0.2r$ which means that in the numerical model, a greater width must be included so its effect can be appropriately determined.

4.2.2.2 Effect Of Baffle Position

The position of the first baffle (corresponding to the lowest one) varied from $0.15h$ to $0.8h$. Figures 4.3a and 4.3b represent the effect of damping for two different baffle locations. Considering the case of one ring baffle, it was seen that appears a peak in damping value in this location, and then it decreases exponentially. For a baffle with a width of $0.2r$, the maximum damping corresponded to a value of 0.15. The maximum value did not suffer any alteration from the variation of position. This means that the behavior of the wave was linear and only translated for the position where the baffle was located. That occurs because the theory for the used equation is based on sloshing linear dynamics.

When considering a higher number of baffles, with the variation of other parameters, it was seen that the higher the location of the baffle, the larger the damped region (Figure 4.3). Thus, the preferred location corresponded to $0.8h$, since it extends damping in height.

4.2.2.3 Effect Of Baffle Distance

The distance between baffles is related to the position factor, as the distance between baffles gives the position of devices above the first one. Figures 4.3e and 4.3c represent the damping ratio variation using two rings and a constant distance between baffles. Following linear dynamics, as position increased, the peaks and their exponential behavior translated to a higher range, i.e., the curves moved for an LH% where the baffles were located, not changing its damping maximum value. Considering a constant position, as can be seen in Figures 4.3c and 4.3d, it was observed that, as the baffle distance increases,

the maximum damping decreases. Considering a position of $0.5h$, for distances of $0.1r$, $0.2r$, and $0.3r$, the maximum damping value was approximately 0.2, 0.18, and 0.15, respectively.

4.2.2.4 Effect Of Number of Baffles

The number of baffles is also crucial since, in general, more baffles, more damping. As mentioned before, the number of baffles varied between 1 and 5. As the number of baffles increased, the number of peaks also increased. The damping of a system can increase with the number of baffles because each baffle creates additional surfaces for the surrounding medium to interact with, which can increase the amount of energy dissipated as the system oscillates. Figures 4.3f, 4.3g and 4.3h exhibit the results for 3, 4 and 5 baffles, being positioned at the same initial position and distanced with the same distance. It is seen that after three baffles, a relevant difference in the value of maximum damping was not noticed. Thus, to see the difference between each configuration, the integral of each curve was obtained through the Trapezoidal Rule. It concluded that the mean damping also increases as the number of baffles increases. It is also understandable that as the baffling number increases, the range of damping becomes wider. This occurs because the surfaces will damp a higher area of the liquid.

4.2.3 Optimization Study

In the parametric study, the distance between baffles was set to be equal for all, i.e., equally spaced. However, it was thought that equally spaced could not be the best option, so an optimization study using the Powell method was developed to obtain the better configuration.

4.2.3.1 Powell Method

Powell's method is an optimization algorithm used to find the minimum of a multivariate function. It belongs to the class of derivative-free optimization methods, meaning it does not require the function to have a known derivative to find the minimum [44].

This method works by interactively searching along a set of directions updated during each iteration. At each iteration, the algorithm performs one-dimensional searches along each direction using a line search method, such as golden section search or parabolic interpolation, to find the minimum in that direction. The minimum point found in all the one-dimensional searches is taken as the new estimate of the minimum point, and the set of directions is updated to reflect the new search space. The process is repeated until the convergence criteria are met [44].

The advantage of Powell's method is that it can handle nonlinear and non-smooth functions and does not require any information about the gradient or Hessian of the function being minimized. Additionally, the method can efficiently handle high-dimensional problems by exploiting the correlations between the search directions.

4.2.3.2 Definition Of Optimization Function

The main objective of this work is to design an anti-sloshing system that provides the maximum mean damping possible, which is obtained by doing tyhe integral of the curve. Thus, the optimization function is based on this principle. As mentioned before, no significant difference is noticed in the maximum damping of the configurations after a certain number of baffles. Therefore, the most accurate factor was seen to be the mean damping. Mean damping is obtained through an integral. In this case, the Trapezoidal method was used to resolve the integral. This method states that

$$\int_a^b f(x)dx \approx \sum_{k=1}^{N} \frac{f\left(x_{k-1}\right) + f\left(x_k\right)}{2} \Delta x_k \quad (4.1)$$

where $f(x)$ is the function, x_{k-1} is the previous value of x, x_k is the x value of the current position k and Δx_k is the difference between the two positions.

In python, the Powell Method is available in the library scipy. The vector of optimization $\mathbf{x}$ is defined as expressed in Equation 4.2. In order to obtain a result, an initial value of $\mathbf{x}$ must be introduced. A random search algorithm was employed for this initial value, where the code chose aleatory initial values. Besides that, some boundary values must be given to the function. Those were inserted according to the limits of the analytical model. Since the introduction of the number of baffles as a variable was not possible because of the complexity of variables and initial solutions, the optimization code was run for the case of three, four, and five baffles. This configurations were chosen, since the initial study allowed to understand that the damping ratio would be favorable for a number of baffles higher than three.

$$\mathbf{x} = \begin{Bmatrix} w \\ y \\ D_1 \\ \vdots \\ D_{n-1} \end{Bmatrix} \quad (4.2)$$

4.2.3.3 Results and conclusions

The following results were obtained through the optimization study:

Table 4.2: Results obtained through the optimization study.

n	w, m	y, m	D_1, m	D_2, m	D_3, m	D_4, m
3	0.0292	0.0504	0.0210	0.0589	-	-
4	0.0292	0.0428	0.01098	0.0162	0.0584	-
5	0.0291	0.0448	0.0203	0.0177	0.0169	0.0576

For the case of 3, 4, and 5 baffles, the optimized integral value equaled 0.01935, 0.0257, and 0.03162, respectively. This result corroborates the conclusion that more baffles permit a more damped fluid movement. Through the results in Table 4.2, it is possible to conclude that the damping increases with the width, which took the optimal result for this variable to be the same even for different numbers of baffles.

With the analytical theory, for three-ring baffles, the higher mean value of damping is around 0.0195, which occurs for baffles with the maximum width, the first at a position of 0.041 m and the distancing equal to 0.016 m. When different spacing is allowed, the value of the integral is 0.01935, which is lower than the equal spacing. In the first case, the highest baffle is positioned at 0.0968 m, and in the second case, the same baffle is at 0.1298 m. This means that different spacing leads to a higher height of damping. However, the liquid damping is later in this case because the first baffle is almost five times higher than with equal spacing.

The implementation of four baffles, according to the first parametric study, allows the conclusion of a maximum mean damping of 0.0198 when the first ring is at 0.041 m of the bottom and the distance between each of the four rings is 0.043 m. Compared to both cases with three baffles, the damping ratio is higher when one more is added. For a second case, with four baffles displaced at positions according to the results shown in Table 4.2, the integral value equals 0.0257. The difference from the configurations mentioned before is very high. This means the different spacing is a real benefit as the baffles increase.

Regarding the configurations with five baffles, the higher damping is obtained for the first baffle at a position of 0.041 m with a distancing of 0.029 m, resulting in 0.0279 for the mean damping ratio. Considering equal distancing between ring baffles, as the number of baffles increases, so does the mean damping ratio. This can conclude that more baffles lead to a better result. The optimization configuration for the five baffles implementation led to a mean damping value of 0.0316. The difference between these results and the others is very high, almost three times higher than the best configuration of three equally distanced baffles.

Considering these results, it is understandable that five-ring baffles lead to a more stabilized movement of the liquid. The implementation of three baffles is less beneficial than the others. Thus, only configurations of four and five baffles were tested to reduce the

Table 4.3: Configurations to be implemented in the numerical and experimental model.

n	w, m	y, m	D_1, m	D_2, m	D_3, m	D_4, m
4	0.030	0.041	0.044	0.044	0.044	-
4	0.030	0.043	0.020	0.016	0.058	-
5	0.030	0.041	0.029	0.029	0.0292	0.029
5	0.030	0.048	0.020	0.018	0.017	0.058

test matrix. Hence, Table 4.3 shows the configurations to be modeled in CFD and the experimental model.

However, it was observed that the damping also increases by increasing the width of the ring. Thus, a configuration with baffles two times larger will be experimentally tested.

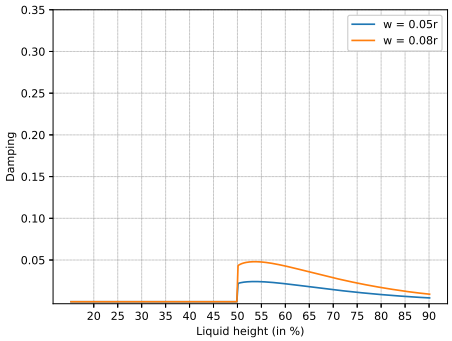

(a) $n = 1, y = 0.1025\text{m}$

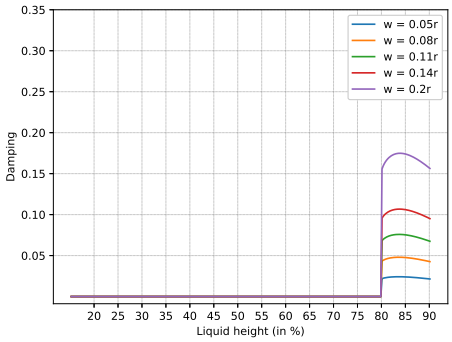

(b) $n = 1, y = 0.164\text{m}$

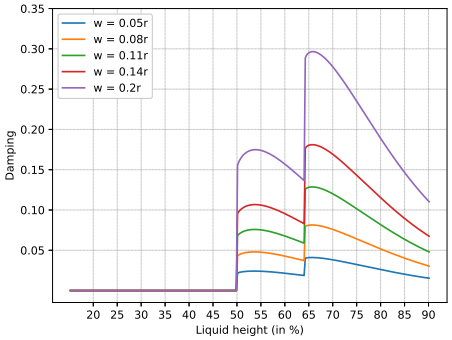

(c) $n = 2, y = 0.1025\text{m}, D = 0.0292\text{m}$

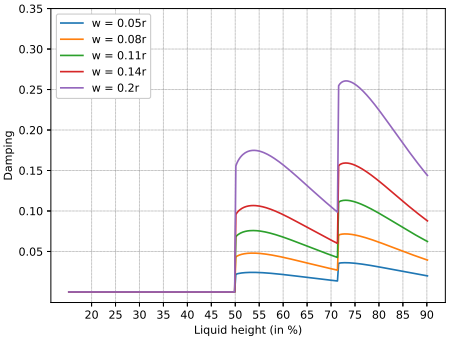

(d) $n = 2, y = 0.1025\text{m}, D = 0.0438\text{m}$

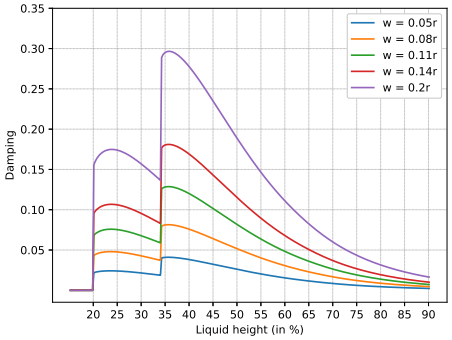

(e) $n = 2, y = 0.041\text{m}, D = 0.0292\text{m}$

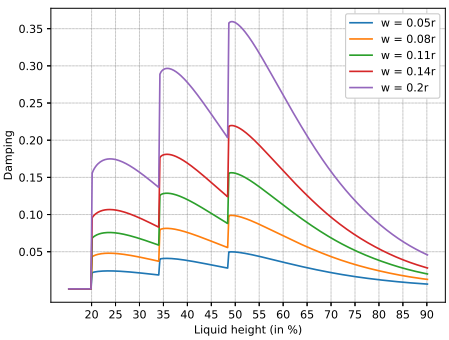

(f) $n = 3, y = 0.041\text{m}, D = 0.0292\text{m}$

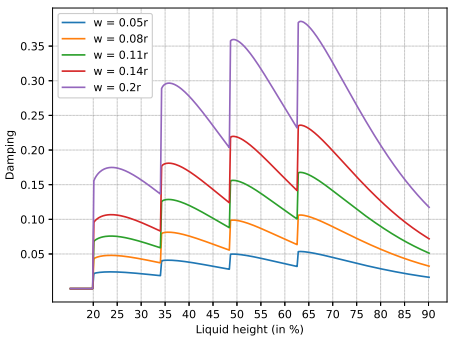

(g) $n = 4, y = 0.041\text{m}, D = 0.0292\text{m}$

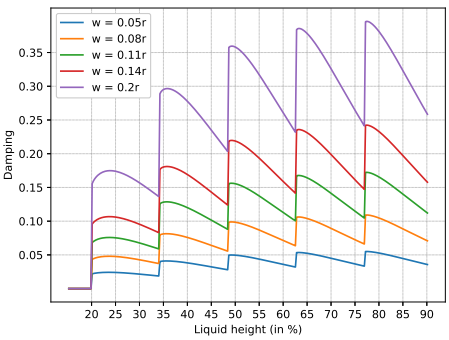

(h) $n = 5, y = 0.041\text{m}, D = 0.0292\text{m}$

Figure 4.3: Damping in the function of liquid height percentage for different number of baffles n, varying position y and baffle distance D.

Chapter 5

Numerical model

5.1 State Of Art

The movement of the liquid induces forces and momentums that influence the vehicle's stability. Understanding and predicting, the behavior of the liquid becomes crucial to teh successful design of the space vehicle. Numerical models are a powerful approach to estimate the movement of the fluid and is employed within the space of this work . The following section briefly resumes some numerical methods utilized for different sloshing problems.

Rebollo et al. [28] performed a numerical study of the liquid dynamics inside a rectangular reservoir with baffles. The numerical study implemented in ANSYS Fluent® solving the Navier-Stokes equations through Finite Volume Method (FVM). To decide which turbulent model was the best for the problem, the authors used different turbulence models and validated them with experimental data from Okamoto et al. [45]. Numerical results obtained with the Large Eddy Simulation (LES) turbulence model showed better agreement with the experimental results. In the LES model, WALE was the SubGrid-Scale Model selected. The interface was simulated with the Volume Of Fluid (VOF) model. For the solution methods, the pressure-velocity scheme chosen was Pressure-Implicit with Splitting of Operators (PISO), since it promotes momentum balancing after every pressure correction. The Green-Gauss-Cell-based method was employed to compute the gradients required to solve the scalar values and the velocity derivatives. The pressure spatial discretization was done through Pressure Staggered Option (PRESTO!) method.

Liu et al. [46], Hou et al. [47] and Wei et al. [32] implemented a numerical study in ANSYS Fluent® employing the k-ε turbulence model. The VOF model was applied, selecting the interface modeling type as sharp/dispersed. Hou et al. [47] adopted the explicit VOF formulation. In the case of Hou et al., [47], the convective term discretization was selected as first-order upwind, while for the other two situations, the selection was second-order upwind. The authors opted for the PISO scheme, and the pressure-velocity coupling was captured by the PRESTO! In the numerical study of Liu et al. [46], the mesh was created in the ICEM software, considering a 2D mesh (to save computational costs). To implement the sinusoidal excitation of the tank, the authors developed a User Defined Function (UDF). The objective of this numerical model was to study the sloshing dynamics considering liquids with different initial temperatures in a cryogenic tank. On the other hand, Hou et al. [47] aimed to see the effect of different external oscillations in the dynamic

of a liquid considering a 2D rectangular tank. In this case, the excitations were imposed resorting to the dynamic mesh technique. In the numerical model validation for the case with a single excitation were compared the results with the ones from Godderidge et al. [48]. Wei et al. [32], focusing on the filling process of a liquid hydrogen tank. Through diverse excitation amplitudes and frequencies, different sloshing conditions were implemented.

Singal et al. [49] implemented a numerical model to study the introduction of baffles in a rectangular tank partially filled with kerosene. As in the other bibliography references, the VOF method was employed. The pressure-velocity coupling option used was the fractional step algorithm, since the flow is time-dependent. The spatial discretization for gradient was defined as Green-Gauss Node Based.

George et al. [50] investigated the effect of a vertical porous baffle placed in a rolling rectangular tank through an analytical and numerical models validated by an experiment. A 3D implicit turbulent model employing incompressible unsteady Reynolds Averaged Navior-Stokes (RANS) equations was modulated by the k-ε realizable model. The interface was modulated with VOF method. For pressure coupling, differently, from most authors, SIMPLE was selected, and second-order upwind discretization was employed for momentum.

Modaressi-Tehrani et al. [36] implemented a laminar numerical study applying VOF. Momentum and pressure correction equations were discretized using the first-order upwind and body-force-weighted schemes. The spatial components of the governing equations were also discretized with a fixed time step, using the first-order time advancing scheme. In this case, the objective was to investigate the effects of baffles and the consideration of a transient fluid.

Liu et al. [51] studied three roll-induced sloshing cases in order to conclude which of the modeling approaches more suitable, evaluating the results through a comparison with experimental results from Delorme et al. and Souto-Iglesias et al.. The considered models were laminar, k-ε Standard, LES, and VLES (Very Large Eddy Simulation). The results showed that VLES and LES agreed very well with the experiment, even on the shape of a plunging water jet in the front part of the wave. In the case of RANS and laminar models did not occur. The primary reason for the poor performance of RANS is that the k-ε model it was developed using a time-averaging approach. At the same time, the plunging wave-breaking process exhibits significant flow unsteadiness.

Storage reservoirs are commonly used to store liquids such as chemicals, and their resistance to movements (such as earthquakes) is critical to understand if they can hold the forces and momentums. Thus, Yazici et al. [52] utilized past earthquakes data to study the sloshing response inside a reservoir filled with naphtha under excitations with large displacements of the ground and long vibration periods. This study used ANSYS Fluent. Pressure-based and transient analysis used VOF to have a better modulation of the free

surface and used the Realizable k-ε method to model turbulence. The discretization of the pressure equation was made using PISO. The gradient was discretized through Least Square Cell-based, and the convection term and the turbulent kinetic energy were discretized through first-order upwind. The discretization method used for pressure was the PRESTO! In this case, the authors opted for an unstructured mesh with inflation layers on the walls for a better prediction of the response at the boundary layer.

The effect of baffles and their position in a cylindrical upright container was studied by Gopalakrishnan et al. [53]. This study considered an oscillating motion of amplitude 2 mm and a frequency corresponding to the natural frequency in a reservoir with different fill ratios. The numerical model implemented in ANSYS Fluent® was pressure-based transient and used explicit formulation for VOF. The fluids used were air and water, and the time step was varied so that the Courant number was beyond 250 to allow convergence.

Using the OpenFoam software, Marques [4] studied the movement of the fluid considering both a non-isothermal and an isothermal sloshing problem. As the authors previously mentioned, Marques used VOF to model the immiscible multiphase flow.For the analysis,the temporal scheme was the first-order implicit Euler, and for the gradient and Laplacian terms, the discretization method used was second-order Gauss Linear. The divergence terms were discretized with second-order total variation diminishing flux-limiting van Leer scheme. The flow was considered to be laminar.

Suyal [42] used ANSYS Fluent® to model the movement of the fuel inside a tank of a moving vehicle.. The problem involved a vehicle that initializes its movement from a rest position and then accelerates for a few seconds. Once it reaches a given velocity, the vehicle starts to drive with a null acceleration and then breaks suddenly, reducing its velocity abruptly. The tank was analyzed for those with no baffles and with different types of baffles. The two-phase flow was modulated using the k-ε model and VOF with the explicit formulation. For this problem, the fractional step method ensured the coupling of pressure with velocity. The discretization of the gradient was done with the least square cell-based method. The discretization methods of momentum and pressure were power-law and body-force weighted, respectively.

As discussed above, different methods were used by different authors. In table 5.1 is a summary of the cases reviewed above. It is possible to understand that there is a tendency for some methods of modulation. In the case of the viscous model, the most common model used us the k-ε standard which we may conclude that can be the best approach for this type of problem. Moreover, it is seen that the pressure-velocity coupling and the pressure discretization methods are mostly the same in the cases modulated in ANSYS Fluent ®. The VOF modulation is concluded to be necessary for the simulations. In the subsequent sections, the methods used in this work are detailed.

Table 5.1: Summary of the numerical models used by the cases mentioned in the state of art.

Authors	Viscous model	Multiphase	Pressure-velocity coupling	Convective term discretization	Gradient discretization	Pressure discretization
Rebollo et al. [28]	LES, WALE	VOF	PISO	Second-order upwind	Green-Gauss cell based	PRESTO!
Liu et al. [46]	k-ε standard	VOF explicit	PISO	Second-order upwind	-	PRESTO!
Hou et al. [47]	k-ε standard	VOF explict	-	First-order upwind	-	PRESTO!
Wei et al. [32]	k-ε standard	VOF	PISO	Second-order upwind	Green-Gauss cell based	PRESTO!
Singal et al. [49]	-	VOF explicit	Fractional step algorithm	-	Green-Gauss node based	-
George et al. [50]	k-ε realizable (y+ wall treatment)	VOF	SIMPLE	Second-order upwind	-	-
Modaressi et al.[36]	Laminar	VOF	PISO	First-order upwind	Green-Gauss cell based	Body-forced weight
Liu et al.[51]	Laminar	VOF	-	Central difference combined with upwind	-	-
Yazici et al.[52]	k-ε realizable	VOF	PISO	First-order upwind	Least-square cell-based	PRESTO!
Gopalakrishnan et al.[53]	Laminar	VOF explicit	-	-	-	-
Marques et al. [4]	Laminar	VOF	-	Second-order Gauss Linear	Second-order Gauss Linear	-
Suyal et al. [42]	k-ε standard	VOF explicit	Fractional-step method	Least- square cell-based	Power-law	Body-force weighted

5.2 Numerical Model

CFD allow us to obtain a numerical solution to problems with fluid flows. This simulation involves five steps [25]:

- Step 1: The physics of the problem should be defined, which means selecting the mathematical model, including the desired level of solution accuracy.
- Step 2: This refers to the discretization process in which the geometry and the mathematical model are translated into algebraic equations. Thus, the discretization of the space consists of partitioning the geometry into divisions creating a grid or mesh. After that, the discretization of the mathematical model can be undertaken.
- Step 3: This phase is where the numerical scheme is analyzed, and the solution's stability and accuracy are evaluated.
- Step 4: The resolution phase refers to selecting the most appropriate methods to resolve the numerical scheme. This includes determining boundary conditions and ways to accelerate the convergence process.

– Step 5: The last step refers to the post-processing phase, where the relevant physical quantities are evaluated examined and interpreted.

The following section describes the main concepts of each component of the numerical model and the options chosen for the case study. Figure 5.1 shows a flowchart that contains all the steps of the numerical model for the case in the study.

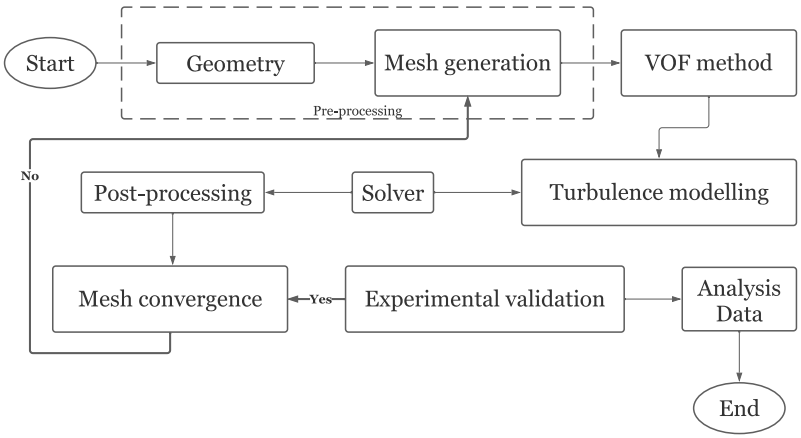

Figure 5.1: Numerical model flowchart.

5.2.1 Geometry and mesh

The tank was designed using the Solidworks® software, in order to generate the 3D geometry. The numerical grid was obtained using the ANSYS® meshing. The definition of the geometry created an unstructured mesh by default. However, structured meshes are often desired in numerical models, since they allow more accurate results [25]. Therefore, the geometry was divided into 18 parts, to obtain a structured grid. A square was designed in the top plane of the tank occupying approximately 18% of its area. The geometry of the tank was axially divided using the square geometry. The remaining cylinder body was vertically divided into eight parts. The whole body was then divided horizontally at the desired liquid height.

Since the desire was to generate a structured grid, the multiphase method was applied to the middle cubic body, to enhance the creation of quadratic elements. The edges created by the divisions of the cylindrical body were subjected to a bias factor, to provide a better aspect ratio of the elements.

A mesh convergence study was made to understand the numerical grid's influence on the results. This consisted of a decrease in the element size. To have the same increase of elements from case to case, the following relations were assumed:

$$\begin{aligned} N_x \times N_y \times N_z &= N_T \\ \sqrt[3]{c}N_x \times \sqrt[3]{c}N_y \times \sqrt[3]{c}N_z &= cN_T \end{aligned} \quad (5.1)$$

ANSYS®enables an option called **Use adaptative sizing** in which the mesh size is specified in specific domain regions to achieve better resolution in areas of interest such as the interface. Moreover, adaptative meshing can be used dynamically and coarsened during the simulation based on criteria such as VOF. This allows a coarser mesh on the liquid phase and refines it in the interface with minimal elements. Thus, both of these options are of good use since a better mesh can be obtained in the interface, which is the most important in the simulations [54, 55].

5.2.2 Boundary Conditions

As mentioned before, the motion of the tank is defined by a harmonic function described as

$$x(t) = A_0 sin(\omega t). \quad (5.2)$$

whose first and second derivative with respect to time yield the following expressions for velocity and acceleration, respectively

$$\begin{aligned} \dot{x} = v(t) &= A_0 \omega cos(\omega t) \\ \ddot{x} = a(t) &= -A_0 \omega^2 sin(\omega t) \end{aligned} \quad (5.3)$$

The values of A_0 and ω are chosen according to the mission's requirements and theory. Requirements say that the lateral acceleration that the tank will be subjected to is around four m/s. The movement of the tank must be defined such that the regime of the sloshing remains stable planar, since the theory predicts damping ratio for linear conditions. Thus, taking as basis theory explained in Chapter 2, the conditions are chosen to have the biggest value of acceleration for values relatively close to the frequency of the first modal mode and also values that allow an amplitude of the wave that is under the limits of the analytical model. This takes to the point where $\omega/\omega_{11} = 0.65$ and $A_f/r = 0.38$. This yields a maximum acceleration is around 2.87 m/s^2, and a maximum displacement at the wall of $0.55r$.

As mentioned in Sub Section 2.3, there are different ways to measure damping in the tank. In this work, the damping is measured through wave amplitude decay. Damping is measured by oscillating the tank with a frequency around the frequency of the first mode,

and once it reaches a steady state behavior, the tank is quickly stopped. Thus, an UDF (User Defined Function) is introduced in ANSYS Fluent® so that this methodology can be modeled. Besides that, the experimental model uses an electric motor that provides a sudden acceleration to the tank in a small period. Thus, the UDF accounts for this rapid acceleration and deceleration to have numerical results close to the experimental model.

5.2.3 Turbulence

In Section 3.1, the governing equations were exposed, and the Navier-Stokes equations were obtain to describe the problem. This set of equations describes the behavior of the flow from laminar to turbulent. In the last case, the turbulence can be modeled from different models. The most detailed method to resolve the numerical problem is Direct Numerical Simulation (DNS) which computes all the scales [56]. Large Eddy Simulation (LES) can only compute the large scales with an exact solution, and the small scales are resolved by the subgrid-scale method. However, these modulations of turbulence have a high computational cost, and in most problems, their use is not justified. Thus, the Reynolds-Averaged Navier-Stokes (RANS) are commonly used and provide a good solution. In the RANS model, the value of a given quantity ϕ is given by Equation 5.4 where the first member corresponds to averaging the quantity to time and the second corresponds to its fluctuation [56].

$$\phi(\mathbf{x}, t) = \bar{\phi}(\mathbf{x}, t) + \phi'(\mathbf{x}, t) \quad (5.4)$$

The averaging of ϕ is given by Equation 5.5 where T is an averaging period that is longer than the period of the fluctuations.

$$\bar{\phi} = \frac{1}{T}\int_0^T \phi(\mathbf{x}, t)dt \quad (5.5)$$

For an incompressible fluid, the averaging of the Navier-Stokes equations is given by

$$\begin{aligned} &\frac{\partial \bar{u}_i}{\partial x_i} = 0 \\ &\frac{\partial \bar{u}_i}{\partial t} + \frac{\partial \bar{u}_i \bar{u}_j}{\partial x_j} = -\frac{1}{\rho}\frac{\partial \bar{p}}{\partial x_i} + \frac{\partial}{\partial x_j}\left[v\left(\frac{\partial \bar{u}_i}{\partial x_j} + \frac{\partial \bar{u}_j}{\partial x_i}\right) - \tau_{ij}\right] + f_i + \frac{1}{\rho}F_i^{ST} \end{aligned} \quad (5.6)$$

In this set of equations, the overbar denotes the averaging of the components to time, and τ_{ij} is the turbulent stress tensor resulting from the averaging of Navier-Stokes equations

[56, 54, 29, 57].

Considering those above, the Navier-Stokes are rewritten by averaging each quantity. For a case, such as the one in the study, of a Newtonian fluid, the averaging of the governing equations becomes:

$$\begin{aligned} \nabla \cdot (\rho \overline{\boldsymbol{u}}) &= 0 \\ \frac{\partial \rho \overline{\boldsymbol{u}}}{\partial t} + \nabla \cdot (\rho \overline{\boldsymbol{u}}) &= -\nabla \bar{p} + \nabla \cdot \left(\overline{\boldsymbol{\tau}} - \rho \overline{\boldsymbol{u'u'}} \right) + \overline{\boldsymbol{f}} \end{aligned} \tag{5.7}$$

These equations bring the appearance of a term that introduces 6 additional unknown variables and is called Reynolds stress tensor $\tau^R = -\rho\overline{\boldsymbol{u'u'}}$. Thus, the turbulence models appears to resolve unknown variables by introducing new equations. Turbulence models are an approach that reduces the unknown variables for the number of equations available by reducing Reynolds stresses to mean values. This can be done by expressing the Reynolds stresses as a linear function of the mean velocity gradients, which can be written as

$$\boldsymbol{\tau}^R = -\rho\overline{\boldsymbol{u'u'}} := \mu_t \left[\nabla \overline{\boldsymbol{u}} + (\nabla \overline{\boldsymbol{u}})^T \right] - \frac{2}{3} \left[\rho k + \mu_t (\nabla \cdot \overline{\boldsymbol{u}}) \right] \boldsymbol{I} \tag{5.8}$$

where the turbulent kinetic energy is equal to

$$k = \frac{1}{2} \overline{\boldsymbol{u'} \cdot \boldsymbol{u'}}. \tag{5.9}$$

and μ_t is the turbulent kinetic energy. The calculation of Reynolds stress is based on the Boussinesq Hypothesis that allows the approximation of the result through the calculation of turbulent kinetic energy and turbulent viscosity. The turbulence models $k-\varepsilon$, and $k-\omega$ are based on the Boussinesq theory having two transport equations. The $k-\varepsilon$ model calculates turbulent eddy viscosity as follows

$$\mu_t = \rho C_m u \frac{k^2}{\varepsilon} \tag{5.10}$$

where ε is the dissipation rate of turbulent kinetic energy obtained using physical reasoning, this model assumes that the flow is fully turbulent and that the effects of the molecular viscosity are neglected. To model an internal or external flow, a first idea of how it will behave is necessary. The two variables k and ε are obtained through the following transport equations

$$\begin{aligned}
\frac{\partial}{\partial t}(\rho k) + \frac{\partial}{\partial x_i}(\rho k u_i) &= \frac{\partial}{\partial x_j}\left[\left(\mu + \frac{\mu_t}{\sigma_k}\right)\frac{\partial k}{\partial x_j}\right] + G_k + G_b - \rho\varepsilon - Y_M + S_k \\
\frac{\partial}{\partial t}(\rho\varepsilon) + \frac{\partial}{\partial x_i}(\rho\varepsilon u_i) &= \frac{\partial}{\partial x_j}\left[\left(\mu + \frac{\mu_t}{\sigma_\varepsilon}\right)\frac{\partial \varepsilon}{\partial x_j}\right] + C_{1\varepsilon}\frac{\varepsilon}{k}(G_k + C_{3\varepsilon}G_b) - C_{2\varepsilon}\rho\frac{\varepsilon^2}{k} + S_\varepsilon
\end{aligned} \tag{5.11}$$

in which G_k is the generation of turbulence kinetic energy due to the mean velocity gradients, G_b is the generation of turbulence kinetic energy due to buoyancy, Y_M is the contribution of the fluctuating dilatation in compressible turbulence to the overall dissipation rate, $C_{1\varepsilon}$, $C_{2\varepsilon}$ and $C_{3\varepsilon}$ are constants, σ_k, and σ_ε represent the turbulent Prandtl numbers for k and ε, and S_k and S_ε are user-defined source terms [1]. The $k-\varepsilon$ model has three variations: Standard, RNG(Renormalization Group), and Realizable. The RNG model contains an additional term in the ε equation, improving the accuracy for rapidly strained flows, providing better results in cases where swirl is present, and the user-defined values in the standard model are obtained through an analytical formula. The realizable model uses an alternative equation formulation for the turbulent viscosity, and the transport equation of ε is derived from an exact equation for the transport of the mean-square vorticity fluctuation.

The $k-\omega$ model uses the turbulence kinetic energy k and its specific dissipation rate ω. When compared to the $k-\varepsilon$ model, this one incorporates modifications for low-Reynolds, effects of compressibility, and spreading of shear flow spreading. The transport equations of these quantities are written as

$$\begin{aligned}
\frac{\partial}{\partial t}(\rho k) + \frac{\partial}{\partial x_i}(\rho k u_i) &= \frac{\partial}{\partial x_j}\left(\Gamma_k \frac{\partial k}{\partial x_j}\right) + G_k - Y_k + S_k \\
\frac{\partial}{\partial t}(\rho \omega) + \frac{\partial}{\partial x_i}(\rho \omega u_i) &= \frac{\partial}{\partial x_j}\left(\Gamma_\omega \frac{\partial \omega}{\partial x_j}\right) + G_\omega - Y_\omega + S_\omega
\end{aligned} \tag{5.12}$$

where G_k represents the generation of turbulence kinetic energy due to mean velocity gradients, G_ω is the generation of ω, Γ_k, and Γ_ω is the effective diffusivity of k and ω, Y_k and Y_ω represent the dissipation of k and ω due to turbulence, and S_k and S_ω are user-defined source terms.

The $k-\omega$ model suffered some modifications over the years, which brought variations to the model. Thus, the variations of this model are the Standard and the SST (Shear-Stress Transport). The SST model differs from the Standard by incorporating a damped cross.-diffusion derivative term in ω equation, turbulent viscosity definition is modified so the transport of the turbulent shear stress is guaranteed and the value of the constants are different in the transport equations.

The Reynolds number was calculated for the original and the scaled tank, and was guaranteed that both were under the same regime. The value of the adimensional number allowed us to understand that the flow inside the tank is turbulent, which implies the usage of the numerical model. The literature review allowed us to conclude that most authors use the $k-\varepsilon$ model. Besides that, based on the study of Liu et al. [51] and Rebollo et al. [28] is possible to understand that for a numerical analysis on a rectangular tank, the $k-\varepsilon$ RNG model with a standard wall function allows a better approximation between CFD and experimental results than the $k-\omega$ model. The RNG model has a variation to account for swirl effects, but since the flow is expected to have a linear behavior, the Standard scheme was considered enough.

An important factor when using turbulence models is related to the wall treatment. The no-slip condition that needs to be satisfied at the wall affects the mean velocity field. Nevertheless, the turbulence is changed by the presence of walls. The accuracy of numerical solutions is strongly affected by the near-wall treatment since it is near walls that solution variables have more significant gradients, moments, and scalar transports.

Near-wall treatment can be divided into three layers. The closest layer to the wall is the viscous sublayer, where the flow is almost laminar, and the viscous effects dominate momentum and heat equations. The outer layer denominates the fully-turbulent layer. The effects of molecular viscosity and turbulence are equally crucial in the layer between these two [1].

Near-wall regions can be modeled in two different ways. The first one is by using wall functions. Those semi-empirical formulas connect the region affection by viscosity in the wall and the fully-turbulent region. In the second approach, the turbulence models modify so that the region affected by viscosity is resolved. This is done using a mesh extending to the wall, including the viscous sublayer.

Wall functions include a significant value denominated y^+. y^+ is the distance of the first mesh node to the wall. If this value is too high, the boundary layer is crossed; if it is too small, it enters the viscous sublayer. This parameter often brings convergence problems since its value can provoke complications at the first node causing an error at pressure drop and velocity [57].

5.2.4 Volume Of Fluid

The volume of fluid allows us to model two or more immiscible fluids solving the momentum equations. Besides that, this model allows us to have better information about the behavior of the interface [58, 59, 60]. However, VOF model has some limitations. This model can only be used with a pressure-based solver, and all the control volumes must be filled with a fluid phase or a mixture of phases. Hence, only one of the phases can be modeled as a compressible ideal gas. The principle of this model is based on the value of

a variable κ. If κ is equal to 1, the cell is filled with liquid; if it equals zero, it means that the cell is occupied with gas. If the variable is between 0 and 1, it defines the cells crossed by the free surface. Figure 5.2 shows a representation of the volume fraction in a series of cells, and **n** which represents the normal vector on each cell[59].

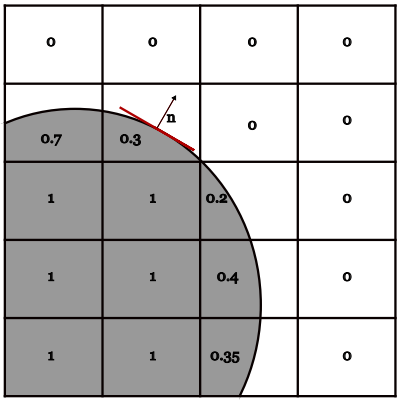

Figure 5.2: Representation of the volume of fraction.

The gradient of κ determines the direction of the free surface. Thus the position of the surface can be given as

$$\frac{\partial \kappa}{\partial t} + \nabla(\kappa \mathbf{u}) = 0 \quad (5.13)$$

which, according to the continuity equation for an incompressible flow (in which $\nabla \mathbf{u} = 0$), gives the transport equation of the volume fraction as

$$\frac{\partial \kappa}{\partial t} + u\frac{\partial \kappa}{\partial x} + v\frac{\partial \kappa}{\partial y} + w\frac{\partial \kappa}{\partial z} = 0. \quad (5.14)$$

This equation solves the system of continuity, momentum, and energy equations for the entire multiphase flow, allowing for tracking of the displacement of the free surface [1].

Once κ is determined, the fluid properties are computed for each cell based on the individual fluid properties and fraction volume.

5.2.4.1 Volume of Fraction in ANSYS Fluent®

In ANSYS Fluent®, some parameters must be chosen, such as the model formulation and discretization.

The formulation can be divided into implicit and explicit. The implicit scheme uses ANSYS's Fluent® standard finite-difference interpolation schemes to obtain the flux at the

face of all cells. This scheme requires the values for the volume fraction at the current time step, which implies that the standard scalar transport equation is solved interactively for each of the secondary-phase volume fractions at each time step. On the other hand, in explicit scheme of the interpolation, the previous time step is considered in the evaluation to the volume fraction. This does not require using an iterative solution of the transport equation during each time step.

Different methods in ANSYS Fluent® can do the the free surface interpolation. The Geo-reconstructor and the donor accept schemes. are two examples The Geometric Reconstruction Scheme obtains the face fluxes of a filled cell by the standard interpolation schemes. This scheme calculates the interface using a piecewise-linear approach, bringing a more accurate scheme, especially in cases with unstructured meshes. The donor-acceptor scheme identifies a cell as the donor of a certain amount of fluid from one phase and another cell as the acceptor of that same amount of fluid.

5.2.5 Solution Methods

5.2.5.1 Pressure-velocity Coupling

The model uses momentum and pressure as the primary variables, i.e., it is pressure-based. In this problem, the pressure equation is derived from a numerical algorithm that combines continuity and momentum equations. This is referred to as pressure-velocity coupling.

ANSYS Fluent® has five methods for pressure-velocity Coupling: SIMPLE, SIMPLEC, Coupled, Fractional Step, and PISO. SIMPLE is the default method and uses a relation between velocity and pressure to enforce mass conservation and to obtain the pressure field. SIMPLEC is similar to SIMPLE, but the expression used for the face flux correction differs. Typically, these two methods are used in steady-state cases. PISO (Pressure-Implicit with Splitting of Operators) is based on the higher degree of the approximate relation between the corrections for pressure and velocity. This scheme improves the efficiency of calculating velocities and their fluxes, enhancing the balance of the momentum equation by introducing the neighbor and the skewness correction. The first is an iterative process that moves the repeated calculations of SIMPLE and SIMPLE inside the solution stage of the pressure-velocity coupling equation. After some loops, the corrected velocities more closely satisfy the continuity and momentum equations. The PISO method is highly recommended for transient flows, especially in cases where the Implicit method is used and where the mesh has a high degree of distortion. The fractional Step Method is only used when the Non-Iterative Time Advancement option is enabled, reducing the computationally cost [1, 54].

5.2.5.2 Discretization Scheme

For spatial discretization, ANSYS Fluent® has four options: the First and Second-Order Upwind Schemes, QUICK, and Third-order MUSCL. From those options, Second-Order Upwind and QUICK Schemes have the best characteristics to be used in this problem.

Second-Order Upwind computes the variable through a multidimensional linear reconstruction approach. This allows the achievement of high accuracy of the variable through a Taylor series expansion of the cell-centered solution about the cell centroid. Thus, the following formula describes how the variable's value is obtained through this scheme.

$$\phi_f = \phi + \nabla\phi \cdot \vec{r}. \quad (5.15)$$

QUICK allows obtaining a high-order value of a variable ϕ at a face cell based on a weighted average of second-order-upwind and central interpolation. Considering a control volume as defined in Figure 5.3, the value of ϕ in face e is given by the following formula

$$\phi_e = \theta \left[\frac{S_d}{S_c + S_d}\phi_P + \frac{S_c}{S_c + S_d}\phi_E \right] + (1-\theta)\left[\frac{S_u + 2S_c}{S_u + S_c}\phi_P - \frac{S_c}{S_u + S_c}\phi_W \right] \quad (5.16)$$

where S_k, S_ε, and S_ω are User defined source terms. If $\theta = 1$, the interpolation is done through a central-second order upwind value, and if $\theta = 0$, the equation is equal to the one of the second-order upwind. However, $\theta = \frac{1}{8}$ is the base for QUICK scheme. This scheme allows to obtain a more accurate value of the variable on structured meshes.

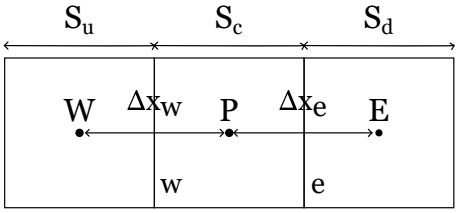

Figure 5.3: One-Dimensional Control Volume [1].

5.2.5.3 Gradients

The gradients are used to compute the secondary diffusion terms and velocity derivatives and to get values of variables at faces. These gradients can be computed from the Green-Gauss Cell-Based, Green-Gauss Node-Based, and Least Squares Cell-based.

The Green-Gauss Theorem uses the following Equation to compute the gradient of a variable ϕ at the center of a cell.

$$(\nabla\phi)_0 = \frac{1}{\mathcal{V}} \sum_f \bar{\phi}_f \vec{A}_f \quad (5.17)$$

Figure 5.4 represents the faces of two cells. If the Green-Gauss Cell-Based method is used, the value of ϕ at the center cell face 0 is obtained by doing an average with the values of the following cells, as described by the following equation.

$$\bar{\phi}_f = \frac{\phi_0 + \phi_1}{2} \quad (5.18)$$

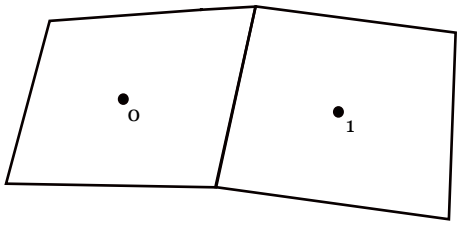

Figure 5.4: Representation of the faces of cells 0 and 1.

In the case of the node-based method, $\bar{\phi}$ is estimated by doing an average weight of the variable in the nodes of the cell, as represented in Figure 5.5, i.e.,

$$\bar{\phi}_c = \frac{1}{N_f} \sum_n^{N_f} \bar{\phi}_n. \quad (5.19)$$

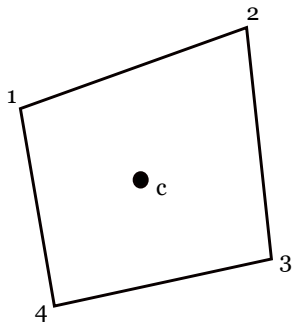

Figure 5.5: Representation of a face cell and its nodes.

The Green-Gauss Node-Based is more accurate than the cell-based method, especially in the case of unstructured meshes, but its computational cost is also higher.

The Least Square Cell-Based method assumes that the solution of the gradient varies linearly. Figure 5.6 represents the change in cell values 0 and 1 along the distance between centroids, which can be expressed as

$$(\nabla\phi)_0 \cdot \Delta r_1 = (\phi_1 - \phi_0) \quad (5.20)$$

Here, the coefficient matrix $[J]$ represents the geometry-dependent coefficients. The main objective is to determine the gradient of the cell, given by

$$\left(\nabla\phi_0 = \phi_x\widehat{i} + \phi_y\widehat{j} + \phi_z k\right), \quad (5.21)$$

by solving the minimization problem for this non-square coefficient matrix system in a least-squares manner.

The linear system can be decomposed, resulting in a matrix of weights for each cell. Consequently, for the cell-centered approach, this implies that three components of the weights $\left(W^x_{i0}, W^y_{i0}, W^z{}_{i0}\right)$ are generated for each face of cell 0 to face cell i.

Hence, the gradient at the cell center can be computed by multiplying the weight factors with the difference vector $\Delta\phi = (\phi_1 - \phi_0)$, yielding:

$$\begin{aligned}
(\phi_x)_0 &= \sum_{i=1}^{n} W^x_{i0} \cdot (\phi_i - \phi_0)\,; \\
\left(\phi_y\right)_0 &= \sum_{i=1}^{n} W^y_{i0} \cdot (\phi_i - \phi_0)\,; \quad (5.22) \\
(\phi_z)_c &= \sum_{i=1}^{n} W^z_{i0} \cdot (\phi_i - \phi_0)\,.
\end{aligned}$$

Both least square and node-based methods allow a more accurate result than cell-based. However, the Least Square has a lower computationally cost than the node-based. The mesh in use is a structured mesh; the usage of node based is unnecessary since the Least Square results allow a very accurate result.

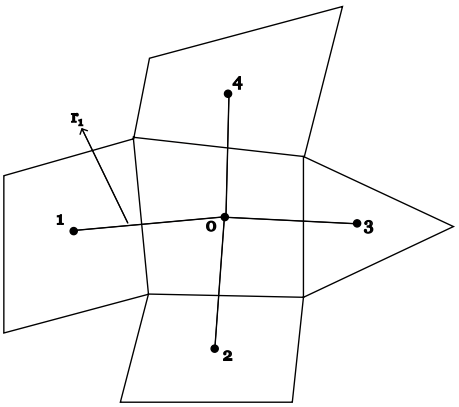

Figure 5.6: Representation of least-square-based.

Chapter 6

Experimental Model

6.1 State Of Art

As referenced in Section 4.1, Akyildiz et al. [39] developed an experimental study using a reservoir with 800 mm of height and 695 mm of diameter equipped with two ring baffles with widths of 10 cm and 5 cm, all components made of plexiglass material. The pressure at the container's wall was acquired using nine pressure transducers installed at different heights and radial positions. An analog-digital converter in the platform obtained the displacement of the wave. The test platform could rotate the tank about a transverse axis through its center by an arrangement moved with energy given by a DC motor.

Sakib et al. [61] developed and designed an experimental setup to study sloshing with an economical budget. The authors assumed that as the liquid moves, its Center of Gravity (CG) also moves along the axis of the force applied. Therefore, if the volume of the liquid is known, a load cell is enough to discover its displacement. Thus, a triple-axis accelerometer was fixed on one side of the container to provide the relationship between the movement and the force. The reservoir was rectangular, with a length of 19 cm, breadth of 9 cm, and height of 15 cm. The base was attached to an aluminum frame. One of the sides was fixed to a load cell of 5 kg. The movement of the water resulted in a change in the weight acting in the load cell because the distance CG changes relative to the load cell.

Panigraphy et al. [37] utilized a shaking table moved by a cam arrangement moved by a DC motor. The tank was bolted in a platform, placed in a concrete basement, and connected with the cam arrangement by rods. A V-belt connected The arrangement with the DC motor's shaft. Six pressure transducers were placed at different heights and faces.

Foreest et al.[24] and Arndt et al. [31] used the same test rig. An electric engine moved a platform on three grooved ball bearings, using a shaft to connect both. The tank was cylindrical with a lower dome and was secured to the platform with the help of a polyacetal lid. The reservoir consisted of two glass layers having a vacuum space between them to minimize the heat transfer phenomena. Two glass-reinforced plastic retainers with four temperature sensors were placed inside the tank to obtain the temperature results in the gaseous phase. In the liquid phase, a similar retainer was allocated underneath the free surface carrying five sensors. Two propellants were utilized: GN_2 and GHe. Foreest et al. [24] focused on studying the thermodynamic effects due to sloshing. Arndt et al. [31] wanted to study the coupling between those thermodynamic effects with pressurization.

Scholl et al.. [62] aimed to observe the effect of the ring baffle presence on the pressure distribution and the damping in large cylindrical tanks. The cylindrical tank made of steel had two long, narrow anti-swirl plates placed vertically along the walls. Two baffles were utilized, one able to change position to identify the effects of distance between baffles. Two strain-gage differential-pressure transducers were sealed from the water and positioned on the baffles to measure the pressure variation on the baffles. One strain-gage differential-pressure transducer measured the displacement amplitudes.

Lloyd et al. [63] studied the effect of different baffle designs on longitudinal road tankers. The experiments were made using a one-sixth scale model. Thus, similarity analysis allowed to obtain the relation between the small-scale and full-scale models. A strain gauge, pressure transducers, and accelerometer enabled the acquirement of results. The tank was made with perspex, and the baffles were fixed in the inner walls through four thin steel poles. These steel poles ran the length of the tank and were secured by a metal ring. Placement of the tank on rails allowed the excitation with the desired acceleration.

The influence of baffles in the damping of cylindrical liquid storage tanks was studied by Maleki et al. [38]. The tank was made of steel and was oscillated through the use of a shake table. One load cell measured the driving force on the table. Three accelerometers were installed in the tank body and one in the table. Also, four strain gauges, placed in the tank walls, measured the pressure. Four bolts at different locations hung the rings inside the tank walls.

6.2 Experimental Setup

As a way of validating the numerical model and, simultaneously, the results obtained in the parametric study, an experimental model was developed. Thus, this section pretends to describe the techniques used for the measurements and construction of the rig. This setup was fully developed to be used to study sloshing effects in future similar projects. Also, the scaling of the tank had to be done since the main tank would occupy a massive space, and the necessary force to move it would be much more significant. This takes to the development of a compact setup. In addition, the desire was to have an automated setup to provide accurate and repeatable results.

6.2.1 System's design

Sloshing is a phenomenon that is interest to visualize, and therefore the first idea was to have a tank entirely made of plexiglass. However, it was seen that would not be a good idea since the domes were very complicated to machine, and most companies would not do that. Thus it was opted to construct a tank with plexiglass and aluminum.

Figure 6.1a shows the tridimensional CAD of the setup developed. In this representation

(1) refers to all the tank geometry. The cylindrical part, where most of the sloshing phenomenon occurs, was chosen to be seen through. Therefore a plexiglass tube of 292 mm in diameter, thickness of 4 mm, and height of 205 mm was used to recreate the cylindrical part of the tank. Both domes were machined from aluminum blocks. Figure 6.1b shows one dome and it is possible to see the features on the inner thickness. This is because this domes were designed to have a 5 mm space, such as the plexiglass tube, so that they could fit perfectly in each other. Besides that, to avoid leaks in the tank a housing of 4 mm was added so that an o-ring could fit in it. One of the problems with a geometry with an elliptical dome is how to fix the full geometry. The most simple way to do so is by a flange. Thus, both domes had a flange with 2 cm of width. This flanges were connected to each other through of six M6 threaded rods and M6 threaded nuts. This allowed to secure both domes and also to connect the tank to the rest of the setup. Pressure was measured through the use of three pressure transducers placed on the lower dome in different radial positions.

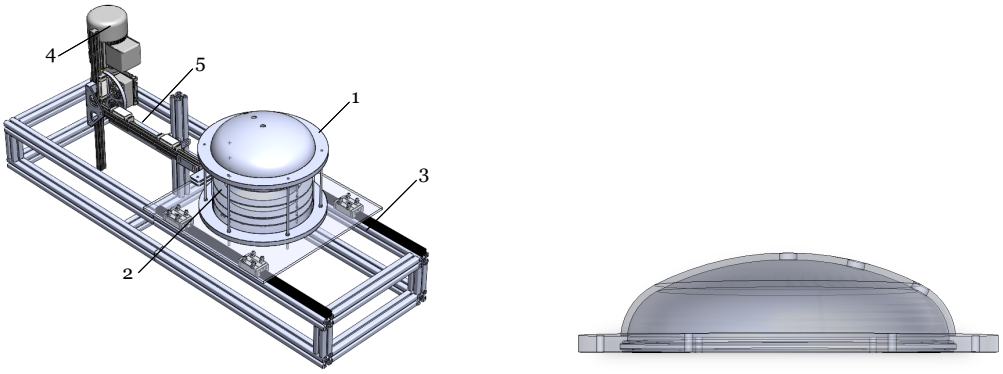

(a) Full setup. (b) Dome.

Figure 6.1: CADs of the experimental setup.

Referring to baffles (2), it was implicit that its structure must be easy to get in and out of the tank. Besides that, the definition of the position of the rings must be simple since different configurations need to be tested. Thus, the solution consists of a ring with a smaller width and 3 mm thickness secured between the upper dome and the tube. The ring is designed so its effect on the flow is the minimum possible. Besides that, it is expected that the water does not arises at such a high point. This ring was perforated with four M3 holes along its circular area, such as the baffles. This ring was connected to the ring baffles with the help of four M3 threaded rods and a bunch of M3 threaded nuts that allowed to position the baffles in the desired position.

The rig (2) developed to secure the tank was composed by different parts. The oscillation table consisted of an aluminum plate of $500 \times 500 \times 8$ mm machined with a hole in the center with exactly the size to fit the lower dome. The threaded rods used in the tank also passed through the plate being all fixed with M6 threaded nuts (can be seen with more detail in Figure 6.3b). To allow the excitation movement, a linear rail system was employed. The pretended excitation is defined by a sinusoidal function that moves the tank

laterally, meaning the tank moves in only one direction. The linear rail system comprises two rails and ball guides that move along the rails. Since the facility has some weight, four ball guides were connected to the aluminum plate for more effortless movement and for a more distributed weight. The rails were fixed to horizontal aluminum extruded profiles. The horizontal profiles were connected with four vertical aluminum extruded profiles, and on the bottom two horizontal profiles were fixed. This structure is shown in Figure 6.2b.

To provide the excitation to the table an electric engine (4) with a power of 0.12kW was used. Since the engine provides a rotary motion and the desired is to be linear a Scotch-Yoke mechanism (5) was utilized.

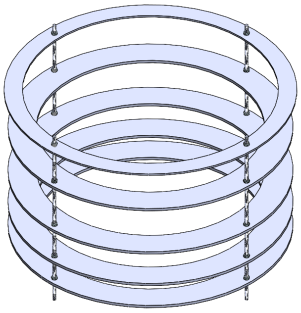

(a) Baffles system for the experimental model.

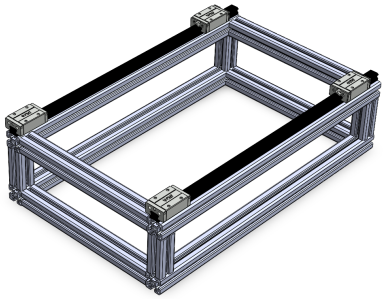

(b) rig used to fix the facility.

Figure 6.2: CADs of the experimental setup.

(a) Full experimental setup.

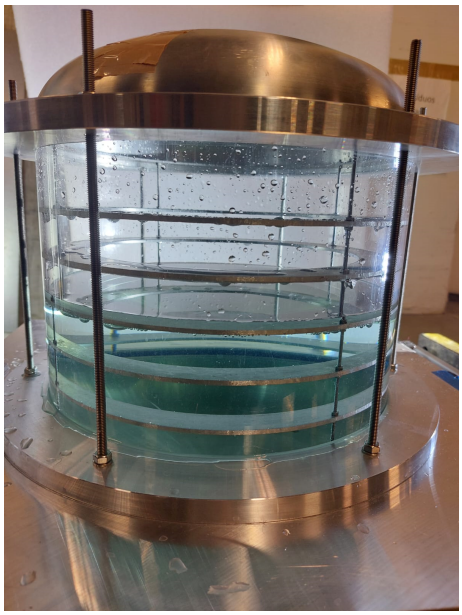

(b) Tank details.

Figure 6.3: Experimental setup photographs.

6.2.2 Instrumentation

The facility has some electronic components that must be mentioned in this chapter. To move the platform, an electric engine is required. Besides that, to understand the effects of the excitation in the tank pressure transducers are used.

6.2.2.1 Acceleration monitoring

The acceleration provided by the electric motor is monitored by an accelerometer which allows a correct and efficient input of excitation. However, an accelerometer is positioned on the displacement table to ensure that the acceleration is correctly defined. The one in use corresponds to a three axis accleramoter that allows to motorize the three axis making sure that only one direction of excitation is applied. This sensor is glued in the front of the aluminum plate ensuring that the direction of the three axis is in the correct direction of the movement (Figure 6.4).

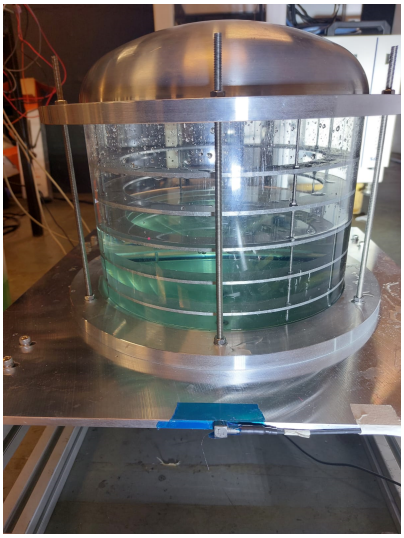

Figure 6.4: Tank and accelerometer.

6.2.2.2 Pressure measurement

Pressure measurements are done using three Pa642P-50mbarg-A4AV-00-000 (Figure 6.5a) type pressure transducers disposed on the lower dome of the tank. These pressure transducers are positioned in different radial positions to understand the pressure variations. These sensors can monitor pressures with a range of 50 mbar.

Pressure transducers measure the pressure of a fluid by evaluating the force it exerts when in contact with a surface. Furthermore, pressure values are converted into an analog electric signal. Pressure transducers include a force collector and a transducer element that uses a dependent resistive, capacitive, or inductive method to generate an electric signal.

Moreover, it uses strain gauges that suffer deformation, creating a change in voltage and allowing the measurement of the acting force.

The lower dome is perforated with three G1/4 male holes in different radial positions to measure the pressure in different locations. The connection of the pressure transducers uses two wires. This type of wiring means that two wires are connected in series with the load. The pressure transducers were connected to a power supply (Figure 6.5b) that allows to provide voltage to the sensors.

To read the values acquired by the transducers, an acquisition board was used. This board was connected to the computer where a LabVIEW program allowed to visualize the curves and save all the data. The data was saved in voltage values. To convert this to pressure in Pascal a linear correlation is used. The minimum value that the transducer can read correspond to 0 Pa and 0.7 V, and the highest value correspond to 5000 Pa and 3.5V. This lead to the following equation:

$$p = \frac{5000}{2.8}V - 1250 \quad (6.1)$$

(a) Pa642P-50mbarg-A4AV-00-000 pressure transducer [64].

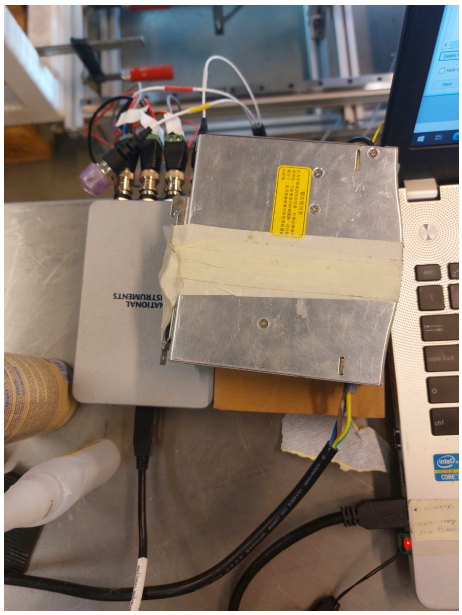

(b) Acquisition board and power supply.

Figure 6.5: Pressure instrumentation.

6.2.2.3 Tank motion

The excitation of the tank is dictated by the Equation 5.3. In order to move platform an electric engine is used. However, the engine provides a rotational motion that must be transformed into a linear one. To do so, a Scotch-Yoke mechanism is used since it provides

a perfected sinusoidal movement contrary to, for example, the crank-shaft mechanism.

This mechanism comprises a wheel, a sliding yoke system, and a connecting rod. The wheel is connected on one side to the engine shaft, which causes its movement. The shaft of the engine is connected to the wheel. The wheel has a shaft that is connected to a bearing in an aluminum plate fixed in a guide. This guide then moves along a rail fixed to an horizontal rail. This second rail moves along a guide that is fixed in aluminum profiles. At the end of this rail two plates of aluminum are fixed in order to connect the plate to the Scotch Yoke mechanism.

The electric engine in use is the three-phase BMT 631-4 that outputs a power of 0.12 kW with a frequency of 50 Hz. The nominal velocity of the engine is very high compared to the desired one. Besides that, the tank must be excited with a specific frequency corresponding to 7.19 rad/s. Thus, a frequency converter must be used. A frequency converter converts a given frequency into another, allowing it to have the desired motor speed.

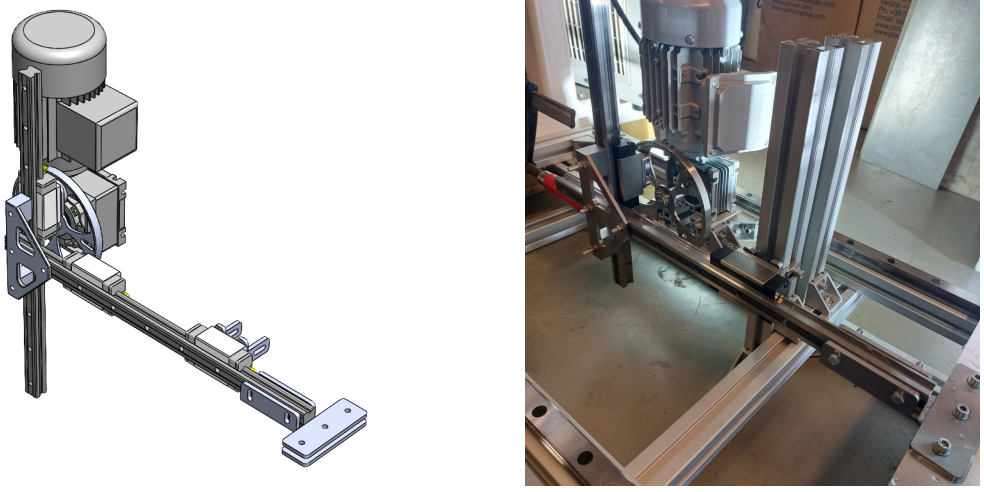

(a) CAD of the mechanism.

(b) Experimental setup.

Figure 6.6: Scotch Yoke arrangement used to convert rotational movement into linear.

6.2.3 Image acquisition

For sloshing experiments is very important to have image acquisition since the visual phenomenons allow to understand better what is happening inside the tank. The system includes a very powerful LED that was directed to the tank and allowed to clearly see the liquid part and the empty one. Then the camera was placed so that in could provide a visualization of the movement in all the amplitude range. The images were saved for a total time of 20 second with an interval of 5 ms.

6.3 Experimental Procedure

The experiments taken into account were only made for a tank filled with 50% of water. This level of water is commonly studied since it presents the liquid height that tends to oscillate at resonant frequencies. Besides that, it presents a critical point where sloshing effects can be potentiated. The most time-consuming part of the experiments refers to the preparation and calibration of all the system. This allows to divide the experimental setup in two parts in which the first one refers to calibration and the second refers to the actual experiments. Liquids are very sensitive to movements which means that any small perturbation applied leads to the movement. In this case, the movement must be subjected only to an horizontal excitation designated by an harmonic function. To ensure that this is the only type of perturbation applied to the tank, the three axis of the acceleramoter were used. The tank was filled with 50% of its capacity with water. After that the three axis of the accelerameter were acquired through LabVIEW. The engine was started and run for about 10 seconds. Observing the behavior of the rig and the behavior of the accelerations it was observed that some lateral accelerations appeared. One of the reasons to that was due to the leveling of the rig. It is a paralleled which means that the all the angles must be perfectly 90°. However, one of the sides was not respecting that requirement. The rig was then leveled which reduced a part of the lateral accelerations. Besides that, the forces inside the tank when in movement also lead to some lateral accelerations. In order to reduce that, the setup was fixed to a rigid structure fixed to the ground.

It is important to mention that not all the variables can be controlled in experiments. One of them is referring to the ambient conditions. Thus, in order to have more accurate results, firstly the reference values were measured. This was done with LabVIEW measuring the pressure values of the air in the empty tank for approximately 10 seconds. After that the mean value obtain for each pressure transducer was obtain and assumed as the referenced value for each position.

Once the calibration is finished, the experiments can be done. This is a phase that is exhaustive since it includes the preparation of each baffles configurations. Following are the description of the steps taken for this phase:

1. Prepare the tank with the liquid level desired. The tank must be marked at the height corresponding to 50% of its capacity and then filled. For the cases with baffles the distances must be measured from the ring that is secured between the acrylic and the upper dome since is the one that is most parallel to the free surface. When baffles are inserted, the level of water must be corrected since the addition of volume increases the liquid height.

2. Once everything is done inside the tank, the upper dome is placed. Six threaded nuts are used to ensure the fixation of the upper dome and provide more safety to the setup.

3. Connect the pressure transducers and the accelerometer to the data acquisition board that was connected to the computer. Connect the pressure transducers, the frequency converter and the engine to the current. LabVIEW is opened.

4. Connect the visual acquisition data. The image acquisition system must be connected to the current and the acquisition parameters must be defined so that the images are saved for intervals of 5 ms in a total time of 20 seconds.

5. Everything is ready to run the case. LabVIEW starts the acquisition data as well as the image acquisition system. The engine rotates for 7 cycles and then stops. After 4 seconds of stopping the movement, acquisition in LabVIEW stops and text file is saved accordingly to the case.

6. To run the following test, the fluid must be completely stopped. Data must be obtained for each case at least for five runs.

7. Once all data is acquired the cycle gets to the beginning.

Chapter 7

Results And Discussion

This chapter presents and discusses the results obtained through the numerical and experimental models. This chapter is divided into three sections. The first one presents the conclusions of the numerical model, including the H-convergence. The second section refers to experimental results, and the third compares both. Each section is divided into no, four, and five baffles for better data comprehension. The results will be given as wave elevation as a function of time, i.e., the 0 m elevation refers to the free-surface.

Moreover, to give a more clear information, the results for each location of pressure transducers will be indicated as:

- P1 referring to the pressure transducer located near the wall;
- P2 referring to the pressure transducer between the upper and the lower ones;
- P3 refers to the lowest pressure transducer located in the axis.

Lastly, the different configurations will be addressed as explained in Table 7.1 for a more unmistakable comprehension.

Table 7.1: Nomenclature of studied Cases.

Configuration	Case
No baffles	Case I
4 baffles equally spaced	Case II
4 baffles differently spaced	Case III
5 baffles equally spaced	Case IV
5 baffles differently spaced	Case V
5 baffles with $w = 60$ mm	Case VI
4 baffles with $w = 60$ mm	Case VII

7.1 Numerical Model Results

7.1.1 H-Convergence

CFD studies strongly depend on the discretization of the space, i.e., on the grid used. However, sometimes, the grid could be more refined and computationally expensive. Thus, a mesh convergence study is done to understand the best compromise between solution and

computational cost. This method consists of increasing the element size to understand the impact in the final solution under the same conditions.

To understand what is the best mesh for the case study, the tank was subjected to an excitation following Equation 5.3. The simplest way to input this excitation in ANSYS Fluent® is through a UDF that defines the system's acceleration. Thus, the simulations were carried out for an amplitude A_f = 55 mm and ω = 7.19 rad/s. The fluid used for the simulations was water. The properties are described in Table 7.2. The solution was obtained for 2 seconds of simulation with a variable time step based on the Courant number.

Table 7.2: Fluid properties for water.

Fluid	ρ, kg/m^3	μ, kg/ms
H_2O, liquid	998.2	0.001003

The element size started at 16 mm, decreasing following the relation mentioned in Equation 5.1. Table 7.3 shows the mesh properties, precisely the element size and the total number of elements of the mesh. Figure 7.1 shows the upper view of the mesh for the different sizes used. These meshes used the option of adaptative sizing. To better understand the behavior of the pressure curves, the amplitude was plotted as a ratio with the amplitude of the curve for the most refined mesh in the function of the inverse of the element size.

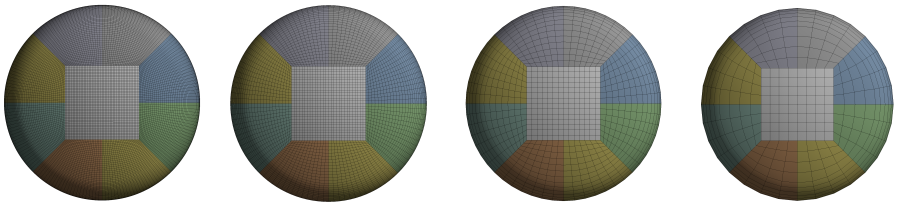

(a) H = 2.5 mm (b) H = 4 mm (c) H = 8 mm (d) H = 16 mm

Figure 7.1: Meshes used for the H-convergence study.

Table 7.3: Mesh properties for the H-convergence study.

Mesh	**Element size**, mm	**Number of elements**
1	16	5440
2	8	31192
4	4	81120
5	2.5	987896

Figure 7.2 shows that as the element size decreases, the amplitude increases. For an element size of 16 mm, it is possible to understand that the difference from the other grid dimensions is very significant. However, when H increases from 8 to 4, it is not that noticeable, and it is also possible to observe in the slope of the trend line decreased.

Figure 7.3 presents an amplitude relation as a function of the inverse of the grid element size. This amplitude ratio is given by Equation 7.1 such that the maximum amplitude for each element size case is related to the amplitude for the case where the elements have a

size of 2.5 mm.

$$\mathbf{A^*} = \frac{A}{A_{H=2.5mm}} \quad (7.1)$$

Understandably, the curve has a logarithmic behavior. The amplitude ratio increases as the inverse of the element size increases, which means that as the element size decreases, the amplitude also decreases. However, at some point, the slope of the curve decreases. At a given point, the slope of the curve starts to become constant, which occurs because the difference between the amplitudes ratio is meager.

Even though the mesh with an element size of 2.5 mm shows good results, the simulation cost is very high. Thus, the option of adaptative meshing was selected. Adaptative meshing allows the refinement and coarsen of the mesh in specific locations, which can be specified from different criteria. In this case, the free surface is the most crucial location, and its behavior is the most relevant for this study.

Adaptative meshing was used to understand the effect on the computational cost and the solution. Thus, the geometry was discretized through a grid with elements of 6 mm. The adaptative meshing criteria are based on the multiphase, meaning the interface was automatically recognized by determining the fluids domains. The coarse criteria were applied to all the domains except for the interface, where the minimum size of the elements was settled as 2.5 mm. The solution provided with this grid is very close to the solution of the grid, with a size of 2.5 mm. Even though the minimum value of the coarser mesh is different, most of the solution is very similar. Furthermore, using this mesh reduces the computational cost significantly. Thus, the mesh of elements with 6 mm refined in the interface is the best option for this problem.

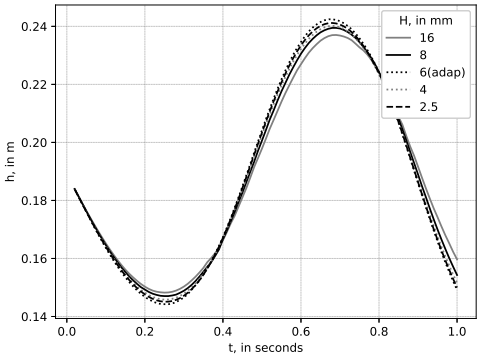

Figure 7.2: Pressure as a function of time for different element sizes, and the amplitude ratio as a function of element size inverse.

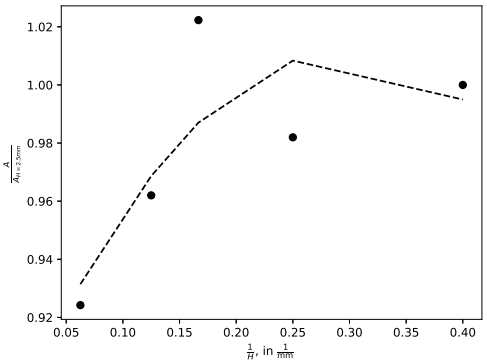

Figure 7.3: Maximum pressure in function of the inverse of the element size.

7.1.2 Configurations analysis

As explained in Chapter 2, damping is a critical factor when evaluating the behavior of the liquid. The evaluation of liquid damping is made through different methodologies. One of them is to determine the logarithmic decrement of a variable once the tank excitation stops. However, the liquid must be in a steady-state behavior before the excitation can be stoped. In order to define the correct excitation equation, a first case was simulated in ANSYS® to understand at which instant the liquid would be in a steady-state condition or very close to it.

7.1.2.1 With No Baffles

In Chapter 2, different methods to evaluate damping were exposed. The easiest way to evaluate the behavior of the liquid is through the logarithmic decrement of a given variable. In order to use this method, the fluid must be in a steady state, which means that the wave has the same behavior from that instant until another perturbation is applied. With that in mind, the unbaffled tank is simulated in ANSYS Fluent® subjected to the harmonic acceleration function. Figure 7.4 shows the variation of the liquid height near the wall as a function of time. In the first two seconds, the liquid height varies very rapidly, and the two cycles that occurred in this time interval have a difference of amplitude in the order of 0.00003 mm. Hence, for the rest of the time, the height of the liquid is almost constant, being more noticeable that the water is steady after the 6 seconds.

Considering this, the damping will be evaluated by applying the excitation function to the tank for 6 seconds, and then it will be stopped, leading to the damping of the fluid.

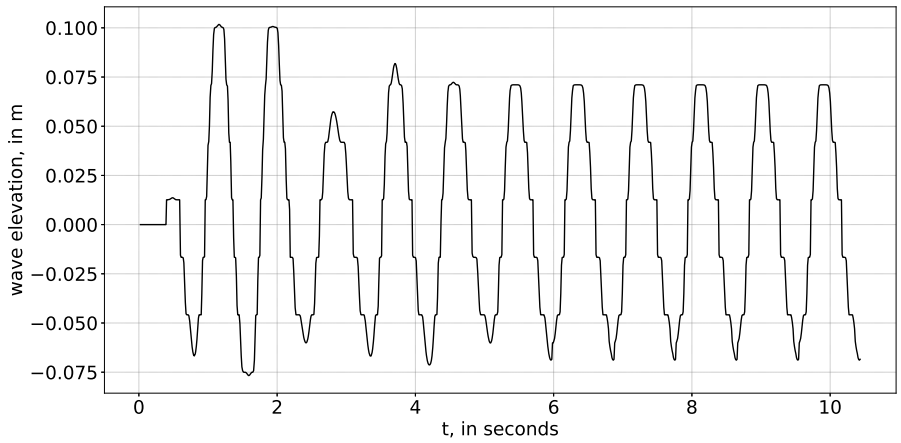

Figure 7.4: Wave elevation as a function of time for Case I.

One of the objectives is to validate the numerical model through the experimental one. Therefore, the higher the number of similar variables in both cases, the higher the simi-

larity. In the experimental model, the frequency of excitation is reached trough the help of a frequency converter, which means that the desired frequency is not instantly reached. This frequency will increase from 0 to the desired one in a small time interval in a linear way, i.e.,

$$\omega(t) = \frac{\omega_0 t}{\Delta t_{accel}} \quad (7.2)$$

where ω_0 is the frequency of excitation and Δt_{accel} is the time interval of acceleration necessary to reach the frequency. This increase in the frequency is fast. Thus, it was only considered for 0.5 seconds. After 0.5 seconds, the excitation is given by Equation 5.3 for 5.5 seconds, stopping at 6 seconds. This compiles into a UDF given by:

$$\begin{cases} a = A_f(\frac{\omega_0 t}{\Delta t_{accel}})^2 \sin(\frac{\omega_0 t^2}{\Delta t_{accel}}) & \text{if } 0 < t < 0.5 \text{ [s]} \\ a = A_f \omega_0^2 \sin(\omega_0 t) & \text{if } t \geq 0.5 \text{ [s]} \\ a = 0 & \text{if } t < 6 \text{ [s]} \end{cases} \quad (7.3)$$

Figure 7.5 shows the variation of the liquid height as a function of time at a particular location. The point in question is located at the dome at a height of 28.39 mm from the peak curvature of the dome corresponding to position P1, the position near the wall. The wave elevation is an integral function of the fluid volume in a line. Thus, it has some noise. All the data is passed through a low-pass filter to reduce this noise. It is possible to understand that the amplitude variation of the liquid is approximately 87 mm, corresponding to 1.59×A.

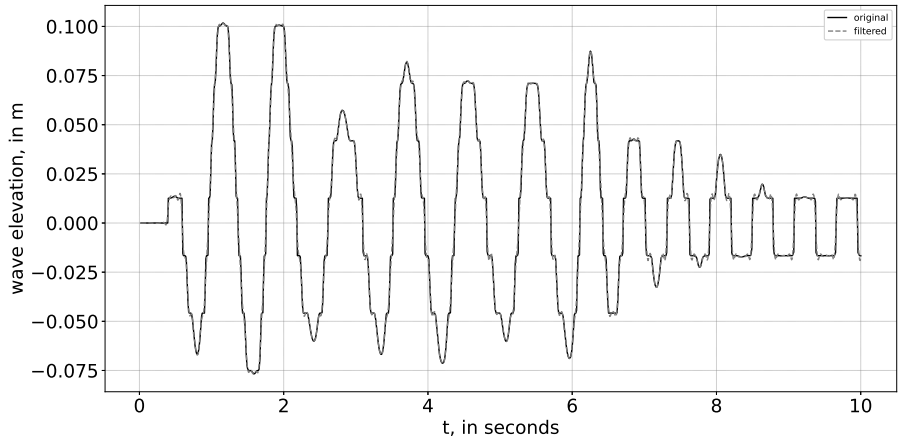

Figure 7.5: Wave elevation as a function of time for Case I.

Once the excitation is stopped, the liquid height reduces considerably, so the amplitude

reduces from 0.08 m to 0.048 m after a cycle. When the simulation is stopped after 10 seconds, the liquid still has sufficient energy to complete a few more cycles until the liquid has completely ceased. In this case, the only factor that reduces the oscillation of the fluid is its viscosity. Thus, the amplitude reduction is minimal from cycle to cycle. From theoretical calculations, the damping ratio for a no baffle case equals 0.0023. Through the logarithmic decrement of the data in Figure 7.5, the damping ratio equals 0.00937. The theoretical damping does not consider the influence of domes, and it assumes that the stabilization of the liquid is only due to the viscosity.

Figure 7.6a shows the behavior of the liquid for an instant of 4 seconds. Evaluating the free surface, it is possible to see that the liquid starts to create small waves, which raises the hypothesis of other modes or it can be also due numerical effects. Furthermore, the free surface line is not entirely linear, meaning these conditions are not under the linear theory. Figure 7.6b shows the behavior of the liquid at 6.5 seconds of simulation, which means that the excitation has been stopped at this time. It is clear that even after the movement has been concluded, the fluid shows a clear wave with energy to continue the propagation of the wave for a couple more seconds.

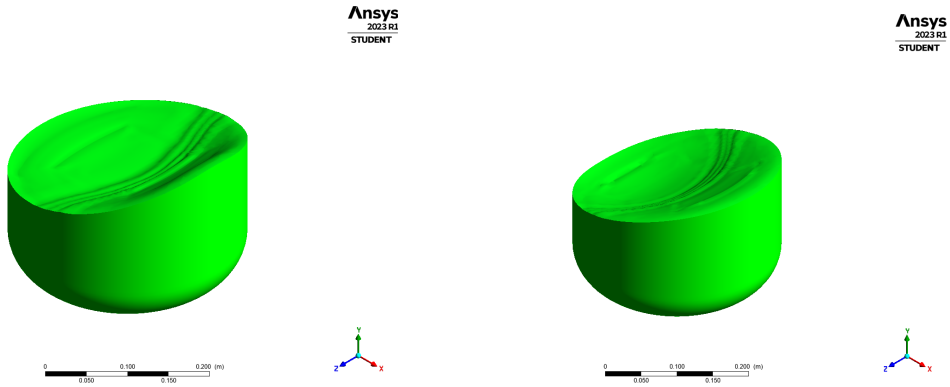

(a) t = 4 seconds (b) t = 6.5 seconds

Figure 7.6: Representation of the fluid in different time steps.

7.1.2.2 With Four Baffles

Figure 7.7 and Figure 7.8 show the wave elevation as a function of time for four baffles equally spaced and differently spaced, respectively. The curves obtained in ANSYS® show more noise than for the case with no baffles. This may occur due to the higher turbulence and the more chaotic behavior of the free surface.

Case I has a maximum elevation of around 0.061 m, and Cases II and III show a maximum elevation of around 0.64m. Hence, including baffles decreases the movement of the free surface, which also decreases its elevation. Evaluating the wave amplitude, for Case II, it corresponds to approximately 0.043 m; for Case III, it is around 0.051 m. When equally spaced baffles, the free surface is right above the third baffle and close to the fourth. Case

II configuration occupies a percentage of the tank height of 84%, while Case III occupies only 67%. This may be one of the reasons why Figure 7.7 shows less movement than Figure 7.8 under excitation.

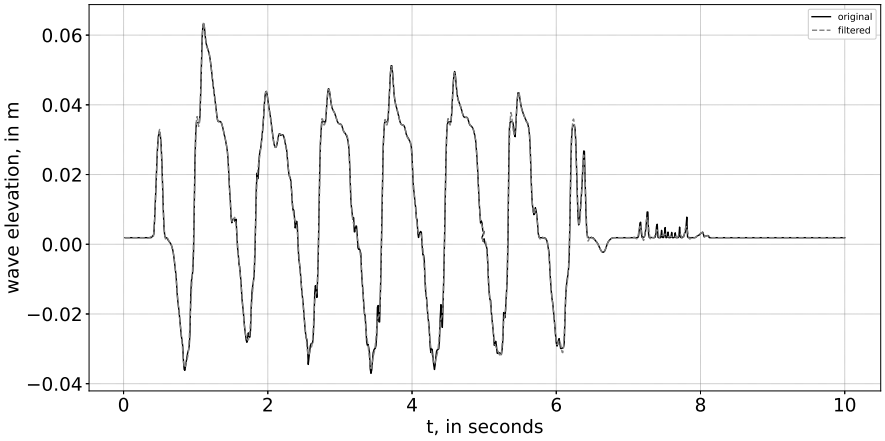

Figure 7.7: Wave elevation as a function of time for Case II.

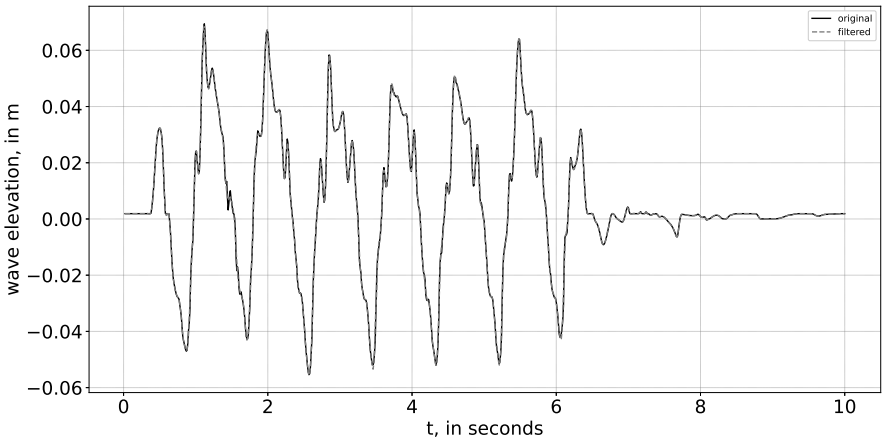

Figure 7.8: Wave elevation as a function of time for Case III.

Representation of liquid movement is seen in Figures 7.9a and 7.9b for Cases III and II, respectively. Here, it is possible to observe that at the same instant, Case III is reaching the maximum amplitude of the wave, while Case II is already decreasing. This can occur due to the near presence of the following ring. Moreover, it can be seen that the fluid has more than one wave, which means that this condition causes the appearance of other normal modes.

As soon as the excitation is stopped, the free surface decreases from a maximum wave elevation of 0.03 m to 0.005 m in one cycle. Furthermore, it is evident that once the excitation is ceased, the movement of the free surface stops entirely in the 10 seconds of simulation, in such a way that it looks that after 2 seconds, the fluid completely stops. This

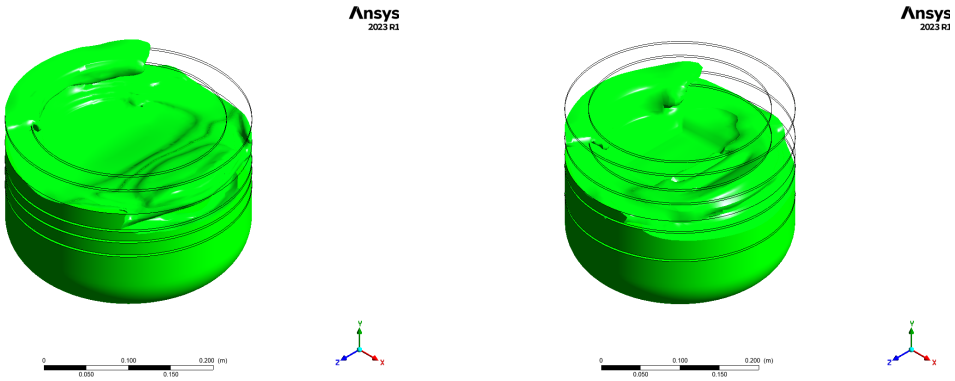

(a) Case III (b) Case II

Figure 7.9: Representation of the liquid at $t = 4$ s.

occurs for Case II, but Case III has some movement after 2 seconds. Nevertheless, these cases validate the efficiency of ring baffles in reducing liquid movement.

The representation of the liquid for both cases mentioned in this Subsection is seen in Figures 7.10a and 7.10b after 6.5 seconds of simulations. Thus, this represents the fluid after stopping the movement. The behavior of the free surface is almost the same for both cases. Additionally, here it is seen that the fluid does not have much energy, meaning that baffles already damped the movement. Case II seems to have a less chaotic movement of the free surface when compared to Case III.

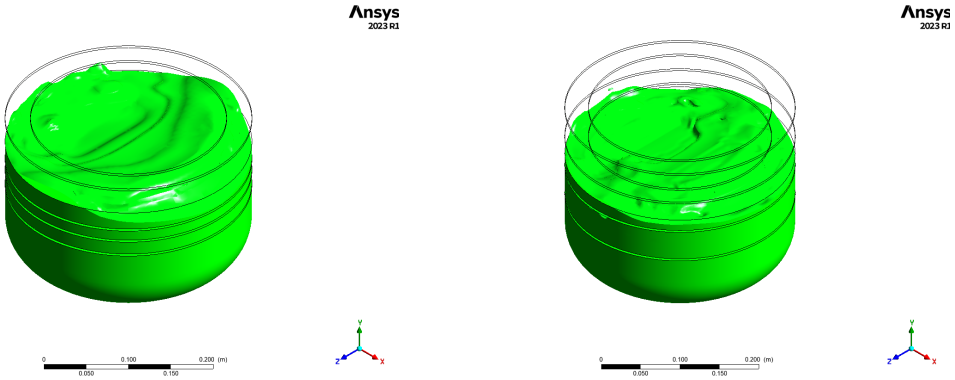

(a) Case III (b) Case II

Figure 7.10: Representation of the liquid at $t = 6.5$ s.

Equation 2.27 is used to evaluate the damping of both configurations. For Case II, the damping ratio equals 0.0194, and for Case III is equal to 0.0204. The damping ratio of both configurations is not very different. However, as predicted in the analytical theory, the damping ratio of differently spaced baffles is higher than when an equal distance is used.

7.1.2.3 With Five Baffles

The elevation of the wave at the P1 location is represented in Figures 7.11 and 7.12 for Cases IV and V, respectively. This data shows curves with less noise than in the Subsection above. Thus, implementing other baffles may provide more stabilization of the liquid. Evaluating the maximum elevation, it is seen that for Case IV, it is equal to 0.038 m, and for Case V, it is 0.06 m. When compared to the unbaffled case, the difference is perceptible.

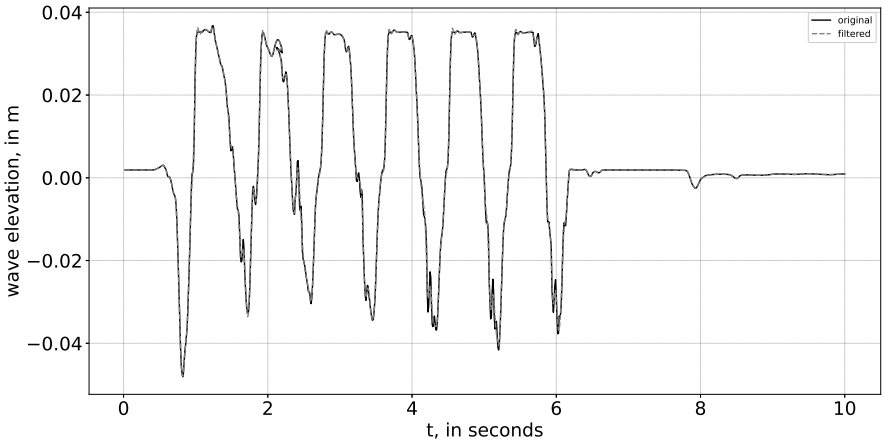

Figure 7.11: Wave elevation as a function of time for Case IV.

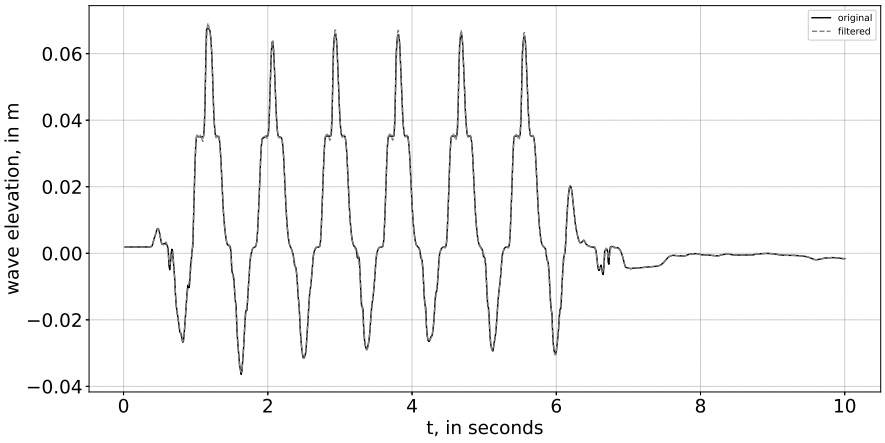

Figure 7.12: Wave elevation as a function of time for Case V.

Figure 7.11 shows an amplitude of around 0.031 m, while Figure 7.12 gives an amplitude of approximately 0.043 m. As in the four baffle configurations, the free surface is closer to the next baffle when the distances are equal, which can answer why the amplitude, in this case, is less than for the case with different spacing.

The ANSYS ® representation of the water is shown in Figures 7.13a and 7.13b after 4 sec-

onds of simulation for Cases V and IV, respectively. At the same instant, Case V seems to be reaching the highest wave elevation while Case IV is already decreasing the elevation. These figures also show a more chaotic flow behavior with various waves forming. However, this anti-sloshing system still reduces the movement of the liquid.

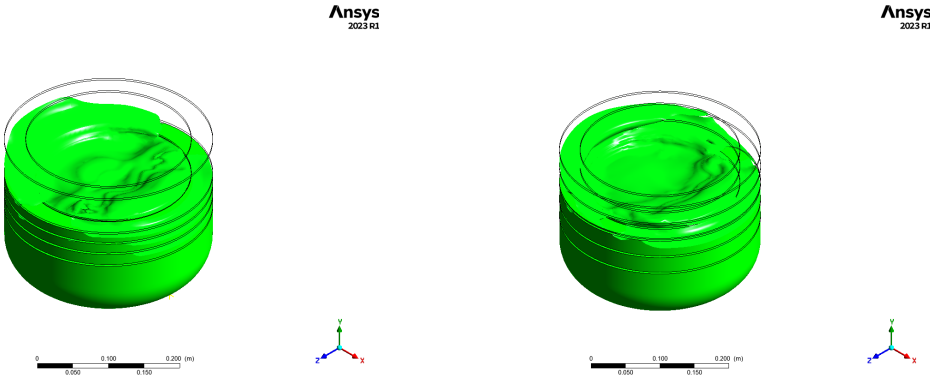

(a) Case V (b) Case IV

Figure 7.13: Representation of the liquid at $t = 4$ s.

Excitation is stopped at 6 seconds, and a rapid decrease in the amplitude is noticed. Case IV shows a rapid amplitude decrease, while Case V still needs 1 second to stop completely. Through logarithmic decrement of both cases, Case IV presents a damping ratio of 0.016 and Case V of 0.0048. These results must be more accurate since the curves for this case present irregular behavior when the liquid stops. A visual reference of liquid movement is seen in Figures 7.14a and 7.14b for both five baffles cases 0.5 seconds after the excitation is stopped. Both movements of the liquid seem very similar. However, Case IV has fewer waves and a more even distribution of the free surface. Moreover, it is seen that only after 0.5 seconds after stopping the excitation, the liquid looks already more stabilized.

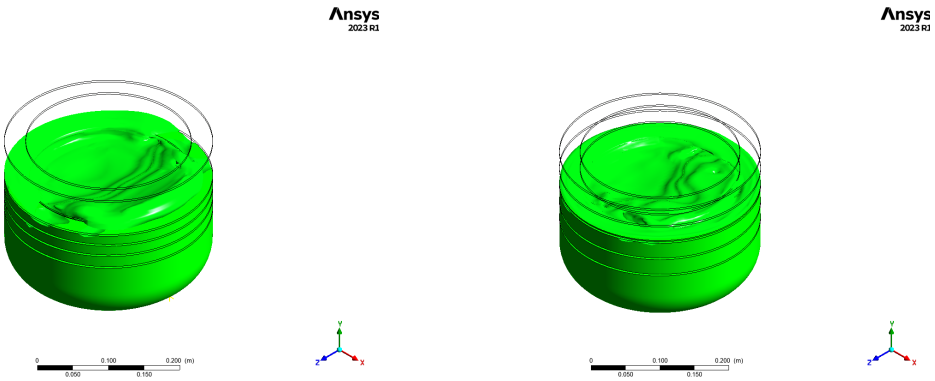

(a) Case V (b) Case IV

Figure 7.14: Representation of the liquid at $t = 6.5$ s.

7.1.2.4 All Cases

One of the main objectives is to understand the best configuration for the problem in question. This Subsection is dedicated to comparing all the results for the numerical analysis. In Figure 7.15 are the results of wave elevation for all the cases studied and before discussed. The elevation of the unbaffled cases is higher than the other cases. However, under excitation, the difference between the configurations with fours and five baffles is minimal. It is necessary to note that the data has more noise when baffles are intersected. This may be because turbulence effects become more accentuated in cases with baffles.

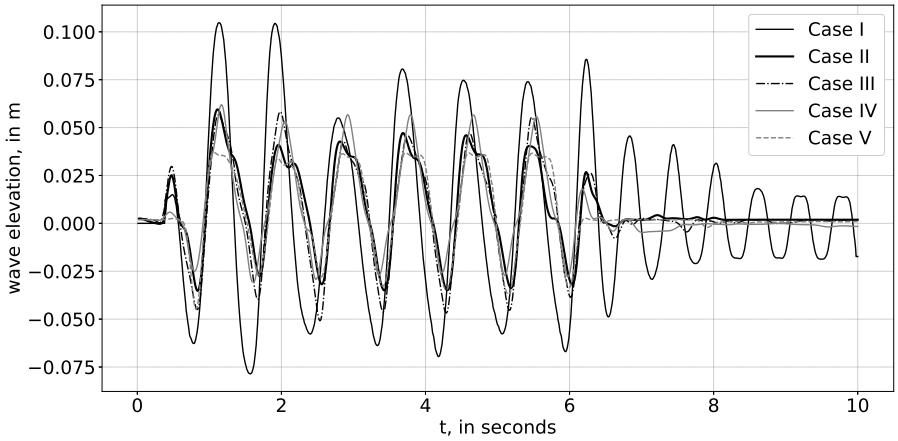

Figure 7.15: Wave elevation as a function of time for all cases.

One of the most critical parameters is damping, which is evaluated after stopping the movement. The difference between Case I and the others is enormous. When the movement is stopped, the liquid has enough energy to continue the propagation of the wave for more cycles until it is completely stopped. On the contrary, the other four cases show that the fluid stabilizes almost immediately after ceasing the excitation. This comparison validates the efficiency of this anti-sloshing system, at least for the conditions and this case of study. Comparing the cases with four and five baffles, little difference is seen in damping the liquid. Thus, adding one more baffle may not be beneficial regarding weight.

Table 7.4: Damping ratio from the numerical data.

	γ
Case I	0.0093
Case II	0.0194
Case III	0.0204
Case IV	0.016
Case V	0.0048

Table 7.4 organizes the damping ratio γ values obtained through the numerical simulations. The damping ratio for Case I is meager since, in this case, the only thing that helps to damp the liquid is viscosity. Case II has a damping ratio of 2 times greater than the

first one, and Case III is 2.2 times more damped than an unbaffled tank. However, both five-baffle configurations have a lower damping ratio when compared to cases with four baffles.

7.2 Experimental Model Results

7.2.1 No baffles

When evaluating the experimental results, some aspects need to be considered. One is related to the region where the pressure is being measured. Figure 7.16 shows the wave elevation of tests with no baffles. The P1 location refers to the upper sensor, P2 refers to the middle sensor, and P3 refers to the sensor in the axis of the tank.

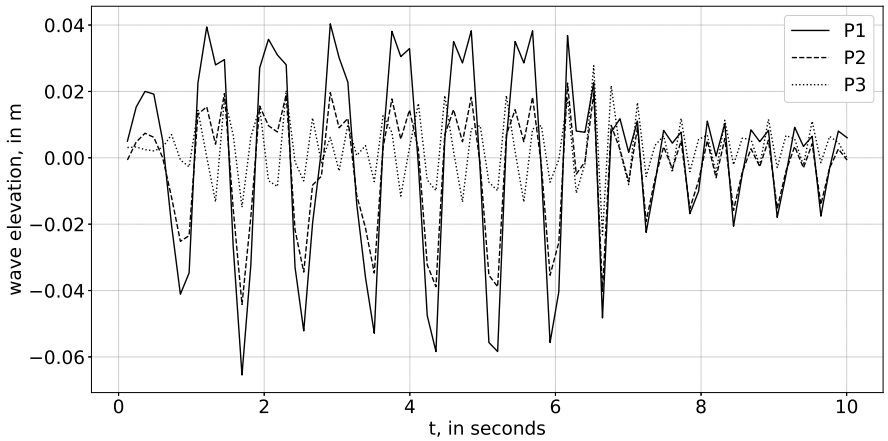

Figure 7.16: Wave elevation as a function of time for the three positions of the pressure transducers in the Case I.

The pressure transducer at the P1 location shows the most considerable amplitude variation. It shows that wave elevation goes from a minimum value of -0.064 m to a maximum value of 0.04 m, which corresponds to a mean amplitude of 0.052 m. Doing the same reference to the other two locations, the mean amplitude at the middle sensor is 0.021 m and for P3 location is 0.015 m. This means that the amplitude decreases as the sensor position gets deeper. It is indeed expected that the higher amplitude occurs near the wall, which corresponds to the P1 position.

An important parameter is the signal frequency since it will allow to see if the wave only oscillates in the first mode. This evaluation is commonly made using Fourier analysis. A Fourier Transform analysis is a mathematical technique to decompose a complex waveform or function into a sum of more straightforward sinusoidal functions, each with a specific frequency, phase, and amplitude. Thus, the Fourier Transform analysis was made for the three functions of the experimental results. Figure 7.17 shows the relative magnitude

as a function of the wave elevation data frequency obtained through the unbaffled Case experiments. Relative magnitude refers to how the amplitudes of different frequency components compare within the transformed signal, helping to understand which frequencies are dominant or significant in the original signal. Referring to P1 and P2 locations, it is seen that the higher peak occurs between 1 and 1.5, more precisely at 1.16 Hz, corresponding to the frequency of the excitation. However, it is seen that some other peaks appear at different frequencies. However, at location P3, the peaks occur almost simultaneously. This can lead to the assumption that some other modes appear for these excitation conditions, i.e., the sloshing mode is not linear.

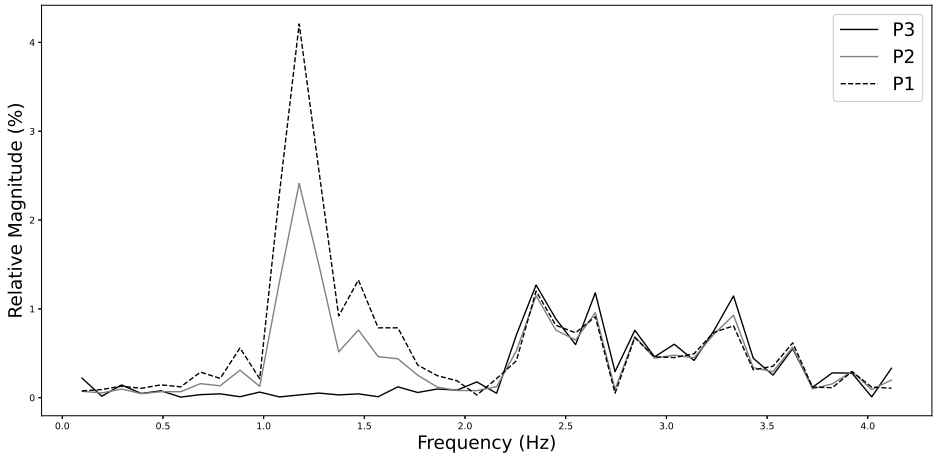

Figure 7.17: Fourier transform analysis of the experimental data for the Case with no baffles.

Figure 7.18a shows the images acquired for the experiments with no baffles four seconds after the excitation is applied. It is perceptible the chaotic behavior of the liquid. Besides that, during the experiments, it was observed that the liquid was in a swirl motion. This means that the conditions do not allow a linear behavior of the liquid. The theory does not correctly predict the behavior of the tank with domes, which influence since the conditions lead to a wave height that reaches the upper dome. Here, the fluid rolls and helps create a chaotic behavior.

The excitation is stopped, and it is perceptible that the wave's amplitude decreases. However, after stopping, the waves have a slight decrease in amplitude. This means that the fluid has sufficient energy to continue the movement for more seconds until it is stopped completely. In this case, only the viscosity will dampen the movement. Doing the logarithmic decrement of the wave, the damping ratio is equal to 0.00338. Figure 7.18b shows the liquid 0.5 seconds after the excitation is stopped. Here, it is still perceptible that the wave has a significant height, almost the same as in Figure 7.18a.

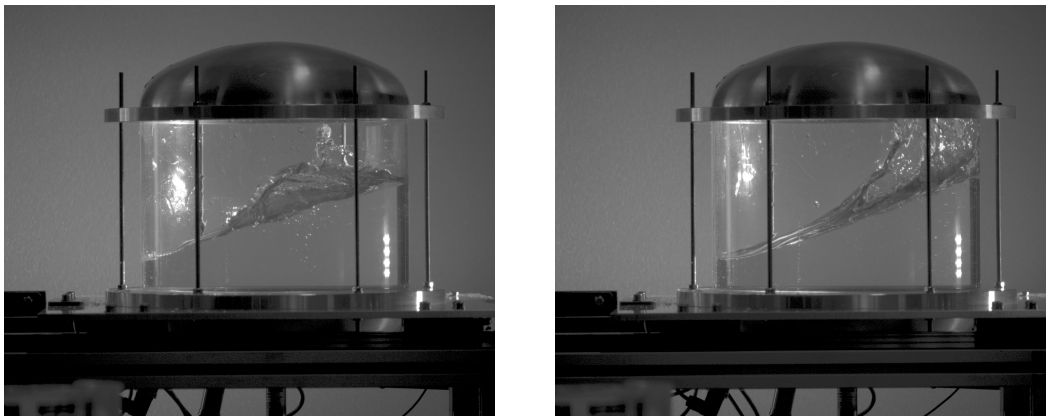

(a) $t = 4$ seconds. (b) $t = 6$ seconds.

Figure 7.18: Images of the experiments with no baffles.

7.2.2 With Four Baffles

Experimental data acquired for the four baffles equally spaced configuration is represented in Figure 7.19. As in the unbaffled case, it is possible to observe the big difference between the wave amplitude in the three locations. The behavior of these curves seems to be more smooth than in Figure 7.16. This may occur due to the implementation of baffles that lead to a more stabilized free surface movement. Accounting for the amplitudes of the curves, at the P1 location, the amplitude equals 0.039 m. At P2, it is equal to 0.022 m, and at P3, it is equal to 0.005 m. Comparing the case with no baffles, it is seen that the implementation of these rings leads to a decrease of the amplitude greater than 1.3 for the first two locations. At P3, the wave's amplitude in the unbaffled case is almost 2.5 times greater than the four ring baffles equally spaced. This means that the height of the waves in the axis location decreased, leading to the conclusion that the implementation of baffles also decreased the chaotic motion of the liquid.

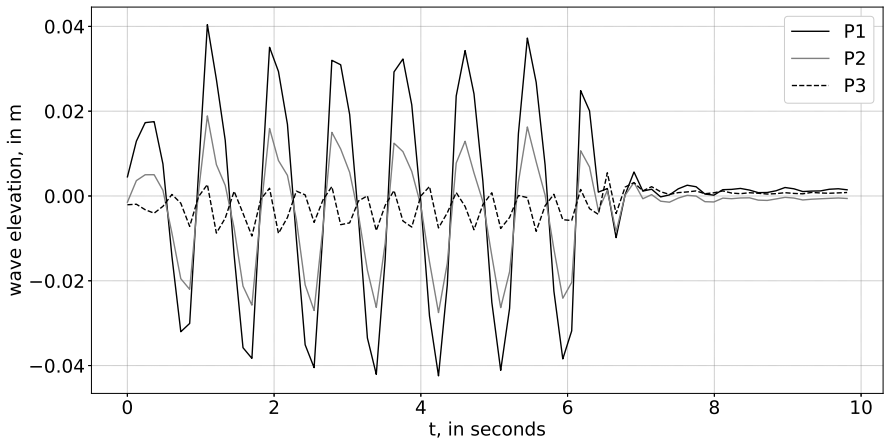

Figure 7.19: Wave elevation as a function of time for the three pressure transducers location for Case II.

Figure 7.20 represents the experimental data for the four baffles case with different spacing. The behavior of the waves is almost the same as the one mentioned before. In this case, the behavior of the curve looks cleaner, especially once the excitation is stopped. Evaluating the amplitudes of the functions, at P1, it has a value of 0.042 m; at P2, it is equal to 0.023 m; and at P3, it corresponds to 0.0047 m. Contrary to what was expected in the analytical method, this configuration has higher variations of wave elevation than the case where the baffles are equally spaced. The free surface is located right above the third baffle in the first case, with the fourth very close to it, contrary to the second case, where the fourth baffle is more distant. This leads to less damping.

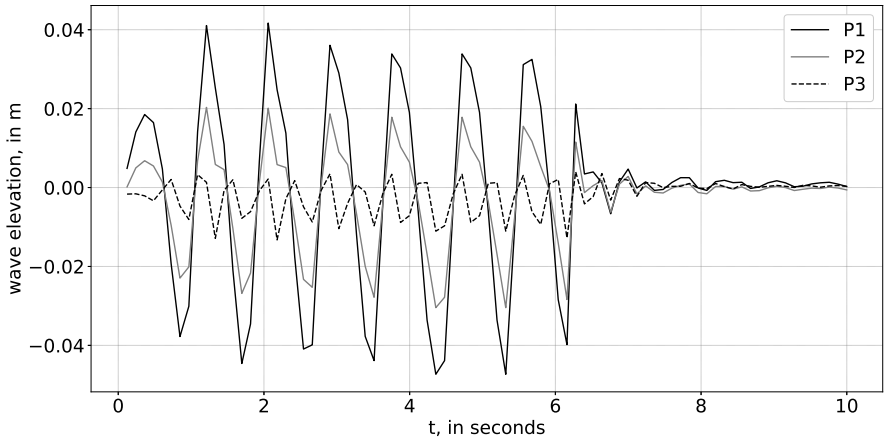

Figure 7.20: Wave elevation as a function of time for the three pressure transducers location for Case III.

A visualization of the liquid at 4 seconds of oscillation is seen in Figures 7.21a and 7.21b for Cases III and II, respectively. Through this image acquisition, it is possible to see that the free surface has a higher amplitude in the different spacing configurations simultaneously, which can occur due to the lower height range of the baffle's position. However, Case III seems to have a less chaotic behavior. In these Figures, it is possible to see the swirl of the free surface fluid and some tiny drops of water that separate from the free surface and move in the empty zone of the tank. Furthermore, observing some places where the liquid is allocated is possible.

The excitation is ceased, which leads to the stabilization of the fluid. An immediate reduction is observed in curves. Figure 7.20 seems to have a smaller amplitude right after stopping excitation than Figure 7.19. After that, Case II seems to reduce the amplitude of the wave faster than Case III. However, obtaining the damping ratio for both cases is the best way to make conclusions. Logarithmic decrement allows a damping ratio of 0.01899 for Case II and 0.021 for Case III. Thus, Case III has a better performance in damping the fluid.

The images of the liquid right after the excitation is stopped are in Figures 7.22a and 7.22b. Case III has a less chaotic behavior than Case III. Thus, it shows a more stabilized fluid.

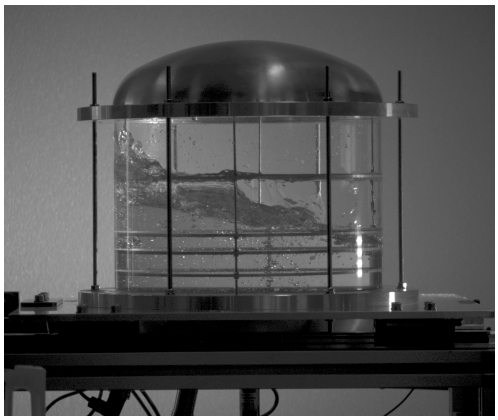

(a) Case III

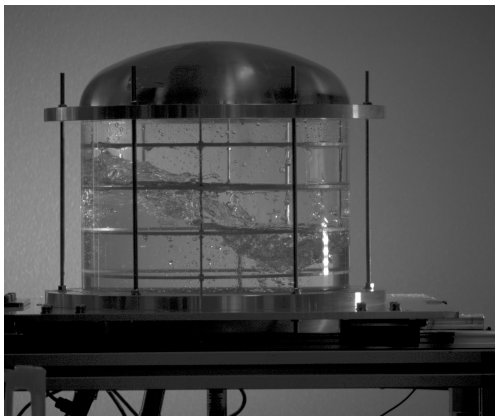

(b) Case II

Figure 7.21: Image acquisition of fours baffles configurations at $t = 4$ seconds.

Case II shows that the wave still has the energy to go above the third baffle. It is also essential to notice the tension between the free surface and the baffles, which looks like the fluid is glued to the baffle.

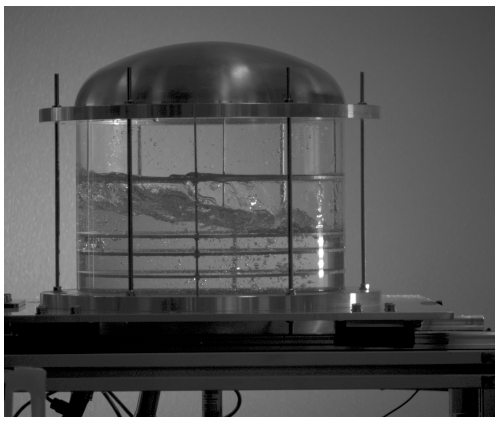

(a) Case III

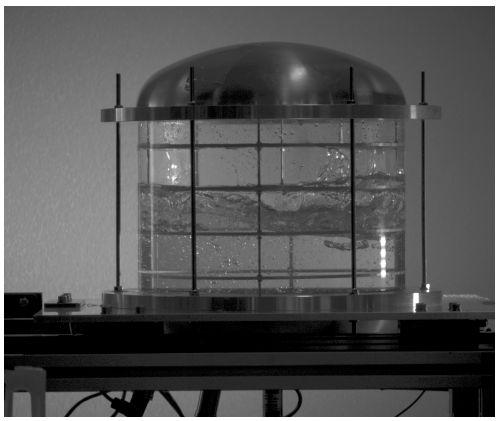

(b) Case II

Figure 7.22: Image acquisition of fours baffles configurations at $t = 6.5$ seconds.

Figures 7.23a and 7.23b explicit the Fourier transform analysis for the configurations of four baffles differently spaced and equally spaced, respectively. The highest frequency peak occurs at 1.16 Hz, having a higher relative magnitude than in the unbaffled case (Figure 7.17). Furthermore, it is seen that the magnitude of other frequencies decreased when compared to the case with no baffles. This takes to the assumption that the implementation of baffles reduces the chaotic behavior of the liquid and also the appearance of other normal modes.

7.2.3 With Five Baffles

Figure 7.24 shows the results obtained for wave elevation when five ring baffles equally spaced were tested. These curves show a harmonic behavior in the three locations. As ex-

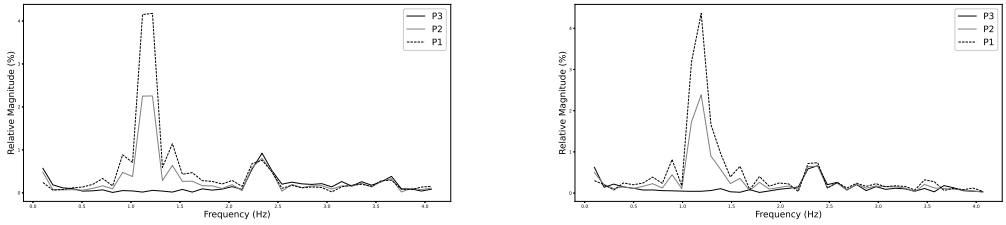

(a) Different spacing (b) Equal spacing

Figure 7.23: Fourier transform analysis of the experiment data for the case with four baffles.

pected, at the P2 location, the initial wave elevation is higher since it is the deeper pressure transducer. It is seen that the variation of the upper sensor is the highest. The maximum value of wave elevation is very close for P2 and P1 locations. This is to assume that as the position gets closer to the center, the wave's amplitude reduces. Looking closer at the curves, it is possible to calculate the amplitudes obtained at locations P1, P2, and P3, amplitudes of 0.039 m, 0.022 m, and 0.0046 m, respectively. Once more, it is seen that compared to the case with no baffles, the amplitudes reduce significantly. However, compared to the cases with four baffles, the differences are insignificant. This can mean that adding more baffles is not beneficial when the liquid is under excitation.

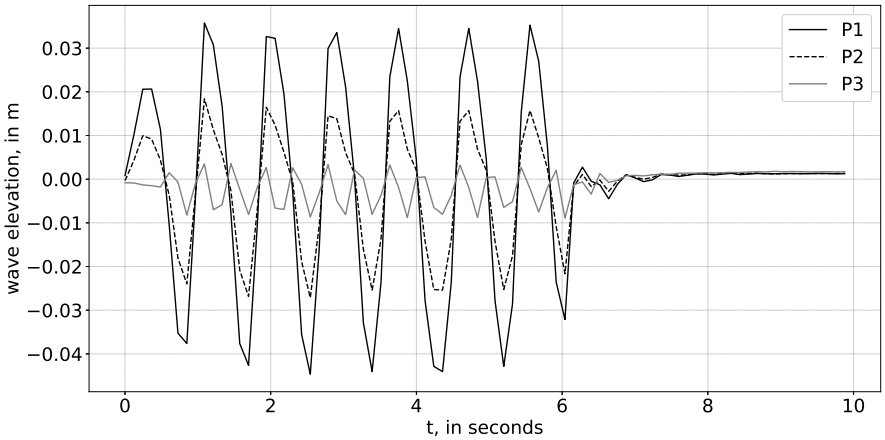

Figure 7.24: Wave elevation as a function of time for the experiments with five baffles and equal distancing.

On the other side, Figure 7.25 represents the behavior of wave elevation inside a configuration of five baffles differently distanced is used. This shows wave elevation as a function of time in different locations. In this case, the same behavior as the above curve is observed, appearing again at location P3, a variation of wave elevation that may occur due to the appearance of a chaotic mode. Accounting for the amplitudes of the curves, respectively, at locations P1, P2, and P3, they correspond to values of 0.041 m, 0.024 m, and 0.0073 m.

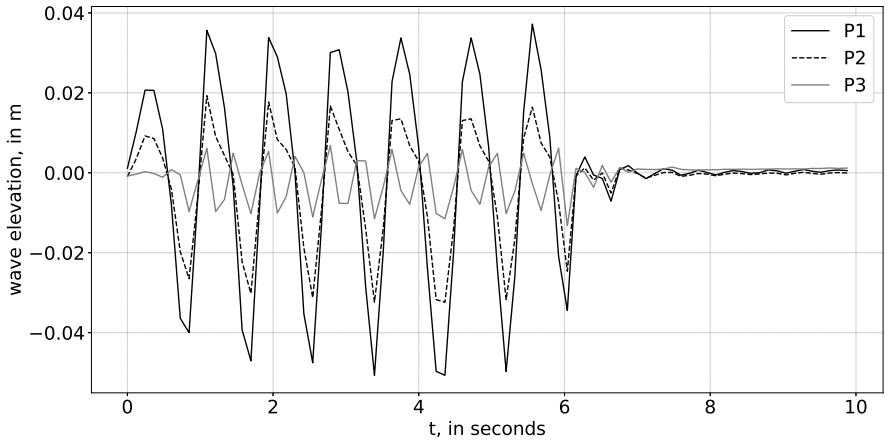

Figure 7.25: Wave elevation as a function of time for the experiments with five baffles and different distancing.

Visualization of this phenomenon is an excellent way to conclude. Thus, the visualization of water's behavior for both cases discussed in this Subsection is presented in Figures 7.14a and 7.14b. These images were acquired after 4 seconds of the experiment. The fluid is more stabilized with this configuration than with four baffles configurations. Moreover, the fluid seems less turbulent. Case IV presents a separation of the free surface in the higher elevation due to the baffles' close position. The amplitude of the waves looks very similar.

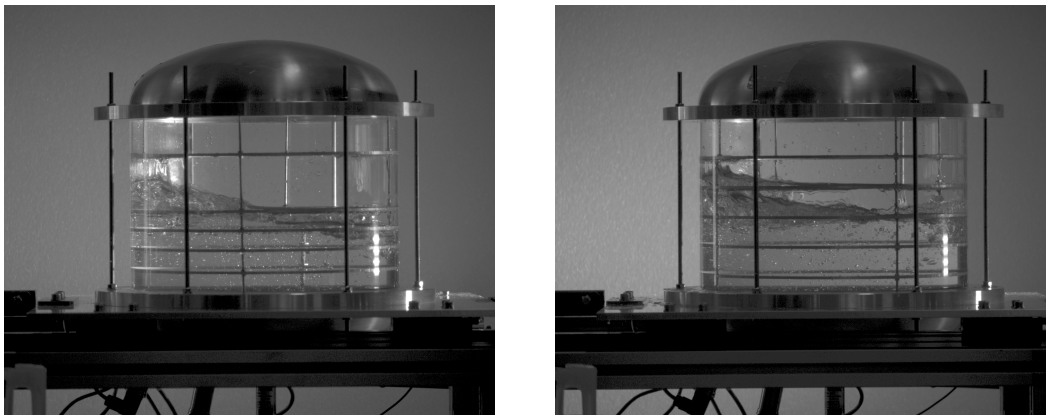

(a) Case IV (b) Case V

Figure 7.26: Image acquisition of five baffles configurations at $t = 4$ seconds.

The excitation is stopped after 6 seconds, and it is possible to see that the amplitude reduction in only one cycle reduces drastically. Besides that, it is possible to observe that the movement of the liquid stops in only one second, leading to no elevation of the liquid. Through Figures 7.14a and 7.14b, it is possible to understand the performance of the liquid right after ceasing the excitation. The first one shows a more stabilized behavior of the free surface, while the other looks to have sufficient energy to complete at least one more

cycle until the liquid is completely stabilized. Case IV shows a damping ratio of 0.0019.

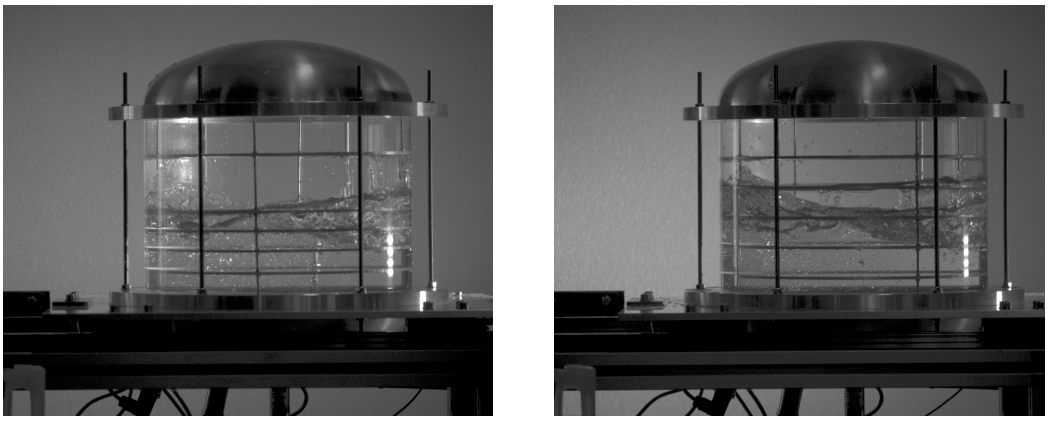

(a) Case V (b) Case IV

Figure 7.27: Image acquisition of five baffles configurations at $t = 6.5$ seconds.

Fourier transforms represented in Figures 7.28b and 7.28a, for Cases IV and V, respectively, allow for evaluation of data's frequencies. These cases show, essentially, four different frequencies with more significant magnitudes. Comparing Figures 7.23b and 7.23a, it shows a slight difference. However, compared to Figure 7.17, it shows a decrease in the magnitude of different peaks, which, once more, corroborates the efficiency of baffles.

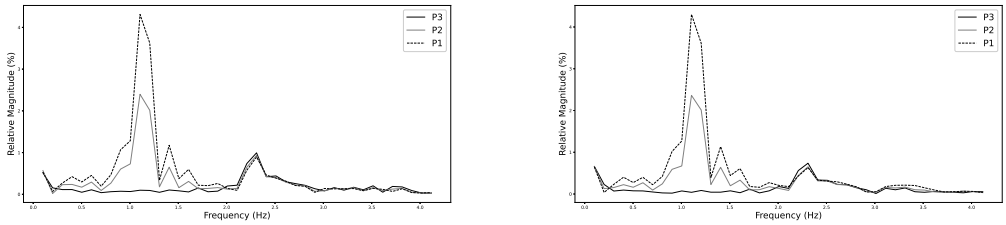

(a) Different spacing (b) Equal spacing

Figure 7.28: Fourier transform analysis of the experiment data for the case with five baffles.

7.2.4 Case VI

The theoretical model has some limits being one of them related with the width of the ring. Thus, the limit width allows was of 30 mm. However, it is known a larger width allows higher damping of the liquid. In order to understand the beneficial of a larger width, two additional cases where studied. Case VI refers to a five baffle configurations with ring disposed as in Case V, but with a width two times larger. The behavior of wave elevation in time for case VI is represented in Figure 7.29. Calculating the amplitudes at each position, at P1 it is equal to 0.033 m, at P2 it is 0.017 m and at P3 it is equal to 0.0032.

Once the excitation is stopped, it is possible to observe how fast the liquid completely stops. In fact, it seems to completely stop in less than one second. Through the logarithmic

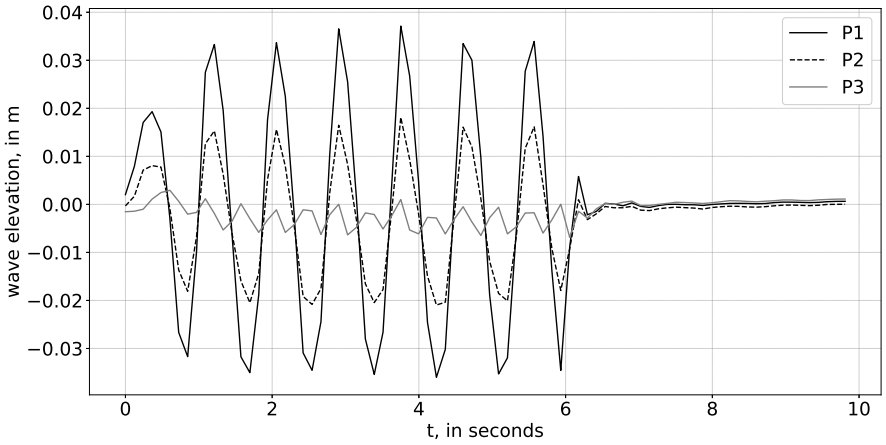

Figure 7.29: Wave elevation as a function of time at the three pressure transducers positions, for Case VI.

decrement of this data, it is possible to obtain a damping ratio of 0.00593.

It is also important to understand the reduction of other frequencies in the fluid. To do so, Figure 7.30 represents the Fourier transforms analysis for Case VI. The most interesting location is P3. Comparing Figure 7.28a and Figure 7.30 it is possible to understand that the second one presents, at p3 location, less peaks of frequencies and less relative magnitude of the existing ones. Besides that, in the other locations, also, a reduction of relative magnitude in smaller peaks is observed. This may indicate that the implementation of larger baffles lead to a more stabilized movement and also reduces the appearance of a chaotic behavior and other normal modes.

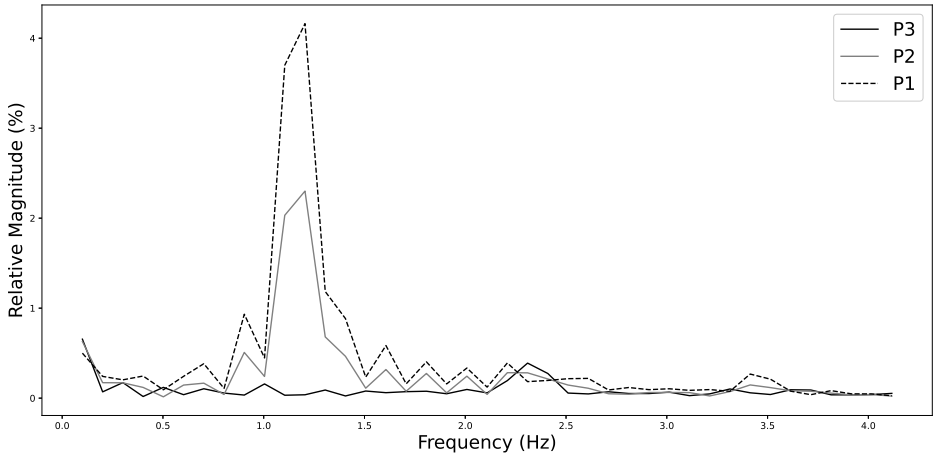

Figure 7.30: Fourier transforms analysis, for Case VI.

7.2.5 Case VII

As in Case VI, Case VII refers to a four baffle configuration with equal displacement of Case III but with a with of 60 mm. Evaluating the plots it is possible to obtain that the amplitudes at locations, P1, P2 and P3 are, respectively, 0.039 m, 0.019 m, and 0.005 m. The excitation is topped and the decrement of the wave elevation is observed. Since the moment the movement is stopped, the fluid stabilized 2 seconds after. Doing the logarithmic decrement of this data, damping ratio is equal to 0.016.

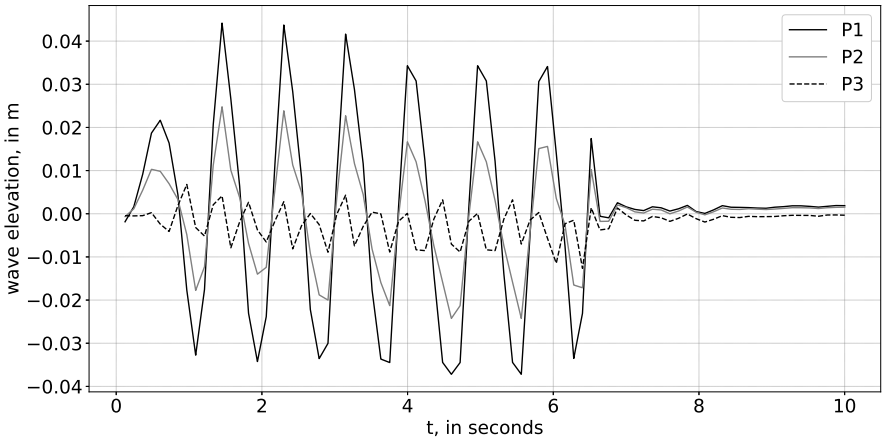

Figure 7.31: Wave elevation as a function of time at the three pressure transducers positions, for Case VII.

Fourier transforms were obtained for the data get and represented in Figure 7.32. Comparing Figures 7.23a and 7.32 it is possible to understand that the larger rings allow a less relative magnitude of other frequencies other than that of the excitation. Besides that, at the location in the axis of the tank it is possible to understand that the magnitude of frequencies decreased. This may implicate that the implementation of larger ring baffles allows a more damped movement of the fluid.

7.2.6 All Cases

Previously, the data obtained through the experimental analysis were discussed. This Subsection compares wave elevation curves in Figure 7.33 at position P1 for all cases. Under excitation, maximum wave elevation does not seem to suffer much alteration from case to case. It is possible to understand that the maximum wave elevation of all cases is around 1800 Pa. The harmonic behavior of the curves seems to become cleaner with the implementation of baffles, which may occur since this anti-sloshing system reduces the movement of the liquid. Also, some other phenomena are observed, like swirls.

For a better comparison between Cases when under excitation, Table 7.5 displaces the amplitudes of curves at the three locations. Case I shows an amplitude almost 1.5 times

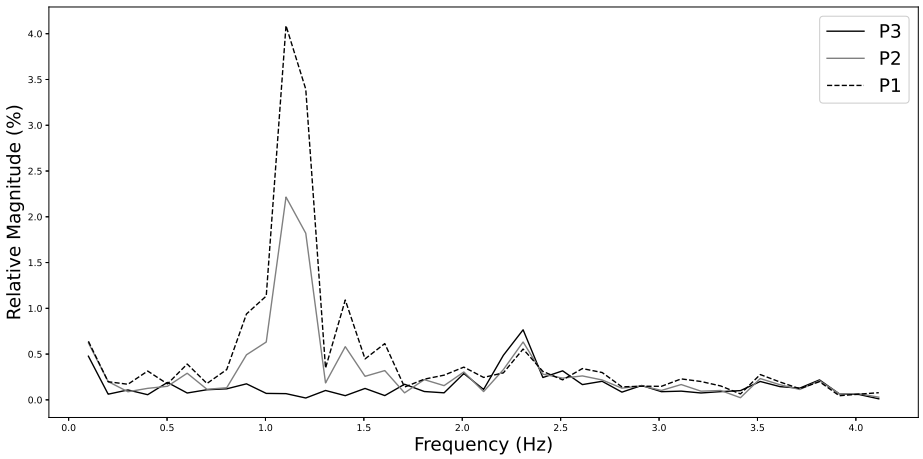

Figure 7.32: Fourier transforms analysis, for Case VI.

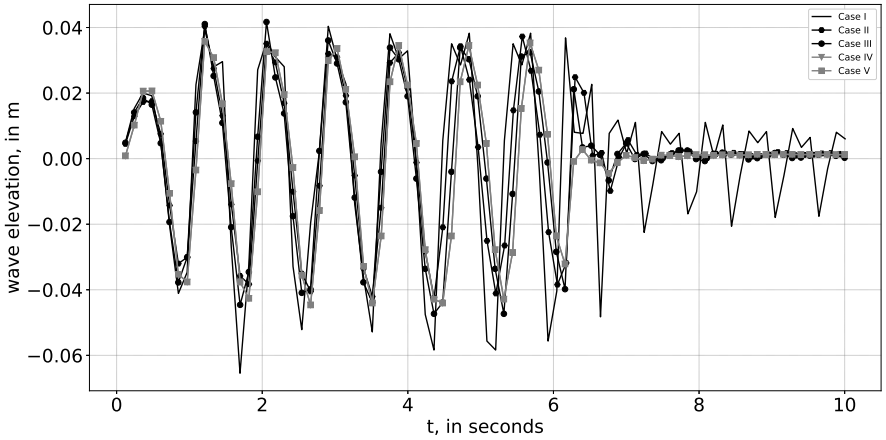

Figure 7.33: Wave elevation as a function of time for the first five Cases.

higher than all the other cases at location P1; at location P3, it is around two times higher. If amplitude at the P1 location reduces, it can be concluded that the wave height reduces with the implementation of ring baffles. The more considerable difference of amplitudes in the axis point allows to conclude that the free surface becomes more linear, and the appearance of other normal modes is reduced. In the P2 location, the difference is not that noticeable, even though it presents a reduction. Theoretical model predicted that the different distancing between baffles would allow higher damping. However, Case III presents higher amplitudes than Case II. In fact, at the P3 location, the amplitude difference is very noticeable. This means that, at least under excitation, Case III configuration is not that beneficial. For five baffles configuration, the same is perceptible. Implementing one more ring also did not show much difference in amplitudes. The reduction of wave elevation was not significant. Furthermore, the two extra cases studied are accounted in the following Table. It is possible to understand that Case VI reduces the amplitudes of

the waves. The most important reduction refers to the amplitude at P3 location which reduced significantly. This means that this new configuration reduces the instability of the liquid. Besides that, it is possible to understand that these larger configurations lead the stopping of the liquid faster than the other ones. On the other hand, while Case VI shows a higher difference, the same can not be said for Case VII. The amplitudes reduced but in a very considerable way. In fact, Case II shows lower amplitudes than case VII.

Table 7.5: Amplitudes, in m, of the experimental data.

	P1	P2	P3
Case I	0.052	0.021	0.015
Case II	0.039	0.022	0.005
Case III	0.042	0.023	0.0047
Case IV	0.039	0.022	0.0046
Case V	0.041	0.024	0.007
Case VI	0.033	0.017	0.0032
Case VII	0.039	0.019	0.005

Even though during excitation conditions, the behavior of all cases is very similar when they are stopped, Case I performs very differently from the others. After 6 seconds of simulation, it is observed that Case I has waves with a relatively high amplitude, while the other four cases reduce the amplitude very rapidly. Thus, the implementation of ring baffles, indeed, helps to dampen the liquid. Table 7.6 shows the damping ratio obtained with experimental data. Damping ratio values show the difference between the cases with with baffles and no baffles. However, it is necessary to note that the damping ratio for cases with five baffles are very low. One of the reasons for this values is due to the curves that are not very clear for these cases and since the movement of the liquid is almost instantly ceased it leads to a more difficult observation. This does not mean that this configurations are not efficient. On the contrary, the experiments show the efficacy of these configurations on stabilizing the fluid

Table 7.6: Damping ratio from the experimental data.

	γ
Case I	0.0038
Case II	0.01899
Case III	0.021
Case IV	0.0019
Case V	0.0031
Case VI	0.00593
Case VII	0.016

7.3 Comparison Between Numerical And Experimental Models

One of the objectives of this work is to validate the numerical method through experiments. Thus, this section is dedicated to comparing both methods. For better comprehension, the results will be compared only for location P1 since it represents the nearest location of the wall and with the higher interest.

7.3.1 No baffles

Figure 7.34 shows the curves of the numerical and the experimental model at the location closer to the wall. The behavior of the curves seems to be very similar in such a way that at the maximum amplitude, both curves present the same particular behavior. However, it is seen that the medium line is not in the same place for both cases. The amplitudes of the wave are critical since they show in which way the movement is similar. The experimental model exhibits a maximum amplitude of 0.052 m, while the numerical model gives a value of 0.087 m, which implies a relative error of approximately 40%. The numerical model does not consider the surface tension since the theory allows this consideration. However, during the experimental analysis, it was possible to observe the effects of surface tension so that it was possible to see how the fluid was glued to the acrylic. Thus, this can be one of the reasons for this error. Besides that, one of the reasons for the numerical difference can be related with the turbulence model that may be not well calibrated specially relating to wall the wall treatments.

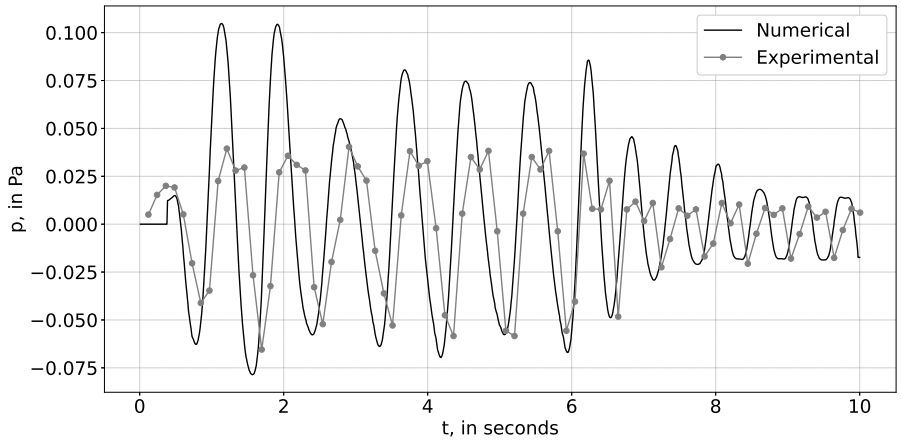

Figure 7.34: Wave elevation as a function of time at location P1 for both the numerical and experimental models, for Case I.

Experimental analysis allowed to observe the behavior of the water. It was possible to conclude that the fluid presented swirl and some other normal modes appeared, as seen

by the Fourier transforms in Figure 7.17. ANSYS Fluent ® did not show that type of performance. A tridimensional analysis of the fluid shows the appearance of other waves but not as so noticeable as seen in the experimental model. Besides the differences in amplitudes, the behavior of both curves is very similar, and it shows irregularities in almost the same places, which can lead to the assumption that the numerical model predicted the behavior of the liquid.

7.3.2 With Four Baffles

The numerical and experimental analysis of four baffle configurations is compared in Figures 7.35 and 7.36. Case II (Figure 7.35) looks similar. Even the stability of the function seems very close. Case III (Figure 7.36) presents a very irregular function in the data obtained from ANSYS Fluent®. On the contrary, the experimental model gives a cleaner function. Under excitation conditions, for Case II, the amplitude of the numerical data is equal to 0.044 m, and for the experimental, it is 0.039 m. The relative error of the experimental is equal to 11.4%. The relative error is small, meaning both analyses allow a very close result. For Case III, the amplitude of the numerical data is equal to 0.054 m, and the experimental is 0.042 m, giving a relative error of 22.2%. One of the reasons for this error to be higher than for Case II may be the irregularities of the numerical data. As soon as the excitation is ceased, the numerical analysis for both cases shows a more rapid stabilization of the fluid than the experimental one, which can influence the final results for damping values.

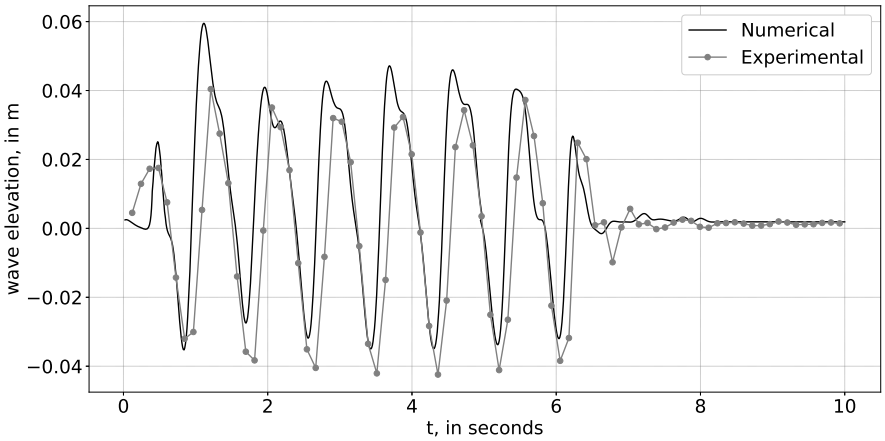

Figure 7.35: Wave elevation as a function of time at location P1 for both the numerical and experimental models, for Case II.

ANSYS Fluent ® allows a representation of the fluid movement. One exciting thing was how the fluid stayed ”stuck” for some instants in the baffle surface and the tiny drops of water that separated from the free surface. These phenomenons seen in numerical representations were also observed in the numerical one even though with more intensity. It

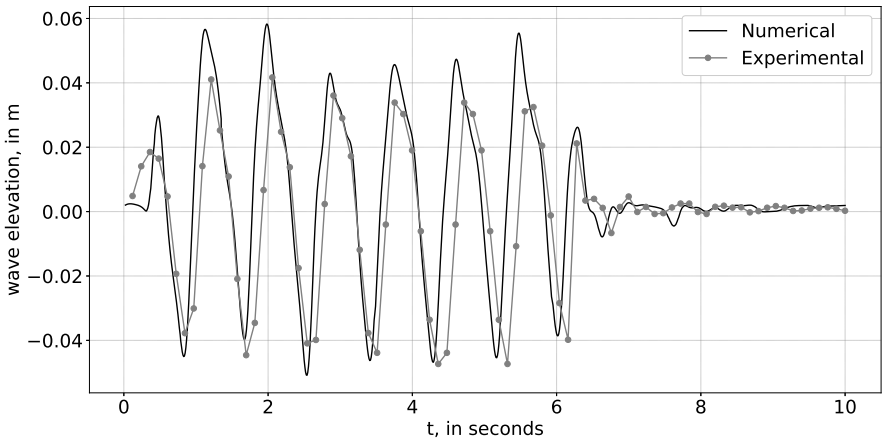

Figure 7.36: Wave elevation as a function of time at location P1 for both the numerical and experimental models, for Case III.

is possible to say that the prediction of fluid movement was better for configurations with anti-sloshing systems than for the empty Case. One of the reasons for this differences may be related with the turbulence model used. As seen, the cases with baffles shows a more chaotic movement of the fluid which may induce a different modulation of turbulence. Thus, maybe the wall treatments used for the baffled cases leaded to the differences observed. Moreover, the mesh in use as elements of 6 mm being refined in the free-surface with elements of 2.5 mm. However, in this cases it is observed that the fluid separates in some parts and also the interaction with the walls is more pronounced. Thus, the non refinement of the mesh in the walls can lead to discrepancies.

7.3.3 With Five Baffles

A fifth ring baffle was inserted and tested in both models. Figures 7.37 and 7.38 compare both analyses for Cases IV and V, respectively. Case IV shows a closer relation between both models in that the curves show almost the same amplitude. Case V, on the contrary, shows a more noticeable difference. Case IV accounts for an amplitude of 0.034 m in the numerical analysis and 0.039 m in the experimental. This difference accounts for a relative error of 14.7%. This relative error decreased when compared with the cases mentioned before. For Case V, the amplitude given by ANSYS Fluent ® is equal to 0.051, and by the experiments is equal to 0.041 m, which implies a relative error of 19.6%.

The numerical model prediction for configurations with five ring baffles looks closer to the experimental model than the other cases since the relative error decreased. However, when the tank excitation is stopped, the movement of the liquid looks different in both cases. As mentioned, the numerical prediction of the liquid's movement looks close in both cases, even showing similar phenomena.

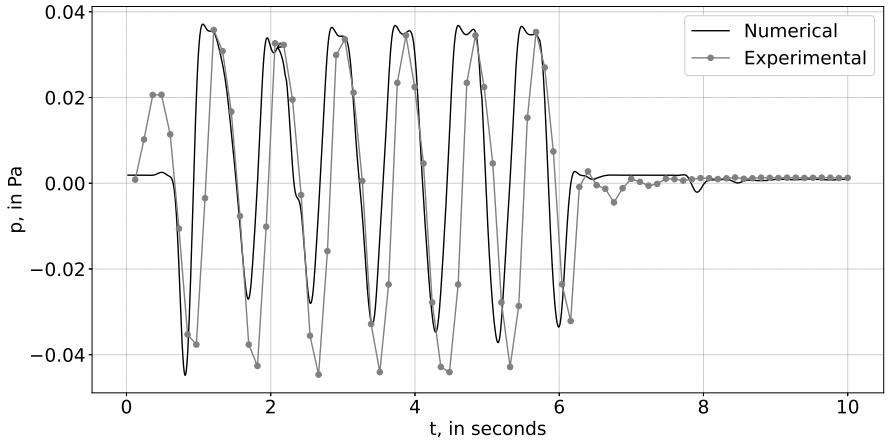

Figure 7.37: Wave elevation as a function of time at location P1 for both the numerical and experimental models, for Case IV.

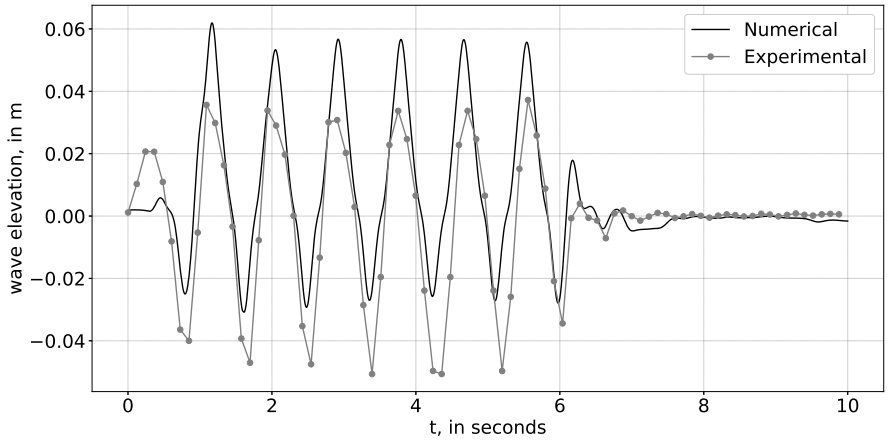

Figure 7.38: Wave elevation as a function of time at location P1 for both the numerical and experimental models, for Case V.

7.4 Comparison Between The Three Models

The objective is to compare the damping ratio results through the three models and conclude which is the better anti-sloshing system. Thus, Table 7.7 shows the damping ratio obtained for each case within the three models. Besides that, the relative error is presented considering the theoretical value of the reference.

Case I shows the most significant difference in damping ratio, thus showing the biggest relative error. The numerical model presents a relative error of 304%, and the experimental presents a relative error of 65%. This difference may occur due to the dynamics of the fluid. As the experimental model shows, the liquid presents a swirl motion and slight chaotic behavior. Furthermore, other waves appear. The theoretical theory only predicts

damping under linear conditions. One other reason for the difference in the experimental model is the presence of surface tension. The image acquisition allows to observe how the fluid and the acrylic behave together. The tension between the walls of the tube and the liquid was very perceptible. The conditions were chosen based on the project requirements and the theory that predicted the linear conditions. However, there are different theories with different explanations and predictions for sloshing. Moreover, the tank was considered fully cylindrical, which is only partially true because the cylindrical part is tiny, and two spherical domes interfere with the fluid. It was seen that the fluid reached the upper dome, causing an enrollment, which led to a more chaotic behavior.

The implementation of ring baffles significantly reduces the relative error. Hence, implementing these anti-sloshing systems allows the stabilization of the free surface, approaching a more linear behavior. The prediction will be closer since the theory is only made for linear conditions. It is significant the increment in damping ratio with the implementation of baffles. This was seen through the experimental data. Both numerical and experimental models allowed to see the efficacy of stabilizing the liquid. Damping ratios of Cases II and III also allow to conclude that different spacing is more efficient in reducing the movement. When five baffles were evaluated, it was seen that the efficacy also increased, seeing that the fluid completely stopped after only one second of the stopping movement. However, the irregularity of the curves in numerical and experimental models made the logarithmic decrement give very low damping ratios. Also, it is essential to mention that the ring baffles used in experimental data were made of steel and had a small gap between the outer radius and the tank that made the water pass through it. The material of the rings was slightly harsh, and the tension between the water and these systems was perceptible.

Table 7.7: Damping ratio from the theoretical, numerical, and experimental models.

	γ			Relative error, in %	
	Theoretical	Numerical	Experimental	Numerical	Experimental
Case I	0.0023	0.0093	0.0038	304	65.2
Case II	0.0198	0.0194	0.0189	20.2	40.9
Case III	0.0257	0.0204	0.021	20.6	18.2
Case IV	0.0019	0.016	0.0279	42.6	93.1
Case V	0.0031	0.0048	0.03162	84.8	90.1

Even though the values of the damping ratio are unclear, the visualization of the experiments allows a perfect conclusion. As mentioned in the Sections above, the difference in amplitudes of baffle configurations under excitation was not very significant, and even the way that the fluid acts as soon as the excitation is stopped is similar. One crucial factor for anti-sloshing systems is understanding when adding more weight will be entirely beneficial. Studying the cases with a bigger width showed a very stable movement of the fluid. Furthermore, even when in excitation conditions, the movement seemed significantly stabilized. Nevertheless, the addition of this weight may not be beneficial. Thus, the conclusion is that the five baffle configurations present better results.

Chapter 8

Conclusions And Future Work

8.0.1 Summary And Conclusions

The research developed and discussed in the current work aimed to discover an anti-sloshing system in the scope of the VIRIATO project. This was accomplished using three different methods. The first method is based on one theory developed by Miles and previously evolved by Bauer. A first code was implemented in Python that only allowed studies with equal distances between baffles. It was seen that as the number of baffles increased, the damping ratio also increased. Besides that, a larger ring and a more spaced configuration also provided a more stabilized fluid movement. In order to have a better perception of the damping of each configuration, the integral of the plot obtained was calculated. Hence, evaluating the mean damping ratio of only two configurations was interesting to study in more detail. Thus, from this the configurations obtained were: $n = 4, w = 30\text{mm}, D = 44\text{mm}, y = 41\text{mm}$, and $n = 5, w = 30\text{mm}, D = 29\text{mm}, y = 41\text{mm}$. However, as mentioned, this first Python study only allowed to study configurations with rings equally spaced. Thus, an optimization study was implemented using Powell's method to understand if equal spacing was more beneficial than different spacing. This study provided two configurations with higher mean damping ratio and different spacing:$n = 4, w = 30\text{mm}, D_1 = 20\text{mm}, D_2 = 16\text{mm}, D_3 = 58\text{mm}, y = 43\text{mm}$, and $n = 5, w = 30\text{mm}, D_1 = 20\text{mm}, D_2 = 18\text{mm}, D_3 = 17\text{mm}, D_3 = 58\text{mm}, y = 48\text{mm}$. Through this analysis a study matrix with different configurations was obtained to be implemented in the numerical and experimental models.

The second part of this work consists of implementing a numerical model in ANSYS Fluent®. The four configurations and the case with no baffles were studied using a pressure-based and transient method in the software. The implementation of the turbulence model was also essential. A first research was made, and based on the literature review, the k-ε Standard model was used. For a sloshing problem is necessary to use a multiphase model, thus, VOF was implemented.

The third approach was done by an experimental model fully developed at INEGI to be used in other works. Since the original tank had such big dimensions, it was necessary to do a scaling analysis. The tank was constructed with acrylic and aluminum. The cylindrical part consisted on an acrylic tank that was cut with the necessary dimensions. The spherical domes were machined in aluminum blocks. The anti-sloshing system was defined in order to be of easy to take off and define the different configurations. To implement the excitation, a rig was fully developed with aluminum extruded profiles. The

excitation was provided to the tank using an electric engine and a Scotch-Yoke mechanism. Three pressure transducers were implemented in the lower dome to evaluate the liquid's behavior. Image acquisition was also essential for this project. Thus, a camera was used for image recording.

A first comparison between the numerical and experimental data was discussed in Section 7.3, and it was concluded that the numerical model made a very close approximation. The amplitude results were compared, and the relative error varied from 38% to 3% , with the most significant difference for the case with no baffles. One of the reasons for this errors are related with the chaotic movement of the liquid which can imply that the turbulence model was not correctly implemented. besides that, in the numerical model the surface tensions were neglected, and in the experimental model it was possible to see that the tensions also had effect in liquid damping.

Lastly, relating to anti-sloshing configurations, the five ring baffles showed a better performance on damping the liquid under the defined conditions. Contrary to what was expected in theory and not relying only upon the damping ratio, the best configuration would be equally spaced. This choice is because it showed a better reduction of the movement when the fluid is under excitation and also because this occupies a higher height percentage of the tank, which is in conditions where the emptying of the tank may be beneficial.

8.0.2 Future Work

This work proved to be a very complex work compiling all three components: numerical, experimental and analytical. These components allowed to obtain a first configuration of an anti-sloshing system for tanks of sub-orbital vehicles. However, these work can be a little more extended in the future. Thus, here are some suggestions for futures works.

- **Consideration of the pressure drop effect:** Pressure drop effects and the utilization of cryogenic fuels are of paramount importance in the context of sloshing phenomena. Pressure variations within a tank can influence the dynamics of fluid motion. Furthermore cryogenic fluids, due to their extreme low temperatures, exhibit unique thermodynamic behaviors, including phase changes and density variations. Thus, when a fluid with such low temperatures is excited, both fluids inside the tank interacts and the temperature changes which may lead to a pressure drop effect. This is important to guarantee safety in the structure of the tank.

- **Consideration of natural frequency difference in tanks with baffles:** The implementation of ring baffles changes the dynamic of the fluids which means that the natural frequency also changes. It would be interest to do a natural frequency study to understand in which way these anti-sloshing systems interfere in the fluid dynamics.

- **Testing in different sloshing regimes:** This study was studied for conditions predicted to be under the linear range. However, it was seen that swirl and chaotic mode appear. It would be interest to study sloshing under the three regimes and see the efficacy of each configuration in each regime.
- **Different treatment for turbulence effects and wall treatments:** In this study, the turbulence was modeled through the k-ε model since the literature review allowed to understand that this modulation has good results. However, in some cases it was seen that LES allowed a better approach with the experimental results. For this study, due to the computational cost of this modulation, it was not considered. besides that, the treatment of the wall was neglected since the theory allowed to consider that the wall tension was not important. Furthermore, the tension between the fluid and the tank walls was not consider.
- **Different types of baffles:** Even thought the main objective of this work was to find a good anti-sloshing system, the main focus was the ring baffles. This is due to the information obtained in the literature review. In past works, ring baffles seemed to be the best option to reduce sloshing effects specially for space applications. However, that does not mean that these are the best option. Thus, it would be good to test exceptional configurations. That was not possible to do due to the lake of time to create different geometries and also because the theory did not allowed to have a first configuration for that.

Bibliography

[1] T. Ahmad, S. L. Plee, and J. P. Myers, Fluent Theory Guide, Nov. 2013. xvii, 47, 48, 49, 50, 51

[2] H. N. Abramson, The Dynamic Behavior of Liquids in Moving Containers, with Applications to Space Vehicle Technology. NATIONAL TECHNICAL INFORMATION SERVICE, Jan. 1966. 1

[3] M. Dreyer, "Propellant behavior in launcher tanks: An overview of the compere program," in Progress in Propulsion Physics. Brussels, Belgium: EDP Sciences, 2009. doi: 10.1051/eucass/200901253. ISBN 978-2-7598-0411-5 978-2-7598-0687-4 pp. 253–266. 1

[4] P. Marques, "Scaling and numerical analysis of non-isothermal sloshing for space propulsion," Master's thesis, IST, Lisboa, Oct. 2020. 1, 5, 6, 16, 22, 41, 42

[5] "The First Lunar Landing," https://history.nasa.gov/alsj/a11/a11.landing.html. 1

[6] F. Dodge and H. Abramson, "Liquid propellant dynamics in the Saturn/Apollo vehicles - A look back," in 41st Structures, Structural Dynamics, and Materials Conference and Exhibit. Atlanta,GA,U.S.A.: American Institute of Aeronautics and Astronautics, Apr. 2000. doi: 10.2514/6.2000-1676 1

[7] "Suborbital Launch Vehicles | SKYRORA," Dec. 2022. 1

[8] "Omnidea | omnidea.net," https://www.omnidea.net/viriato.html. 2

[9] P. Gaillard, C. L. Touze, L. Matuszewski, and A. Murrone, "Numerical Simulation of Cryogenic Injection in Rocket Engine Combustion Chambers," Aerospace Lab, no. 11, p. 16, 2016. doi: 10.12762/2016.AL11.16 2

[10] P. Luthada, "What is Automated Fibre Placement (AFP)?" https://www.addcomposites.com/post/what-is-automated-fibre-placement-afp, Jun. 2022. 2

[11] A. L. Braslow, P. G. Bhuta, R. E. Hutton, H. N. Abramson, and D. G. Stephens, "Propellant slosh loads," National Aeronautics and Space Administration, Spetial Publication NASA SP-8009, Jul. 1968. 2, 13

[12] F. Monteiro, "Non-Isothermal Sloshing for Space Applications Experimental Characterisation," Master's thesis, University of Beira Interior, Covilhã, Jan. 2023. 5, 6, 16, 22, 25

[13] T. Arndt, "Sloshing of cryogenic liquids in a cylindircal tank under normal gravity conditions," Ph.D. dissertation, University of Bremen, Oct. 2011. 5, 6, 9, 19

[14] F. T. Dodge and S. Antonio, The New Dynamic Behavior of Liquids in Moving Containers, Southwest Research Institute San Antonio, Texas, 2000. 5, 6, 7, 9, 10, 13, 17, 31

[15] R. A. Ibrahim, Liquid Sloshing Dynamics: Theory and Applications, 2005. 5, 6, 8

[16] C. Montsarrat, "Fluid motion analysis in the cryogenic tanks of the upper stage of Ariane 5 during the ascent phase," Master's thesis, Kungl. Tekniska Högskolan, Teknikrigen 8, SE-100 44 Stockholm., 2017. 5, 16, 19

[17] H. N. Abramson and L. R. Garza, "Measurements of liquid damping provided by ring baffles in cylindrical tanks," Tech. Rep. NASA-CR-52070, Apr. 1963. 7, 28

[18] D. Liu and P. Lin, "A numerical study of three-dimensional liquid sloshing in tanks," Journal of Computational Physics, vol. 227, no. 8, pp. 3921–3939, Apr. 2008. doi: 10.1016/j.jcp.2007.12.006 8

[19] ——, "Three-dimensional liquid sloshing in a tank with baffles," Ocean Engineering, vol. 36, 2009. doi: 10.1016/j.oceaneng.2008.10.004 8

[20] D. G. Stephens, H. W. Leonard, and T. W. Perry, "Investigation of the damping of liquids in right-circular cylindrical tanks, including the effects of a time-variant liquid depth," Jul. 1962. 9

[21] D. G. Stephens, H. W. Leonard, and M. A. Silveira, "An Experimental Investigation of the Damping of Liquid Oscillations in an Oblate Spheroidal Tank With and Without Baffles," Tech. Rep. NASA-TN-D-808, Jun. 1961. 14

[22] H. F. Bauer, "The Damping Factor Provided by Flat Annular Ring Baffles for Free Fluid Surface Oscillations," National Aeronautics and Space Administration, Technical Memorandum, Sep. 1962. 14, 29, 30

[23] I. E. Sumner, "Experimental investigation of stability boundaries for planar and non-planar sloshing in spherical tanks," Tech. Rep. NASA-TN-D-3210, Jan. 1966. 16

[24] A. Van Foreest, M. Dreyer, and T. Arndt, "Moving Two-Fluid Systems Using the Volume-of-Fluid Method and Single-Temperature Approximation," AIAA Journal, vol. 49, Dec. 2011. doi: 10.2514 / 1 . J 050482 19, 55

[25] C. Hirsch, Numerical Computation of Internal and External Flows: Fundamentals of Computational Fluid Dynamics, 2nd ed. Oxford ; Burlington, MA: Elsevier/Butterworth-Heinemann, 2007. ISBN 978-0-7506-6594-0 19, 42, 43

[26] M. E. Dreyer, Free Surface Flows under Compensated Gravity Conditions, ser. Springer Tracts in Modern Physics. Berlin ; New York: Springer, 2007, no. v. 221. ISBN 978-3-540-44626-2 19

[27] F. M. White, Fluid Mechanics, 17th ed. McGraw-Hill, 2011. ISBN 978-0-07-352934-9 19, 24

[28] X. Vallés Rebollo, E. Sadeghi, I. Kusano, and A.-A. García-Granada, "Study of the Sloshing Dynamics in Partially Filled Rectangular Tanks with Submerged Baffles Using VOF and LES Turbulence Methods for Different Impact Angles," Computation, vol. 10, no. 12, p. 225, Dec. 2022. doi: 10.3390/computation10120225 19, 39, 42, 48

[29] V. d. Brederode, Aerodinâmica incompressível: Fundamentos, 2nd ed. Guide - Artes Gráficas, Lda, 2018. 20, 46

[30] T. Arndt and M. Dreyer, "Damping Behavior of Sloshing Liquid in Laterally Excited Cylindrical Propellant Vessels," Journal of Spacecraft and Rockets, vol. 45, no. 5, pp. 1085–1088, Sep. 2008. doi: 10.2514/1.35019 21

[31] T. Arndt, M. Dreyer, P. Behruzi, M. Winter, and A. vanForeest, "Cryogenic Sloshing Tests in a Pressurized Cylindrical Reservoir," in 45th AIAA/ASME/SAE/ASEE Joint Propulsion Conference & Exhibit. Denver, Colorado: American Institute of Aeronautics and Astronautics, Aug. 2009. doi: 10.2514/6.2009-4860. ISBN 978-1-60086-972-3 22, 55

[32] B. Weigand and V. Simon, "Laws of similarity in fluid mechanics," in WIT Transactions on State of the Art in Science and Engineering, 1st ed., R. Liebe, Ed. WIT Press, Nov. 2006, vol. 1, pp. 20–35. ISBN 978-1-84564-001-9 22, 39, 40, 42

[33] H. Zinzuwadia, "Effect of horizontal baffles on the performance of mechanically agitated gas-liquid contactors," Ph.D. dissertation, Texas Tech University, May 1987. 22

[34] J.-W. Jang, A. Alaniz, L. Yang, J. Powers, and C. Hall, "Mechanical Slosh Models for Rocket-Propelled Spacecraft," in AlAA Guidance, Navigation and Control Conference, Boston, CA, Aug. 2013. 23

[35] J. G. Pérez, R. A. Parks, and D. R. Lazor, "Validation of Slosh Model Parameters and Anti-Slosh Baffle Designs of Propellant Tanks by Using Lateral Slosh Testing," in 28th Aerospace Testing Seminar, Los Angeles, CA, 2012. 24, 30, 31

[36] K. Modaressi-Tehrani, S. Rakheja, and I. Stiharu, "Three-dimensional analysis of transient slosh within a partly-filled tank equipped with baffles," Vehicle System Dynamics, vol. 45, no. 6, pp. 525–548, Jun. 2007. doi: 10.1080/00423110601059013 27, 40, 42

[37] P. Panigrahy, U. Saha, and D. Maity, "Experimental studies on sloshing behavior due to horizontal movement of liquids in baffled tanks," Ocean Engineering, vol. 36, no. 3-4, pp. 213–222, Mar. 2009. doi: 10.1016/j.oceaneng.2008.11.002 27, 55

[38] A. Maleki and M. Ziyaeifar, “Sloshing damping in cylindrical liquid storage tanks with baffles,” Journal of Sound and Vibration, vol. 311, no. 1, pp. 372–385, Mar. 2008. doi: 10.1016/j.jsv.2007.09.031 27, 28, 56

[39] H. Akyıldız, N. Erdem Ünal, and H. Aksoy, “An experimental investigation of the effects of the ring baffles on liquid sloshing in a rigid cylindrical tank,” Ocean Engineering, vol. 59, pp. 190–197, Feb. 2013. doi: 10.1016/j.oceaneng.2012.12.018 28, 55

[40] F. T. DODGE and D. D. KANA, “Moment of inertia and damping of liquids in baffled cylindrical tanks.” Journal of Spacecraft and Rockets, vol. 3, no. 1, pp. 153–155, 1966. doi: 10.2514/3.28408 28

[41] N. Kumar, “Study of sloshing effects in a cylindrical tank with and without baffoles under linear acceleration,” Master’s thesis, NATIONAL INSTITUTE OF TECHNOLOGY, ROURKELA, Jun. 2013. 29

[42] R. Suyal, “CFD analysis of fuel sloshing in a cylindrical tank with and without baffles under linear acceleration,” Master’s thesis, National Institute of technology, Rourkela, 2016. 29, 41, 42

[43] J. R. Roberts, P.-Y. Chen, and E. R. Basurto, “Slosh design handbook I,” May 1966. 30

[44] S. Petersen, “Methods of Optimization for Numerical Algorithms,” Jul. 2027. 33

[45] T. Okamoto and M. Kawahara, “Two-dimensional sloshing analysis by the arbitrary Lagrangian-Eulerian finite element method,” Doboku Gakkai Ronbunshu, vol. 1992, no. 441, pp. 39–48, Jan. 1992. doi: 10.2208/jscej.1992.39 39

[46] Z. Liu, Y. Feng, G. Lei, and Y. Li, “Sloshing Behavior Under Different Initial Liquid Temperatures in a Cryogenic Fuel Tank,” Journal of Low Temperature Physics, vol. 196, no. 3, pp. 347–363, Aug. 2019. doi: 10.1007/s10909-019-02167-w 39, 42

[47] L. Hou, F. Li, and C. Wu, “A numerical study of liquid sloshing in a two-dimensional tank under external excitations,” Journal of Marine Science and Application, vol. 11, no. 3, pp. 305–310, Sep. 2012. doi: 10.1007/s11804-012-1137-y 39, 42

[48] B. Godderidge, S. Turnock, M. Tan, and C. Earl, “An investigation of multiphase CFD modelling of a lateral sloshing tank,” Computers & Fluids - COMPUT FLUIDS, vol. 38, pp. 183–193, Feb. 2009. doi: 10.1016/j.compfluid.2007.11.007 40

[49] V. Singal, J. Bajaj, A. Nimish, and T. Sarthak, “CFD Analysis of a Kerosene Fuel Tank to Reduce Liquid Sloshing | Elsevier Enhanced Reader,” Procedia Engineering, vol. 69, 2014. doi: 10.1016/j.proeng.2014.03.130 40, 42

[50] A. George and I. H. Cho, “Anti-sloshing effects of a vertical porous baffle in a rolling rectangular tank | Elsevier Enhanced Reader,” Ocean Engineering, vol. 214, Aug. 2020. doi: 10.1016/j.oceaneng.2020.107871 40, 42

[51] D. Liu, W. Tang, J. Wang, H. Xue, and K. Wang, “Comparison of laminar model, RANS, LES and VLES for simulation of liquid sloshing,” Applied Ocean Research, vol. 59, pp. 638–649, Sep. 2016. doi: 10.1016/j.apor.2016.07.012 40, 42, 48

[52] G. Yazici, M. Aksel, and A. Koroglu, “Sloshing Displacements of an Above Ground Cylindrical Liquid Storage Tank Subjected to a Near-Fault Earthquake Ground Motion,” Oct. 2014. 40, 42

[53] U. Gopalakrishnan, S. V. Prasad, V. S. Nair, and A. Suryan, “Investigation on the effect of baffle position on sloshing in tanks,” in International Conference on Applied Mechanics and Optimisation, Selangor Darul Ehsan, Malaysia, 2019. doi: 10.1063/1.5120213 p. 040005. 41, 42

[54] T. Ahmad, S. L. Plee, and J. P. Myers, Fluent User’s Guide, Nov. 2013. 44, 46, 50

[55] I. ANSYS, Meshing User’s Guide, Southpointe 275 Technology Drive Canonsburg. 44

[56] M. Jäger, “Fuel Tank Sloshing Simulation Using the Finite Volume Method,” Master’s thesis, Springer Fachmedien Wiesbaden, Wiesbaden, 2019. 45, 46

[57] A. K. Baghel, “CFD STUDY OF SLOSHING IN RECTUNGLAR TANK.” 46, 48

[58] C. Dong, “Modeling and simulation of sloshing motion in partly filled tank,” Master’s thesis, Aalesund University College, May 2015. 48

[59] W. Yang, S. Liu, and H. Lin, “Viscous liquid sloshing damping in cylindrical container using a volume of fluid method,” Science in China Series E: Technological Sciences, vol. 52, pp. 1484–1492, Jun. 2009. doi: 10.1007/s11431-009-0182-5 48, 49

[60] T. Su, “Nonlinear Sloshing and the Coupled Dynamics of Liquid Propellants and Spacecraft,” Tech. Rep., Feb. 1992. 48

[61] S. Sakib and M. M. Karim, “Design and Development of a Cheap Slosh Testing Rig as Laboratory Equipment,” Procedia Engineering, vol. 194, pp. 401–406, 2017. doi: 10.1016/j.proeng.2017.08.163 55

[62] H. F. Scholl, D. G. Stephens, and P. K. Davis, “Ring-baffle pressure distribution and slosh damping in large cylindrical tanks,” National Aeronautics and Space Administration, Technical Note NASA TN D-6870, Dec. 1972. 56

[63] N. Lloyd, E. Vaiciurgis, and T. A. G. Langrish, “The Effect of Baffle Design on Longitudinal Liquid Movement in Road Tankers: An Experimental Investigation,” Process

Safety and Environmental Protection, vol. 80, no. 4, pp. 181–185, Jul. 2002. doi: 10.1205/095758202320439137 56

[64] “Low Range Pressure Sensors | Fast Delivery | AppMeas,” https://appmeas.co.uk/products/pressure-sensors/low-range-pressure-sensor-pa600-lr/. 60

Appendix A

Appendix

A.1 Numerical model setup

1. **Multiphase:**
   - Volume of fluid;
   - Formulation: Explicit;
   - Implicit Body Force;
2. **Viscous model:**
   - $k - \varepsilon$ Standard;
   - Wall function: Standard Wall Function;
3. **General:**
   - X acceleration:
     IF t<6 [s]:
       IF t <0.5 [s]:
         $-0.055[\text{m}] \times (7.29[\text{rad/s}] \times t)^2[\text{ms}^{-2}] \times \sin(7.29[\text{rad/s}] \times t^2)$
       ELSE:
         $-2.87[\text{ms}^{-2}] \times \sin(7.19[\text{rad/s}] \times t)$
     ELSE:
       IF t < 6 [s]:
         0 $[\text{ms}^{-2}]$
   - Y acceleration: -9.81 $[\text{ms}^{-2}]$
4. **Methods:**
   - Pressure-velocity coupling: PISO;
   - Gradient: Green-Gauss Cell Based;
   - Pressure: PRESTO!;
   - Momentum: Second Order Upwind;
   - Volume Fraction: Geo-Reconstruct;
   - Turbulent Kinetic Energy: First Order Upwind;
   - Turbulent dissipation Rate: First Order Upwind;